CHARACTERISTICS OF THE DUKE/OK-4 STORAGE RING FEL AND GAMMA-RAY SOURCE

by

Seong Hee Park

Department of Physics
Duke University

Date: 11/28/00

Approved:

Dr. Vladimir N. Litvinenko, Supervisor

Dr. Lawrence Evans

Dr. Berndt Müller

Dr. Werner Tornow

Dr. Henry Weller

Dissertation submitted in partial fulfillment of the
requirements for the degree of Doctor of Philosophy
in the Department of Physics
in the Graduate School
of Duke University

2000

ABSTRACT

(Physics –Free Electron Lasers)

CHARACTERISTICS OF THE DUKE/OK-4 STORAGE RING FEL AND GAMMA-RAY SOURCE

by
Seong Hee Park

Department of Physics
Duke University

Date: 1/28/00

Approved:

Dr. Vladimir N. Litvinenko, Supervisor

Dr. Lawrence Evans

Dr. Berndt Müller

Dr. Werner Tornow

Dr. Henry Weller

An abstract of dissertation submitted in partial fulfillment of the requirements for the degree of Doctor of Philosophy in the Department of Physics in the Graduate School of Duke University

2000

Abstract

The Duke/OK-4 storage ring is a dedicated device for driving a short wavelength Free Electron Laser (FEL). In addition, Compton scattering of the laser light from the circulating electron beam produces a semi-monochromatic γ-ray source. The dynamics of such a system including accelerator physics, FEL physics, and Compton backscattering is complex and requires special study. This dissertation is a detailed theoretical and experimental analysis of such a system. The main emphasis of the theory presented here is the self-consistent analysis of the system which incorporates three drastically different processes – the dynamics of an intense electron beam, the free electron laser, and the Compton backscattering. The interdependence of these three processes and the physics of this complex system is discussed in this work.

The OK-4/Duke storage ring FEL is the only accelerator facility capable of routine lasing in the deep-UV range and able to generate intense γ-ray beams with energy tunable from 2 MeV to 55 MeV, with energy resolution between 0.5 % - 1 % and with flux up to ~ 5 x 10^7. The flexibility of this γ-ray source is due to the record-breaking performance of the OK-4/Duke storage ring FEL (lasing from 193.7 nm to 730 nm). Experimental studies determining the parameters of the electron beams, OK-4 FEL beams, and γ-ray beams compare favorably with the theoretical

predictions. This study confirms that the electron energy spread induced by FEL lasing is currently the main factor limiting energy resolution. These results provide a solid foundation for future development of the system to obtain more reliable predictions of its performance. A number of useful "scaling laws" are also presented here.

The results of this work have provided the basis for a number of applications of the OK-4 FEL beam and γ-ray beam that are underway or in the advance planning stage. Future plans include the development and design of a system capable of generating γ-ray beams with an energy resolution as low as 0.1%. Future theoretical studies will determine the influence of γ-ray generation on the performance of improved storage ring FELs.

Acknowledgments

I would like to thank my advisor, Dr. Vladimir N. Litvinenko, for all the help and support, encouragement, guidance, and insight that he has given me since I joined the Duke FEL lab. His insight, enthusiasm, and knowledge of physics have advanced my learning and understanding of theoretical as well as experimental physics. In early 1996, there was only an empty optical table in the southwest corner when he was studying the effect of floor vibrations on the mirror feedback system. His dedication to the laboratory set an example that kept me working and studying hard.

I would also like to thank Dr. John M. J. Madey for supporting and encouraging this FEL project and for his discussions about FELs. I wish to thank Dr. Russell Roberson and Dr. Scott Wilburn for their advice during my first semester at Duke. I also wish to thank Dr. Henry Weller and Dr. Werner Tornow for their inspiring support during my work on the γ-ray project.

I would like to thank Dr. Ying Wu, Dr. Bentley Burnham, and Dr. Igor Pinayev for their cooperation, help, and in-depth discussions. They were always there whenever I needed help and had questions about storage rings, the control system, UNIX, hardware, electronics, or optics. They were always ready to aid me,

the only graduate student in the storage ring group, with patience and without hesitation. It was a pleasure for me to spend good times working in this team and to share every moment of glory and frustration with them.

I wish to thank Dr. Alex Lumpkin for helping me with measurements and analysis of the time structure of the electron and optical beams using the streak camera.

I want to thank all my TUNL collaborators for their help and support during the collection and analysis of data on γ rays. I especially wish to thank Eric Schreiber for his role in collecting data and for helpful discussions about γ-ray detectors.

I wish to thank my fellow graduate students in the FEL laboratory. Many thanks to Dr. Brett Hooper, Dr. Genny Barnett, Dr. Lewis Johnson, Dr. Eric Szarmes, and Greg Denbeaux for all the conversations, encouragement, and help since I joined the FEL as a graduate student. I wish Greg Denbeaux the best on his project of LBNL. I also wish to thank Teng Chen for discussions and conversations as a classmate as well as a fellow graduate student at the FEL laboratory. Finally, I wish the best to Charles Neuman on his project at BNL.

I would like to thank everyone at the Duke FEL laboratory for supporting and encouraging me. I have learned so much about engineering, design, instrumentation, vacuum, and purchasing from them. From Ping Wang, I learned a lot about the RF cavity system: she never gave up on helping and supporting me through all the challenges. I want to thank Gary Swift, Crag Kornegay, and Marty Johnson for helping me and teaching me how to condition vacuum chambers. I realize that it is

very tedious to obtain good vacuum inside the beam lines. I wish to thank Nelson Hower for helping and teaching me about mirror distortions caused by mechanical stress from the mirror mount. From Mark Emamian, I appreciate the encouragement and support which kept me going. I would also like to thank the operators, Jim Gustavsson, Jim Widgner, and Brain Hoffman and the Operations Manager, Jim Murphy, for their efforts and help with operating the linac and storage ring, even during late night hours. I also wish to thank Peter Morcombe, Owen Oakeley, and Jim Meyer for all the help in electrical engineering and Joe Faircloth, Gerry Detweiler, and Terry Brinkley for all the support in mechanical assembly. I wish to thank Harold Rose, Doris Albright, and Denise Gamble for helping me with financial and purchasing problems. I really want to say "THANK YOU" to ALL the FEL laboratory family past and present.

I would like to thank Dr. Scott M. Zoldi and Dr. Jim Murphy for their efforts and help correcting the English of this thesis.

Mostly, I would like to thank my husband, Chae Shick Chung, for his support and encouragement that kept me studying and gave me the persistence to finish this thesis.

Finally, I would like to thank my Mother and Father for their endless love and support through all the years of my life. I also wish to thank my sister and brother, for their support.

TABLE OF CONTENTS

LIST OF TABLES

LIST OF FIGURES

Chapter 1

Introduction

This dissertation presents theoretical and experimental studies of Storage Ring (SR) Free Electron Lasers (FELs) and Compton backscattered γ rays. Special attention is paid to the optical klystron in the theoretical developments and the experimental analysis of a storage ring FEL. Novel approaches to the evolution equation of the FEL optical field and to the interactions of electrons with the FEL optical field are discussed to give a better theoretical description of the self-consistent distribution function of an electron beam in a storage ring FEL. This dissertation also presents the experimental results for electron and optical beam parameters of the OK-4 SR FEL. Primary attention is paid to the energy spread and emittance of electron beam and to the temporal and spatial structures of the FEL optical pulse. The dependence of FEL power on cavity tuning and the electron beam parameters is also presented. This dissertation discusses critical issues of the Duke/OK-4 FEL optical cavity focusing on its stability and performance including cavity mirror degradations. Based on dynamics and parameters of the electron and optical beam in the OK-4 SR FEL, theoretical and experimental studies of the γ-ray source using intra-cavity Compton backscattering in the SR FEL are presented. The

theoretical model of the Compton γ-ray source in the OK-4 SR FEL presented here is modified and improved from the previous work [Litvinenko 1995a]. In our model, we focus on the case of most practical importance – a Compton γ-ray source in a storage ring FEL which operates with "flat" electron beams. The experimental results of the energy spectra and spatial distributions of γ rays are presented. The dependence of the flux and the energy resolution of γ rays on the electron beam parameters is discussed, along with a comparison with theoretical analysis using measured electron and optical beam parameters. The results of this analysis support the reliability of the theoretical predictions of parameters of the resulting γ-ray beams.

In the discussion below, the motivation and objectives of the current research is first presented. This is followed by an overview of the basics of FELs, a short review of the experimental results of the Duke/OK-4 SR FEL and critical issues of the Duke/OK-4 FEL resonator, and the fundamentals of the Compton γ-ray source in the Duke/OK-4 SR FEL. A brief outline of the full dissertation concludes this introductory chapter.

1.1 Motivation

The Duke storage ring provides a unique opportunity to study the physics of a complex system consisting of intense ultra-relativistic beams of electrons, a free electron laser, and a Compton γ-ray source. Even though the fundamentals of

accelerator physics, the physics of free electron lasers, and the Compton back-scattering process are well understood, the interplay of these processes in "three dimensions" creates interesting new phenomena. The nonlinear interactions between components of this system must be treated in a self-consistent way to provide an understanding of the dynamics and relevant parameters.

In addition, the experiments with the Duke/OK-4 SR FEL and its γ-ray source are quite challenging. Recent advancements in short wavelength UV FEL and the simultaneous development of a unique semi-monochromatic γ-ray source are at the cutting edge of modern experimental physics. These challenges require development of new experimental methods and an understanding of physics which go well beyond the "three dimensions" mentioned above.

1.2 Objectives

The main objectives of this research are the theoretical study of the physics describing this complex system and a comparison of the theory with the experimental results. We desire to understand the influence of electron and optical beam parameters on the performance of the FEL and the Compton γ-ray source.

The performance of a storage ring FEL depends on the quality of the electron beam and the dynamic aperture of the storage ring. The dynamic energy aperture determines the maximum attainable FEL power. The gain of the FEL depends strongly on both the electron beam peak current and emittance. An electron beam

with an emittance smaller than $\lambda/4\pi$ is required to operate the FEL at a wavelength λ. Low emittance and high peak current of the electron beam are important for short wavelength FELs. The lattice design and the study of electron beam dynamics in the Duke storage ring is discussed in the Ph.D. dissertation of Dr. Ying Wu. The electron beam dynamics in the Duke/OK-4 SR FEL must take into account the parameters of the optical klystron installed in the storage ring. In addition, the stability and quality of the optical cavity should be carefully studied to optimize FEL performance. The quality of γ rays generated via Compton backscattering depends strongly on the parameters of both the electron and optical beams. The availability of high brightness electron and optical beams has allowed us to produce intense γ-ray beams with energy resolution of less than ~ 1% using a 3 mm collimator.

A nice feature of a storage ring FEL is that the parameters of both the electron and optical beams are easily adjustable for a systematic study of the FEL and the γ-ray source. Proper choices of beam parameters can optimize the FEL performance for different applications.

We measured the following electron beam parameters: current, emittance, beta function, bunch length, and energy spread. We also measured spectra and bunch length of the optical beams, cavity losses, and transmittance of cavity mirrors. We studied characteristics of the Duke/OK-4 SR FEL including both micro- and macro-temporal structures, transverse mode structure, bunch lengthening, and FEL power dependence on beam parameters. We developed a theoretical model allowing an analytical evaluation of the energy distribution of γ-ray beams for arbitrary

geometries. We also derived an analytical formula, which can be reduced to a one-dimensional integral, for the energy spectrum of γ rays generated by a flat electron beam through a pinhole collimator. We compare the measured energy spectrum of the γ rays with this theoretical calculation using measured electron and optical beam parameters. This confirmation of the theoretical calculation is important for estimating the beam quality of high energy γ rays above ~ 20 MeV, since it is hard to find a detector with good (0.1 % or better) energy resolution in this energy. The theoretical model which is confirmed by experimental measurements at low energy, can be used to evaluate the quality of high energy γ rays.

1.3 Basics of Free Electron Lasers

A free electron laser is a device consisting of a relativistic electron beam, an wiggler, and an optical cavity. As the electron beam propagates collinearly with the optical wave along the wiggler, the electron beam oscillates transversely due to an alternating magnetic field and starts to interact with the optical field transferring its kinetic energy to the optical field. The wavelength of radiation is determined by the electron beam energy, the wiggler period, and the wiggler parameter, K_w. Unlike atomic quantum lasers, the electrons in an FEL are "*free*" and cannot be "destroyed" by high optical power. These unique characteristics make it possible to build FELs for a wide range of wavelengths, from mm wave to the soft x-ray region, and to

produce semi-monochromatic hard x rays or γ rays via Compton backscattering with high power or/and flux.

FEL gain arises from electron bunching in the longitudinal (φ, E_e) phase space, where E_e is electron energy and φ is the relative phase between the electron and optical beam. These bunched electrons radiate coherently and cause an exponential growth of the optical field strength. At short wavelengths, the gain is reduced because highly energetic electrons are difficult to bunch. The FEL gain can be improved by increasing the number of wiggler periods, N_w, and the electron beam peak current. However, increasing N_w increases the sensitivity of the beam to emittance and energy spread. Increasing the current often decreases the beam quality which results in gain reduction by degrading the electron bunching. At peak FEL power, the growth of the field decreases due to a saturation mechanism, which is caused by over-bunching in a linac based FEL and induced energy spread in a storage ring FEL. When the field strength increases so that the net gain is equal to the total loss, the FEL has reached a steady state.

In the small signal gain regime of an FEL oscillator, the optical field develops from spontaneous emission (i.e. from the noise) with an initial coherence length of $N_w\lambda$, corresponding to the slippage in the longitudinal direction. As the electrons co-propagate with the optical fields along the wiggler, bunching develops in the electron beam and the electrons slip behind the optical fields with which they interact. The electromagnetic fields radiated by the electrons add up on the trailing edge of the optical fields in each pass. This, known as "the lethargy of the FELs"

[Hopf 1976 & 1980], causes an increase in the coherence length and the linewidth narrowing in FELs. In the transverse dimension, the important scale is the waist size of the optical beam, which grows due to diffraction as it propagates along the wigglers. The boundary conditions at the cavity mirrors and the wavelength define a minimum mode size.

There are many different wiggler designs each having different features (for details, see Chapter 4 in Laser Handbook (1990) and the references therein). A helical wiggler produces a circularly polarized FEL with high gain compared to a planar wiggler, but generates no high harmonics on the axis. A planar wiggler produces linearly polarized light and can be used for high harmonic generation. The optical klystron allows an efficient bunching causing an increase in the FEL gain in a fixed interaction length through three stages of operation: energy modulation, density modulation, and coherent radiation. However, the optical klystron experiences power saturation at a lower level.

1.4. The Duke/Ok-4 Storage Ring FEL

Storage ring free electron lasers are the best devices for lasing at short wavelengths among FELs. Lasing at short wavelengths requires both a high quality optical system and a high quality electron beam. Successful lasing at short wavelengths is, therefore, the result of the high quality electron (or positron) beams provided by modern storage rings. Presently, SR FELs operate reliably at UV and

visible wavelengths. They provide laser beams with high peak and average power as well as continuously tunable wavelengths. The lack of high reflectivity cavity mirrors is the main obstacle to lasing at wavelengths below 200 nm. Several FEL facilities around the world are attempting operation at wavelengths below 200 nm. The ultimate aim is creating an x-ray FEL. Currently, a number of FELs are used to generate beams of semi-monochromatic γ rays (or x rays) with tunable energy via Compton backscattering of FEL photons.

The Duke storage ring is dedicated to driving UV and XUV FELs. It has 34 m long straight sections, a large dynamic aperture, and operates with high current and low emittance electron beams. Since the first lasing at a central wavelength of 380 nm in 1996 [Litvinenko 1998], the Duke storage ring FEL system (the OK-4/Duke SR FEL) has been further developed. These upgrades have resulted in substantial enhancements in FEL gain by allowing higher currents, and better quality, more stable electron beams. Upgrades to the e-beam diagnostic systems have played an important role by eliminating the "blindfold" operations of the early years at Duke. These improvements, in combination with better cavity mirrors, made it possible to lase at a wavelength below 200 nm in August, 1999 [Litvinenko 1999b]. The OK-4/Duke SR FEL has demonstrated lasing in a wavelength range from 193.7 nm to 730 nm using five sets of dielectric mirrors. Lasing in this wide range of wavelengths and the operation of the Duke storage ring at electron energies from 240 MeV to 800 MeV have allowed the generation of nearly monochromatic γ rays with a peak energy tunable from 1.8 MeV to 55 MeV with an energy resolution of 0.5 % -

1 % FWHM (depending on the energy of γ rays) and a flux as high as 5 x 10^7 γ rays per second (depending on the electron beam energy and the cavity mirror qualities).

We used the OK-4 FEL e-beam diagnostics to study and improve both temporal and spatial characteristics of the electron and optical (FEL) beams. Improvements in the quality of both the optical and the electron beams allowded generation of γ-ray beams with substantially better quality (higher energy resolution and flux). The dependence of the FEL power and the γ-ray flux on the beam parameters is in close agreement with theory. The good agreement between theory and experiments gives us confidence both in the OK-4/Duke SR FEL and in our theoretical predictions.

The transverse mode quality of the laser beam from the OK-4 FEL is extraordinary good – it is rather easy to obtain perfect TEM_{00} mode with a Fourier limited transverse distribution. It is more complicated to obtain Fourier limited longitudinal modes, the so-called super-modes [Dattoli 1980]. The storage ring FEL operational parameters (such as lasing power, micro-pulse duration, lasing linewidth, etc.) are optimized at an exact synchronism between the electron and the optical bunches. A streak-camera with picosecond resolution was used to study the dynamics and the evolution of the micro- and the macro-temporal structures of the OK-4 FEL. With optimal tuning, Fourier limited longitudinal micropulses (super-modes) as short as 1.4 psec RMS and laser spectra with linewidths as narrow as 9×10^{-5} FWHM were observed. However, fluctuations in the electron beam, as well as noise in the ring magnet power supplies and RF system prevented the routine

attainment of stable and longitudinally Fourier limited FEL operation. Further improvements to the Duke storage ring and the OK-4 FEL systems are required to obtain better stability.

The stability of the optical cavity also determines the stability of the optical beam inside the resonator. We studied the stability of the optical resonator to estimate the criterion for lasing. A long near-concentric optical cavity can reduce thermal loads on the cavity mirrors caused by the high-order harmonics of the spontaneous radiation generated in the wiggler, but this reduction comes at the expense of a high sensitivity to angular misalignments. A mirror feedback system was constructed to maintain angular tolerances of better than ~ μrad.

The mechanical and chemical stability of the mirrors used in the optical cavity of the Duke/OK-4 FEL is extremely important. The study of mirror degradation allowed us to choose cavity mirror materials which are stable for the severe conditions imposed by the OK-4/Duke FEL system. The proper choice of materials for mirror coatings played an important role in reducing cavity losses and reflectivity degradation at wavelengths below 200 nm. It also played a main role in providing the conditions for long term operation of the OK-4 FEL in the deep-UV and visible ranges. The downstream cavity mirror which is exposed to severe conditions (~ 30 W of soft x-ray spontaneous radiation from the OK-4 wigglers) demonstrated changes in its spectral features (shift of reflectivity band) due to high temperature effects. A mirror cooling system and/or protection from the high harmonic radiation from the FEL wigglers will be required to solve these problems.

1.5 γ-ray generation via Compton Backscattering

Conventional Compton γ-ray and x-ray sources use ultra-relativistic electron beams and conventional lasers. The main limitations for these conventional Compton γ-ray sources using two independent systems are limited energy resolution (especially for low energy γ rays) and the flux limitations imposed by the necessity to "tag" lost electrons.

The γ-ray generation via intra-cavity Compton backscattering in FELs opens up new possibilities in nuclear physics and in other applications because of the high flux and high energy resolution compared to conventional γ-ray sources. The tunability and the energy resolution of the Compton γ rays depend on the characteristics of the incident electron and photon beams. In the Duke γ-ray source the electron beam energy is much higher than the photon energy and the quality of γ rays is dominated by the electron beam quality. The energy spread of γ rays in the Duke source is determined chiefly by the induced energy spread of the electron beam due to the FEL interaction. The low emittance of the electron beam in our system allows a much better γ-ray beam quality than other existing systems. In addition, the large energy acceptance of the Duke storage ring provides for a "no-loss" mode of operation over a wide range of γ-ray energies. In this "no-loss" mode, the γ rays can be generated without reducing the beam lifetime. Figure 1.3.1 shows the tunability of the γ-ray energy in the Duke/OK-4 Storage Ring FEL. For low energy γ rays, we

operate the FEL at longer wavelengths, whereas, for high energy γ rays, we operate the FEL at short wavelengths and at high electron beam energies.

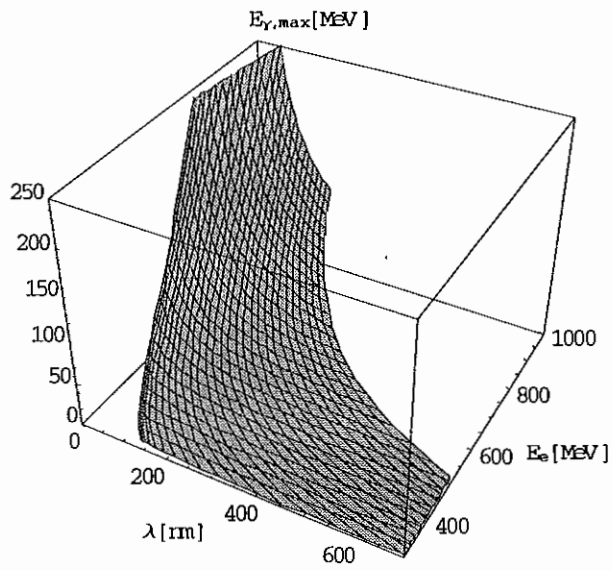

Figure 1.3.1 Tunability of γ-ray energy in the Duke/OK-4 storage ring FEL. Currently achievable tuning range of γ-ray energy is from 2 to 55 MeV.

The geometry of the OK-4/Duke SR FEL system requires at least two electron bunches in order to generate γ rays. The successful generation of γ-ray beams by operating the Duke storage ring with two and four equally spaced electron bunches has been demonstrated. The performance of the OK-4/Duke SR FEL γ-ray source, the measured parameters of γ-ray beams (including the photo image of γ rays showing their spatial distribution), and their dependence on parameters of the

electron and the optical beams agreed well with the theoretical calculations. Therefore, plans for improvements and for application of this unique system can proceed with confidence.

Chapter 2

Storage Ring FELs: Theory

2.1. Introduction

Beams of relativistic electrons (or positrons) used for FEL operation can be produced by a variety of accelerator. The use of heavier charged particles such as protons for FELs is disadvantageous – heavy charged particles do not radiate as efficiently as electrons or positrons. The most popular means to generate electron beams are rf linear accelerators, storage rings, microtrons and electrostatic accelerators. The main advantage of storage rings as compared to single pass accelerators (such as linacs) is the re-circulation and the re-use of the same electron beam for many passes. This is the main reason why storage rings can provide electron beams with large average currents.

In addition, the synchrotron radiation in an electron storage ring provides the radiation damping responsible for the reduction of both the transverse emittance and the energy spread of the electron beam. For many years storage rings provided the lowest available transverse emittances of electron beams, which is the reason why storage rings are popular in short wavelength FELs. Only in recent years have new linac technologies utilizing photo-cathode injectors competed with storage rings for lower transverse emittance. However, the use of storage rings as FEL drivers limits

the average lasing power and efficiency of the FEL. This limitation (which was first derived by N.A.Vinokurov [Vinokurov 1977], but is known as the Renieri limit [Renieri 1979]) is caused by re-using the same electron beam whose energy spread increases after each pass through the FEL due to beam interactions with the FEL. The decrease in the FEL gain caused by the growth in the energy spread limits the maximum lasing power of the storage ring FEL. Nevertheless, the average lasing power in the storage ring FELs can easily compete with conventional lasers, especially at short wavelengths.

There are three processes in a storage ring FEL which need to be considered:

i) the effect of the FEL interaction on the electron beam;

ii) the evolution of an FEL optical field due to the interaction with the electron beam;

iii) the evolution of the distribution function of the electron beam in six dimensional phase space in a storage ring.

All three effects must be evaluated to find self-consistent parameters of the system. An electron entering the FEL wiggler interacts with the optical field and radiates an electromagnetic wave. The FEL wiggler is a magnet with a periodic magnetic field along the trajectory of the electron beam. The FEL wavelength (i.e., the wavelength of optical field) and the wiggler parameters (i.e., the wiggler period and its field) should satisfy resonant conditions to provide for effective interaction between the electrons and the optical field. The resonant condition is created by tuning the FEL wiggler so that the interaction between the electron and the FEL optical field repeats itself for each period of the wiggler. In this resonant case, the electron exchanges

energy with the FEL optical field depending on the initial phase between the electron's oscillation in the FEL's wiggler and the FEL optical field. After passing through the FEL interaction region, the electron beam circulates around the storage ring which consists of focusing magnets, bending magnets, and an RF cavity; the optical beam travels back and forth inside the optical resonator. If the period of the round trip of the electron bunch in the storage ring and the optical pulse in the optical resonator (cavity) are equal, they overlap and interact in the FEL interaction region at each pass. This condition is called synchronism. If the FEL gain exceeds the losses in the optical cavity, the power of the optical pulse grows on each pass until saturation.

The lack of highly reflective mirrors in the short wavelength range demands a high gain for a short wavelength FEL. One way to maximize the gain is the use of long FEL wigglers since a longer wiggler provides more periods for bunching. The length of the FEL, however, is limited by the length of the straight section in the ring and the matching of the size and angular spread of the electron beam.

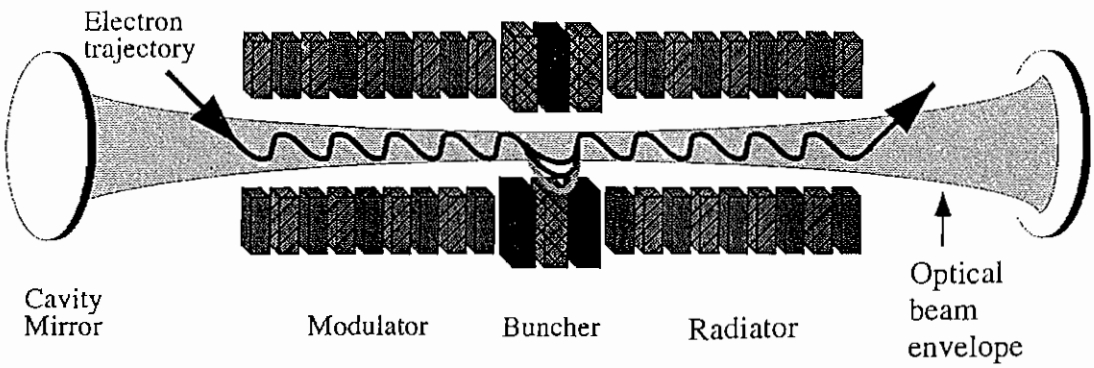

Fig. 2.1.1 Schematic layout of optical klystron.

A modification of the conventional FEL – an Optical Klystron (OK) [Vinokurov 1977] (see Figure 2.1.1) – enhances FEL gain in a compact FEL system. An OK takes advantage of the high quality of the electron beam characterized by a small energy spread. The optical klystron consists of two wigglers separated by a bunching section (sometimes called a dispersion section). The use of the bunching section provides for optimal bunching conditions and a "separation of functions" between the two wigglers.

The gain of an optical klystron can be substantially higher than the gain of a conventional FEL using the same wigglers. In the case of the OK-4/Duke SR FEL, this enhancement is 5 to 10 times the conventional FEL gain depending on the specific beam parameters. The higher gain of the optical klystron scheme is attractive for most storage ring FELs where the quality of the electron beam is high.

2.2. The optical klystron

The optical klystron, a modification of the conventional FEL which consists of one continuous wiggler, is designed to improve the FEL gain that develops from the coherent electron bunching. A buncher consists of one period of deflecting magnets. The transit time of the electrons in a buncher depends on their energy. Unlike in a conventional one-wiggler FEL, in the optical klystron the functions of modulation and radiation are separated into energy modulation, density modulation, and coherent radiation.

This separation of functions is illustrated in Figure 2.2.1 by Poincare plots in the (φ, ε/E_0) phase space. The electrons enter the first wiggler with some energy spread and random phases (Figure 2.2.1(a)). Passing through the first wiggler, electrons may lose or gain energy depending on the phase between the electrons' motion and the optical field (Figure 2.2.1(b)). In the bunching section, higher energy electrons in the back will catch up with the slower moving lower energy electrons in front, transforming the energy modulation (developed from the first wiggler) into the density modulation (Figure 2.2.1(c)). If the phase delay between the two wigglers is chosen correctly, most of the electrons entering the second wiggler will lose energy and amplify the optical beam. Electrons bunched on a scale of optical wavelength λ will radiate coherently (Figure 2.2.1(d)) and the radiation will interfere constructively with the FEL optical field. After one turn in the storage ring, all electrons lose their phase correlations (on the scale of optical wavelength) and the modulations wash out causing growth of the longitudinal phase space volume (see Fig. 2.2.1(e)). The growth of the longitudinal phase space volume corresponds to growth in the energy spread and bunch length of the electron beam. The growth rate of the energy spread is directly proportional to the power generated in the FEL. An increase of the energy spread reduces the FEL gain and causes power saturation in storage ring FELs. The growth of the energy spread and the FEL lasing power continues until the FEL gain is equal to the losses in the optical cavity. Zero net gain (i.e., FEL gain minus the cavity losses) provides one of the conditions for saturation in the SR FEL – the FEL lasing power stops growing and becomes constant.

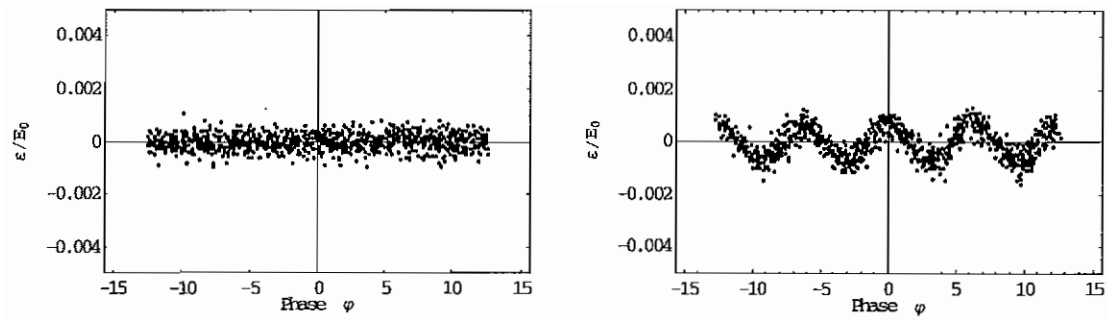

(a) Initial distribution

(b) Energy modulation

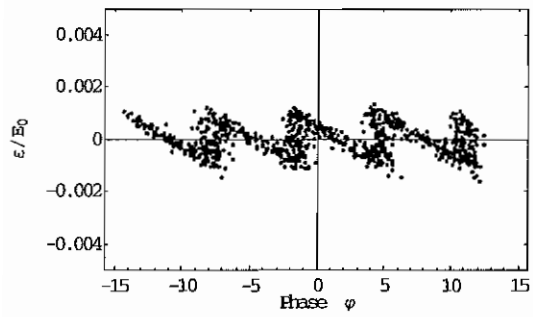

(c) Density modulation

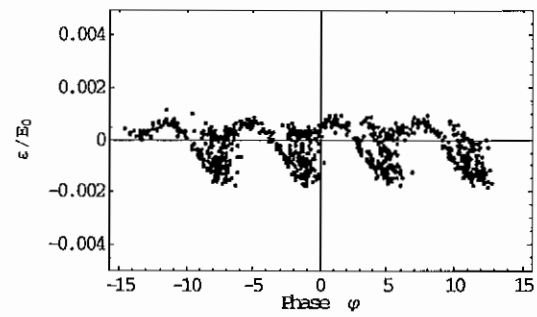

(d) Coherent radiation

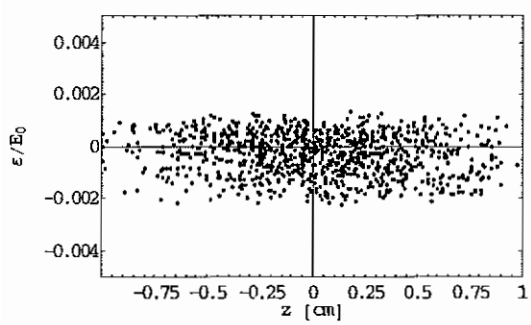

(e)-1

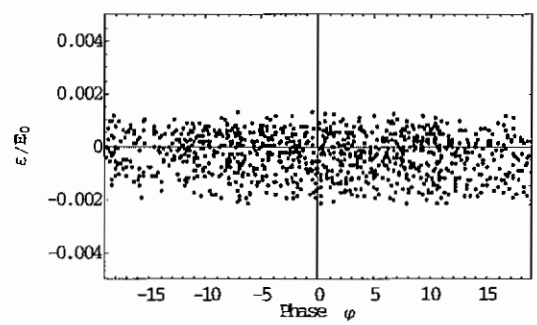

(e)-2

(e) Distribution after one turn through the ring. (1: in (z, ε/E_0); 2: in (φ, ε/E_0)) After one turn, the coherent bunching on a scalc of optical wavelength is washed out and the energy spread is increased due to the FEL interaction.

Fig. 2.2.1 Evolution of electron beam distribution in phase space (φ, ε/E_0) in the optical klystron.

Spontaneous radiation from the wigglers is a source for the start-up of the FEL oscillator and can be used to evaluate the quality of the electron beam and the wigglers. The frequency and angular distribution of the radiation from the wiggler depend on the characteristics of the wigglers and the electron beam. The radiation is emitted into a forward cone with an angular divergence of approximately K_w/γ, where K_w is the wiggler parameter.

The power spectrum of the spontaneous emission from an electron traveling in the wiggler can be calculated from the Liénard-Wiechert potentials. In the far field, the power spectrum in the frequency range $d\omega$ and solid angle $d\Omega$ about the direction of observation $\hat{\mathbf{n}}$ is [Jackson 1975]:

$$\frac{d^2I}{d\omega d\Omega} = \frac{e^2\omega^2}{4\pi^2 c}\left|\int dt\, \hat{\mathbf{n}}\times\left(\hat{\mathbf{n}}\times\vec{\beta}(t)\right)\exp\left[i\omega\left(t-\frac{\hat{\mathbf{n}}\cdot\vec{\mathbf{r}}(t)}{c}\right)\right]\right|^2, \qquad (2.2.1)$$

where $\vec{\mathbf{r}}(t)$ and $\vec{\beta}(t)$ are the position and the velocity of the electron at time t. In the optical klystron, the wave packet of spontaneous radiation from the second wiggler is delayed by a time corresponding to the total slippage of the electron, Δs. Slippage is defined as the path difference along the z-axis (direction of propagation of electron and optical pulses) between the optical pulse traveling at the speed of the light and the electron, which is traveling at a slightly smaller velocity. The radiation from a one period buncher is weaker and broader than that from the N_w period wiggler. Because of the high K_w value in the buncher, the resonant frequency of the buncher is much lower than that for the wigglers. As a result, we neglect the radiation from the buncher. The power spectrum of the OK spontaneous radiation becomes

$$\left(\frac{d^2I}{d\omega d\Omega}\right)_{OK} = 2\cdot\left(\frac{d^2I}{d\omega d\Omega}\right)_{N_w}(1+\cos k\Delta s), \qquad (2.2.2)$$

where

$$\left(\frac{d^2I}{d\omega d\Omega}\right)_{N_w} = \frac{e^2\omega^2}{4\pi^2c^3}\left(\frac{K_w[J_0(\xi)-J_1(\xi)]L_w}{2\gamma}\right)^2\left(\frac{\sin(\delta kL_w/2)}{\delta kL_w/2}\right)^2,$$

$$\delta k = \left(\frac{k}{2\gamma^2}\left(1+\frac{K_w^2}{2}\right)-k_w\right), \text{ and } \xi = \frac{1}{2}\frac{K_w^2/2}{(1+K_w^2/2)},$$

$$\Delta s = (N_w + N_d)\lambda .$$

Here Δs is the slippage of electrons between the centers of the two wigglers, N_d is a dimensionless number characteristic of the bunching section representing the number of optical wavelengths passing over an electron in the bunching section, and k_w is the wave vector of the wiggler. The subscript N_w indicates the spectrum from one wiggler with N_w periods and the subscript *OK* denotes the optical klystron containing two wigglers with N_w periods and one buncher. The power spectrum of the spontaneous emission from the optical klystron has a fine structure inside the modulation envelope. The envelope is the same as for the wiggler with N_w periods. In a small-signal and low gain regime, the Einstein relation states that the gain is proportional to the derivative of the spectrum of spontaneous radiation with energy. In the case of a plane wave, we can easily explain the higher gain of an optical klystron as compared to that of a conventional FEL with the same number of wiggler periods. As shown in Figure 2.2.2, the gain of the optical klystron with an idealized

electron beam (zero energy spread) is substantially higher than a conventional FEL. Also the gain continues to increase as Δs increases.

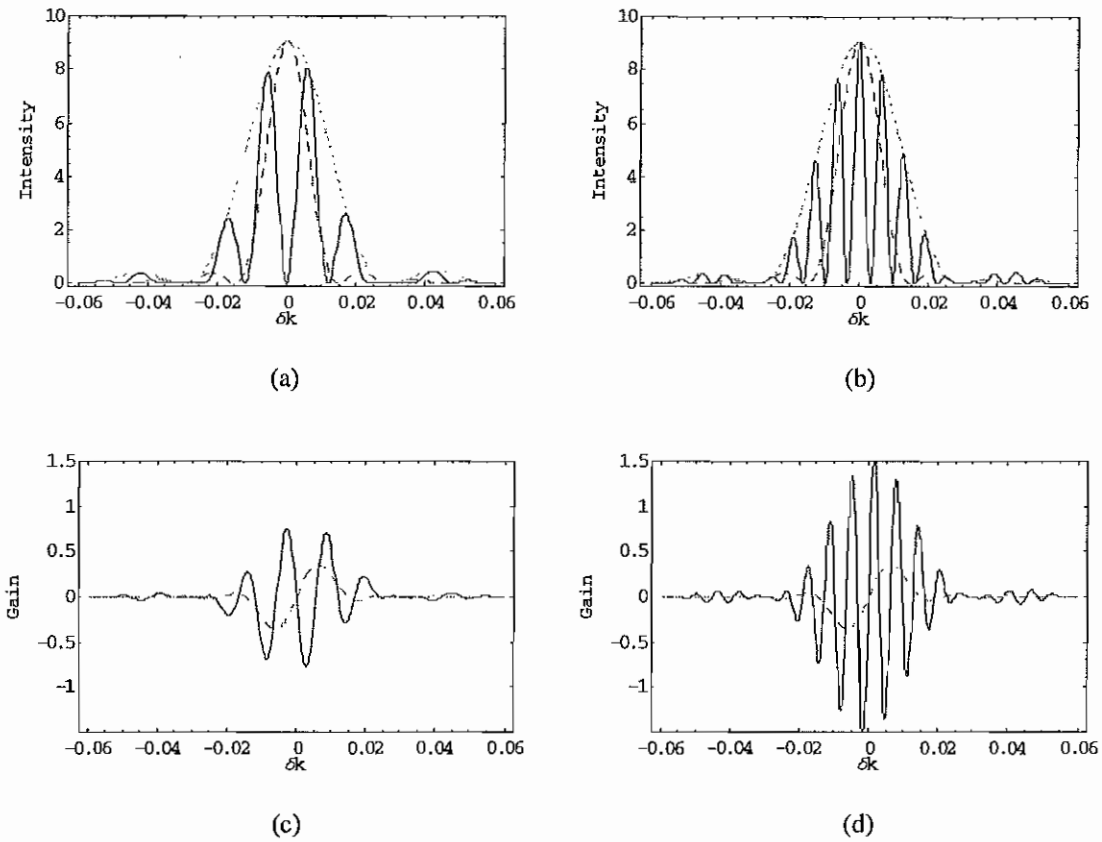

Fig. 2.2.2 Spontaneous emission spectra and their derivatives calculated theoretically. ((a) and (c): $N_d = 50$; (b) and (d): $N_d = 121.5$) Dashed curves are for the conventional FEL with $2N_w$.

For an electron bunch (or pulse), the power spectrum should be averaged over the electrons' distribution in phase space. While the gain is enhanced by use of stronger bunching, it also becomes sensitive to the energy spread in the electron

beam. These effects change the modulation depth of the spectrum. For an electron bunch, the power spectrum can be written as [Vinokurov 1977, Elleaume 1983]

$$\left(\frac{d^2I}{d\omega d\Omega}\right)_{OK} = 2\cdot\left(\frac{d^2I}{d\omega d\Omega}\right)_{N_w}(1+M\cdot\cos k\Delta s), \qquad (2.2.3)$$

where M is the modulation rate due to the energy spread, the angular spread, and the transverse size of the electron beam. For electron beams with low transverse emittances, the main effect on the modulation rate is caused by the energy spread. Figure 2.2.3 shows the influence of energy spread and emittance of the electron beam on the spontaneous radiation spectra. The modulation depth of fine structure with σ_ε = 0.05 % (Figure 2.2.3 (a)) becomes smaller than that with no energy spread (Figure 2.2.2 (b)), resulting in the reduction of gain. The spectrum of spontaneous radiation with angular spread becomes asymmetrical as shown in Figure 2.2.3 (b). We can see that the OK performance is sensitive to the energy spread of the electron beam.

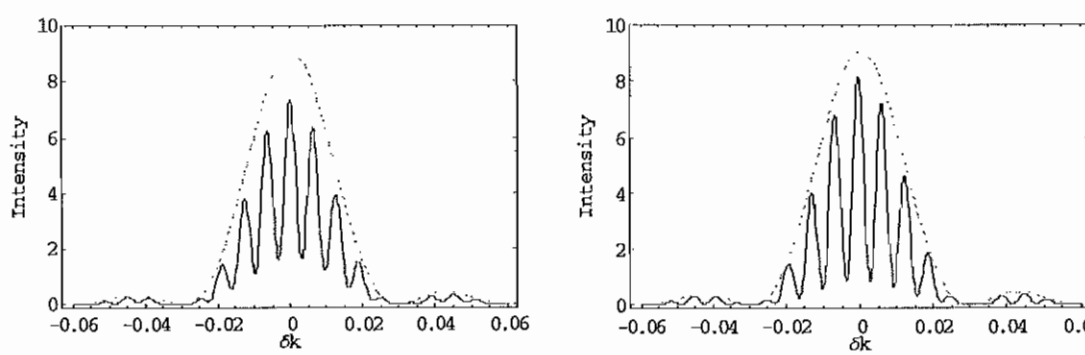

(a) (b)

Fig. 2.2.3 Spontaneous emission spectra depending on electron beam parameters.
((a): relative energy spread σ_ε = 0.05 %; (b): angular spread $\sigma_{x'}$ = 0.1 mrad)

2.3. The motion of electrons in the interaction region

As an electron travels along the axis of the wiggler, an alternating magnetic field forces the electron to oscillate sinusoidally and consequently to radiate. The equation of motion for the electron can be derived using the Hamiltonian or the Lorentz force equation. The magnetic field of a wiggler must satisfy Maxwell's equations. In the absence of electrons and in a vacuum,

$$\vec{\nabla}\cdot\vec{\mathbf{B}}=0 \quad \text{and} \quad \vec{\nabla}\times\vec{\mathbf{H}}=0 \tag{2.3.1}$$

where $\vec{\mathbf{H}}=\vec{\mathbf{B}}=\vec{\nabla}\times\vec{\mathbf{A}}$ and $\vec{\mathbf{H}}=-\nabla\Psi_M$. $\vec{\mathbf{A}}$ is the vector potential and Ψ_M is the magnetic scalar potential. The magnetic scalar potential is a solution of the Laplacian equation satisfying the boundary conditions of the different magnet designs. An ideal planar wiggler (similar to the OK-4 FEL) is much wider (~ cm) in the x-direction than the electron transverse size (sub-millimeter). Hence one can neglect the x-dependence of the magnetic field. The periodicity and symmetry condition about the *xz*-plane leads to the solution of the magnetic scalar potential Ψ_M as

$$\Psi_M(y,z)=\sum_{\substack{n=1\\ n=odd}}^{\infty} A_n\cos(nk_w z)\sinh(nk_w y),$$

$$A_x(y,z)=\sum_{\substack{n=1\\ n=odd}}^{\infty} A_n\sin(nk_w z)\cosh(nk_w y),\ A_y=0=A_z, \tag{2.3.2}$$

where k_w is the wave vector of the wiggler, $2\pi/\lambda_w$. Planar wigglers are usually designed to support only the fundamental harmonic of the field. Dropping the higher

order terms in the summation, one computes for the vector potential and magnetic field of a planar wiggler:

$$A_x(y,z) \approx \frac{B_0}{k_w}\sin(k_w z)\cosh(k_w y),\ A_y = 0 = A_z \tag{2.3.3}$$

$$B_x = 0,\ B_y \approx B_0\cos(k_w z)\cosh(k_w y), \text{ and } B_z \approx -B_0\sin(k_w z)\sinh(k_w y). \tag{2.3.4}$$

Because the $\hat{y}$ component involves a hyperbolic function term, the electrons in the interaction region experience focusing in the $\hat{y}$ direction.

The Hamiltonian of an electron in the external field is

$$\mathcal{H}(\vec{\mathbf{r}},\vec{\mathbf{P}},t) = \left[m^2c^4 + c^2\left(\vec{\mathbf{P}} - \frac{e}{c}\vec{\mathbf{A}}\right)^2\right]^{1/2},\ \vec{\mathbf{P}} = \vec{\mathbf{p}} + \frac{e}{c}\vec{\mathbf{A}}, \tag{2.3.5}$$

where $\vec{\mathbf{r}}$ and $\vec{\mathbf{P}}$ are canonical variables. From the Hamiltonian equation, we can derive the electron motion in the wiggler [Brau 1990, Litvinenko 1989]. In fact, the vector potential is the superposition of the magnetic field and the optical field. However, the influence of the optical field on the electron's trajectory is small compared to that of the wiggler's magnetic field. Therefore, the motion of the electron is mostly governed by the magnetic field of the wiggler and the interactions with the optical field can be treated as perturbations. Because the magnetic field is independent of the x direction, P_x is a constant of motion. Introducing the variable s for the electron path, $s = vt$, and using $'$ for d/ds and $\dot{}$ for d/dt, the velocity of the electron can be written as:

$$x' = x_0' - \frac{e}{pc}A_x(y,z) = x_0' - \frac{K_w}{\gamma\beta}\sin(k_w z)\cosh(k_w y), \tag{2.3.6}$$

$$z' = \left(1 - x'^2 - y'^2\right)^{1/2} \approx 1 - \frac{1}{2}x'^2 - \frac{1}{2}y'^2, \ (x_0', y', \text{and } K_w/\gamma << 1), \quad (2.3.7)$$

where $K_w = \dfrac{eB_0}{k_w mc^2}$ is the wiggler parameter. For an ideal case, i.e., $y = 0$ and $x_0' = 0$

$$x' = -\frac{K_w}{\gamma\beta}\sin(k_w z) \quad (2.3.8)$$

$$z' = 1 - \frac{K_w^2}{4\gamma^2\beta^2} + \frac{K_w^2}{4\gamma^2\beta^2}\cos(2k_w z). \quad (2.3.9)$$

The trajectory of an electron in the xz-plane is described by

$$x \approx x_0 + x_0' z + \frac{K_w}{k_w\gamma\beta}\cos(k_w z) \quad (2.3.10)$$

$$s \approx s_0 + \left(1 + \frac{K_w^2}{4\gamma^2\beta^2}\right)z - \frac{K_w^2}{8k_w\gamma^2\beta^2}\sin(2k_w z). \quad (2.3.11)$$

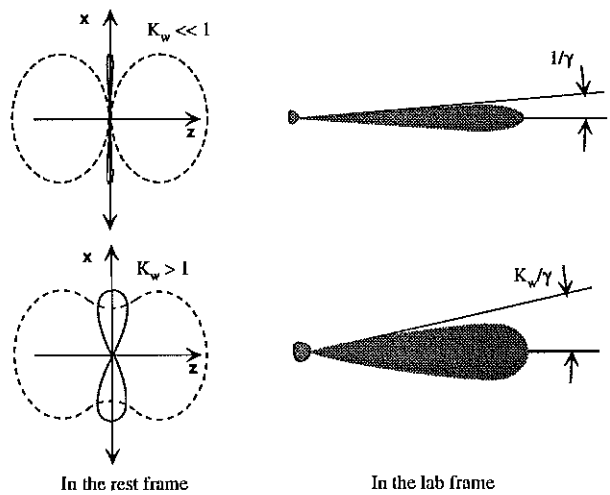

Fig. 2.3.1 Oscillatory motion of an electron in the rest frame and the electron's radiation in the lab frame.

Oscillations of the longitudinal velocity (in z-direction) occur at twice the frequency of oscillation in the x-direction. This effect is responsible for the appearance of odd harmonics of the fundamental frequency in the on-axis radiation of a planar wiggler. Figure 2.3.1 shows the motion of an electron in the rest frame and the corresponding radiation in the lab frame. When $K_w << 1$, the amplitude of the oscillation in the z-direction is much smaller than in the x-direction, and so the electron produces dipole radiation. When $K_w > 1$, the amplitude in z is comparable to the amplitude in the x-direction, and so the electron produces multipole radiation. The symmetric form of the radiation pattern in the rest frame is stretched in the forward direction of the lab frame forming cones of angle $\theta = \gamma^{-1}\sqrt{1+K_w^2/2}$. The radiated frequency is $2\gamma_{\parallel}^2(1+2m)k_w$(m: integer number, $\gamma_{\parallel} = \gamma/\sqrt{1+K_w^2/2}$) and therefore only odd harmonics appear along the axis of the planar wiggler.

The equation of motion in the $\hat{y}$-direction is

$$\ddot{y} = \frac{d}{dt}\frac{\partial \mathcal{H}}{\partial P_y} = -\frac{1}{\gamma m}\frac{\partial \mathcal{H}}{\partial y} = x'\frac{ep}{\gamma^2 m^2 c}\frac{\partial A_x(y,z)}{\partial y} \tag{2.3.12}$$

and, hence,

$$y'' = x_0'\frac{e}{pc}\frac{\partial A_x(y,z)}{\partial y} - \frac{1}{2}\left(\frac{e}{pc}\right)^2\frac{\partial A_x{}^2(y,z)}{\partial y}$$

$$y'' + \frac{\partial}{\partial y}\left(\frac{1}{2}\left(\frac{eA_x}{pc}\right)^2 - x_0'\frac{eA_x}{pc}\right) = 0 \tag{2.3.13}$$

Considering the classical Hamiltonian with s as independent variable, and averaging

over one wiggler period λ_w while keeping only the lowest order term in y, we arrive at:

$$\left\langle \mathcal{H}_y \right\rangle_{\lambda_w} = \frac{1}{2}\left\langle y'^2 \right\rangle_{\lambda_w} + \frac{1}{2}\left\langle \left(\frac{eA_x}{pc} \right)^2 \right\rangle_{\lambda_w} \cong \frac{1}{2}\left\langle y'^2 \right\rangle_{\lambda_w} + \frac{1}{4}\left(\frac{eB_0}{pc} \right)^2 y^2 . \qquad (2.3.14)$$

The equations of motion resulting from this Hamiltonian are the equations of betatron motion,

$$y'' + y^2 \Big/ \beta_w^2 = 0 , \qquad (2.3.15)$$

where $\beta_w = \dfrac{\sqrt{2}\gamma\beta}{k_w K_w}$ is the beta function of the wiggler. Hence, the solution is

$$y = y_0 \cos(z/\beta_w) + y_0' \beta_w \sin(z/\beta_w) \qquad (2.3.16)$$

$$y' = y_0' \cos(z/\beta_w) - y_0 \beta_w^{-1} \sin(z/\beta_w) \qquad (2.3.17)$$

From Equation 2.3.7, one calculates the slippage between the electron and the optical pulse, i.e., $ct(z) - z$:

$$ct(z) = \beta^{-1} \int dz \left(1 - x'^2 - y'^2\right)^{-1/2} \approx \beta^{-1} \int dz \left(1 + \frac{1}{2}(x_0' - \frac{e}{pc} A_x(y,z))^2 + \frac{1}{2} y'^2 \right). \qquad (2.3.18)$$

Since the motion in the y-direction is slowly varying compared to the fast oscillatory motion in the x-direction, we can consider an averaging over one wiggler period. Then, using Taylor's expansion for $A_x(y, z)$, $A_x(y,z) \approx A_x(0,z)(1 + k_w^2 y^2/2)$ and $A_x^2(y,z) \approx A_x^2(0,z)(1 + k_w^2 y^2 + O(y^4))$, after averaging all terms including y or y' in Equation 2.3.18 over one wiggler period, one obtains

$$\frac{1}{2}\left\langle y'^2\right\rangle_{\lambda_w}+\frac{1}{2}\left\langle\left(\frac{\sqrt{2}ek_w}{pc}A_x(0,z)y\right)^2\right\rangle_{\lambda_w}\approx\frac{1}{2}y_0'^2+\frac{y_0^2}{2\beta_w^2}$$

and

$$\left\langle y^2A_x(0,z)\right\rangle_{\lambda_w}=0. \tag{2.3.19}$$

Integrating along z yields

$$ct(z)-z\approx\frac{1}{2\gamma^2}\left(1+\frac{K_w^2}{2}\right)z+\left(\frac{1}{2}x_0'^2+\frac{1}{2}y_0'^2+\frac{y_0^2}{2\beta_w^2}\right)$$

$$-\frac{x_0'K_w}{\gamma k_w}\cos(k_wz)-\frac{K_w^2}{8\gamma^2k_w}\sin(2k_wz), \tag{2.3.20}$$

where

$$\beta=\left(1-\frac{1}{\gamma^2}\right)^{1/2}\approx1-\frac{1}{2\gamma^2}. \tag{2.3.21}$$

For an ideal electron (or a synchronous electron with $x_0'=y_0'=y_0=0$), the total slippage past one wiggler is $N_w\lambda_{0,op}$ and, where N_w ($=L_w/\lambda_w$) is the number of wiggler periods and $\lambda_{0,op}$ is the resonant optical wavelength radiated by the electron:

$$\lambda_{0,op}=\frac{\lambda_w}{2\gamma_0^2}\left(1+\frac{K_w^2}{2}\right), \tag{2.3.22}$$

where the subscripts "0" and "*op*" denote ideal electron and optical wavelength, respectively.

In an optical klystron, electrons pass through the bunching section after passing the first wiggler. The dispersion section consists of three poles of strong magnetic field that produce a one period oscillation. The path length of the electrons

in the magnetic field depends on their energy. Similar to the wiggler, the slippage of a synchronous electron (i.e., ideal electron) is $\lambda_{BS,op}$ (subscript BS denotes "bunching section"), i.e.,

$$\Delta s_{0,BS} = \lambda_{BS,op} = \frac{\lambda_{BS}}{2\gamma_0^2}\left(1+\frac{K_{BS,w}^2}{2}\right), \tag{2.3.23}$$

where λ_{BS} is a period of the magnetic field in the bunching section and $K_{BS,w}$ is the wiggler parameter in the bunching section. Then, the total slippage of a synchronous electron past the buncher section is $\Delta s_0 = (N_w + N_d)\lambda_{0,op}$. For an arbitrary electron with energy E, there is an additional slippage depending on the variation in electron energy, $(\varepsilon + \Delta E)\cdot ds/dE$, where ε is the energy deviation from the synchronous electron energy (i.e., $\varepsilon = E - E_0$, where E_0 is the energy of synchronous electron) and ΔE is the energy change due to the interaction with optical fields in the first wiggler. Thus the total slippage is given by

$$\Delta s = \Delta s_0 + (\varepsilon + \Delta E)\frac{ds}{dE}. \tag{2.3.24}$$

In case of $N_w << N_d$ and $\Delta E << 1$, by differentiating the total slippage Δs with respect to E or γ,

$$\Delta s = (N_w + N_d)\frac{\lambda_w}{2\gamma_0^2}\left(1+\frac{K_w^2}{2}\right)\left(1+\frac{\delta\gamma}{\gamma_0}\right)^{-2}, \tag{2.3.25}$$

$$\frac{ds}{dE} = -\frac{2}{E}(N_w + N_d)\frac{\lambda_w}{2\gamma^2}\left(1+\frac{K_w^2}{2}\right) = -\frac{2\Delta s}{E}, \tag{2.3.26}$$

we obtain

$$\Delta s \approx \Delta s_0 - (\varepsilon + \Delta E)\frac{2\Delta s_0}{E_0}. \qquad (2.3.27)$$

For electrons entering the interaction region with a different position or angle than the synchronous electron on the axis, the second term in Equation 2.3.20 must be included. This slippage of an ultra-relativistic electron is the main cause of the FEL lethargy effect. We will discuss this effect further in the next section.

The basic equations of the electron motion will be used next for calculating the evolution of the optical field due to the FEL interaction.

2.4. The evolution of optical fields

The evolution of an optical field in the presence of an electron current can be derived from Maxwell's equations. The radiation fields inside the optical cavity (resonator) satisfy the wave equations:

$$\left(\nabla^2 - \frac{1}{c^2}\frac{\partial^2}{\partial t^2}\right)\vec{\mathbf{A}}(\vec{\mathbf{r}},t) = -\frac{4\pi}{c}\vec{\mathbf{j}}(\vec{\mathbf{r}},t), \quad \vec{\mathbf{j}}(\vec{\mathbf{r}},t) = -e\sum_{i=1}^{n_e}\vec{\mathbf{v}}_i(t)\,\delta\left(\vec{\mathbf{r}} - \vec{\mathbf{r}}_i(t)\right) \qquad (2.4.1)$$

$$\left(\nabla^2 - \frac{1}{c^2}\frac{\partial^2}{\partial t^2}\right)\phi(\vec{\mathbf{r}},t) = -4\pi\rho(\vec{\mathbf{r}},t), \qquad \rho(\vec{\mathbf{r}},t) = -e\sum_{i=1}^{n_e}\delta\left(\vec{\mathbf{r}} - \vec{\mathbf{r}}_i(t)\right). \qquad (2.4.2)$$

$\vec{\mathbf{A}}(\vec{\mathbf{r}},t)$ and $\phi(\vec{\mathbf{r}},t)$ are the vector and the scalar potentials and $\vec{\mathbf{j}}(\vec{\mathbf{r}},t)$ and $\rho(\vec{\mathbf{r}},t)$ are the current and charge densities. Typically, the paraxial approximation with slowly varying amplitude and phase (which is a good assumption for the coherent and monochromatic optical field) is used to solve the wave equation in laser physics. In this approximation, the vector potential can be written as $\vec{\mathbf{A}}(\vec{\mathbf{r}},t) = \hat{\mathbf{e}}\,k^{-1}E(\vec{\mathbf{r}},t)e^{i(kz-wt)}$

($\hat{\mathbf{e}}$: complex polarization vector) and the second order wave equation can be reduced to the paraxial equation. The polarization is chosen to match that of the spontaneous radiation from the wigglers and $\hat{\mathbf{e}} = \hat{\mathbf{x}}$ for a planar wiggler. When an electron beam is bunched due to interaction with the FEL, the non-uniform longitudinal charge distribution produces a longitudinal electric field. However, in the Compton regime (in a small-signal, ultra-relativistic case, $\gamma >> 1$) the space charge effect is negligible. Therefore, for the case of a short wavelength FEL, we neglect the scalar potential. Assuming the existence of a complete and orthogonal set of eigenmodes (which is reasonable for a system with negligible diffraction losses), the optical field inside the resonator can be expressed as a linear combination of eigenmodes as follows:

$$\vec{\mathbf{E}}(\vec{\mathbf{r}},t) = Re\,\hat{\mathbf{x}}\sum_{l,m} A_{lm}(ct-z,t)E_{lm}(\vec{\mathbf{r}})\cdot e^{ik(z-ct)}\,, \tag{2.4.3}$$

where $A_{lm}(ct-z,t)$ is the slowly varying complex amplitude and $E_{lm}(\vec{\mathbf{r}})$ is a time-independent homogeneous solution of the paraxial equation [Siegman 1986]:

$$\left(\frac{\partial^2}{\partial x^2}+\frac{\partial^2}{\partial y^2}+2ik\frac{\partial}{\partial z}\right)E_{lm}(\vec{\mathbf{r}})=0 \tag{2.4.4}$$

$$E_{lm}(\vec{\mathbf{r}}) = \frac{1}{\sqrt{2^{l+m-1}\pi l!m!}}\left(\frac{\beta_0/w_0}{\beta_0-iz}\right)\left(\frac{\beta_0+iz}{\beta_0-iz}\right)^{\frac{(l+m)}{2}} H_l\left(\frac{\sqrt{2}x}{w(z)}\right)H_m\left(\frac{\sqrt{2}y}{w(z)}\right)e^{-\frac{k}{2}\frac{x^2+y^2}{\beta_0-iz}} \tag{2.4.5}$$

$$\int dxdyE^*_{l'm'}(\vec{\mathbf{r}})E_{lm}(\vec{\mathbf{r}}) = \delta_{l'l}\delta_{m'm} \text{ (orthonormality relation).} \tag{2.4.6}$$

Here, $E_{lm}(\vec{\mathbf{r}})$ describes the transverse modes in the Hermite-Gaussian form (appropriate for an arbitrary transverse electron distribution), $H_{l,m}$ is the Hermite

polynomial, β_0 is the Rayleigh range, and $w(z)$ is the waist at the position z, which is the transverse mode size of a Gaussian beam. The waist is defined as,

$$w^2(z) = w_0^2\left(1+\frac{z^2}{\beta_0^2}\right),$$

where $w_0 = \sqrt{\frac{\beta_0\lambda}{\pi}}$ is the waist at the focal point with the wave number $k = \frac{2\pi}{\lambda}$. The subscripts l and m are the transverse mode numbers. It is easy to include higher harmonics by changing $k \rightarrow nk$ (n: harmonic number).

Substituting Equation 2.4.3 into the wave equation (Equation 2.4.1) the optical evolution equation in the interaction region becomes:

$$\left(\frac{\partial}{\partial z}+\frac{1}{c}\frac{\partial}{\partial t}\right)A_{lm}(ct-z,t) = i\frac{2\pi}{c}\int dxdy\; j_x(\vec{\mathbf{r}},t)E_{lm}^*(\vec{\mathbf{r}})e^{-i(kz-wt)}$$

$$= -2i\pi e\sum_{i=1}^{n_e}\beta_{i,x}(t)E_{lm}^*\left(x_i(t),y_i(t),z\right)\cdot\delta\left(z-z_i(t)\right)\cdot e^{-i(kz-wt)}. \qquad (2.4.7)$$

By changing variables (z, t) to (η, τ) ($\eta = z - ct$, $\tau = t$) and integrating with respect to τ using the Dirac delta function,

$$\delta\left(f(x)\right) = \sum_i \delta(x-x_i)\left|\frac{df(x)}{dx}\right|^{-1}_{x=x_i} \quad \text{for } x_i \text{ satisfying } f(x_i) = 0,$$

one arrives at:

$$\Delta A_{lm}(\eta) = -2i\pi e\sum_{i=1}^{n_e}\frac{dx(z_i)}{dz_i}E_{lm}^*\left(x(z_i),y(z_i),z_i\right)\cdot e^{-ik\eta}\left|\frac{d\Sigma(z_i)}{dz_i}\right|^{-1}, \qquad (2.4.8)$$

where $\Sigma(z_i) = c\tau(z_i) - z_i$ is the slippage of the ith electron ($\frac{dx(z_i)}{dz_i}$ is set to zero outside of the interaction region). The summation is confined to electrons satisfying the condition that, for a given moment η, $\eta + \Sigma(z_i) = 0$ and $z_i \in (-L_{FEL}/2, L_{FEL}/2)$ (L_{FEL}: total length of the FEL interaction region; z = 0 at the center of the FEL interaction region. This means that only electrons arriving at time interval (η/c, $\eta/c - \Sigma_{tot}/c$) (Σ_{tot}: total slippage, $\Sigma_{tot} = \Sigma(L_{FEL}/2) - \Sigma(-L_{FEL}/2)$) contribute to the optical field $A_{lm}(\eta)$.

Equation 2.4.8 is the first derivation of the optical field in the FEL interaction region (including the slippage effect) that has been made directly from the paraxial wave equation. For the one electron case, this equation is the same as the equation derived from energy conservation [Litvinenko 1995d]. The additional factor of 2 in Equation 2.4.8 is due to difference in definition of the electric field.

$$\Delta A_{lm}^{(1)}(s_0 + \Sigma(z)) \equiv -i\pi \frac{eK_w[JJ]}{\gamma} e^{iks_0} E_{lm}^*(x(z), y(z), z) e^{i(k\Sigma(z) - k_w z)} \left| \frac{d\Sigma(z)}{dz} \right|^{-1}, \quad (2.4.9)$$

where

$$[JJ] = J_0(\xi) - J_1(\xi) \text{ with } \xi = \frac{K_w^2}{2(2 + K_w^2)}. \quad (2.4.10)$$

As the number of electrons contributing to the optical field $A_{lm}(\eta)$ is large (of order ~10^6 – 10^9 with the average current of less than 10 mA per bunch), the summation can be changed to an integral using the distribution function $f(\mathbf{X})$ of the electron beam.

$$\Delta A_{lm}(\eta) = -2i\pi e n_e \int d\mathbf{X} f(\mathbf{X}) \delta(\eta + \Sigma(z)) \frac{dx(z)}{dz} E^*_{lm}(x(z), y(z), z) e^{ik\Sigma(z)} \left| \frac{d\Sigma(z)}{dz} \right|^{-1},$$

(2.4.11)

where $\mathbf{X}^T = [x, x', y, y', z, \varepsilon]$ and n_e is the number of electrons in a bunch. Using Equations 2.3.6 and 2.3.20, one can calculate the wave packet radiated by an electron beam into the TEM_{lm} mode in the FEL interaction region.

The FEL gain can be derived using energy conservation. The energy lost by the electron is equal to the energy gained by the optical wave:

$$\Delta E_w = -n_e \int d\mathbf{X} f(\mathbf{X}) \Delta E_e(\mathbf{X}). \tag{2.4.12}$$

Therefore, the gain with TEM_{00} mode is expressed as:

$$G = \frac{\Delta E_w}{P_{in} / f_0} = -\frac{8\pi n_e}{c A_{00}^2} \int d\mathbf{X} f(\mathbf{X}) \Delta E_e(\mathbf{X}), \tag{2.4.13}$$

where P_{in} is the initial power before the interaction between the electron and the optical beam and f_0 is the revolution frequency. In a small signal regime, assuming that the distribution of the electron beam is a Gaussian and the optical wave is a horizontally polarized Gaussian wave packet, the gain is expressed as (for details, refer to [Litvinenko 1989 and 1995d, 1995e]):

$$G(s) \cong 2\pi \frac{I_{peak}}{I_A} \frac{K_w^2}{\gamma^2} \frac{L^2}{\lambda \beta_{eff}} \left[J_n(\xi) - J_{n+1}(\xi) \right]^2 k \left| \frac{ds}{dE} \right| mc^2 \exp\left[-\frac{1}{2} \left(k \frac{ds}{dE} \sigma_E \right)^2 \right]$$

$$\times \mathrm{Re}\langle FF \rangle \exp\left[i \left(k\Delta s_0 + \frac{\pi}{2} + \Delta\varphi \right) \right] \exp\left[-\frac{(s - s_0)^2}{2\sigma_s^2} \right], \tag{2.4.14}$$

where

$$\langle FF \rangle = \frac{\beta_{eff}}{\beta_0}\frac{1}{L^2}\int_{z_i}^{L}\int_{z_i}^{L} dzdu \exp[i\delta k(z+u)+i\chi]\frac{F_x(z,-u)F_y(z,-u)}{|1+i\,z/\beta_0|\cdot|1+i\,u/\beta_0|},$$

$$\beta_{eff} = \frac{L^2}{\beta_0}\Big/\left(\sinh^{-1}\frac{L}{\beta_0} - \sinh^{-1}\frac{z_i}{\beta_0}\right),$$

$$\delta k = \frac{k}{(2n+1)2\gamma^2}(1+K_w^2/2) - k_w + \frac{\beta_0}{\beta_0^2+z^2},\ \Delta\varphi = 2\tan^{-1}\frac{z_i}{\beta_0},$$

$$\chi(z) = \tan^{-1}\frac{z}{\beta_0} - z\cdot\left(\tan^{-1}\frac{L}{\beta_0} - \tan^{-1}\frac{z_i}{\beta_0}\right)\Big/(L-z_i),$$

$$I_{peak} = \frac{C_0}{\sqrt{2\pi}\sigma_s} I_{bunch},\ I_A = \frac{mc^3}{e},\ \beta_w = \frac{\sqrt{2}\lambda_w\gamma}{2\pi K_w},\ \xi = \frac{K_w^2}{2(2+K_w^2)},$$

$$F_{x,y}(z_1,z_2) = \frac{1}{\sqrt{\det W_{x,y}(z_1,z_2)}},$$

$$W_x(z_1,z_2) = \begin{bmatrix} \frac{1}{\beta_x\varepsilon_x} + \frac{k}{\beta_0 - iz_1} + \frac{k}{\beta_0 + iz_2} & \frac{kz_1}{\beta_0 - iz_1} + \frac{kz_2}{\beta_0 + iz_2} \\ \frac{kz_1}{\beta_0 - iz_1} + \frac{kz_2}{\beta_0 + iz_2} & \frac{\beta_x}{\varepsilon_x} + \frac{kz_1^2}{\beta_0 - iz_1} + \frac{kz_2^2}{\beta_0 + iz_2} \end{bmatrix},$$

$$W_y(z_1,z_2) =$$

$$\begin{bmatrix} \frac{1}{\beta_y\varepsilon_y} + \frac{k\cos^2(z_1/\beta_w)}{\beta_0 - iz_1} + \frac{k\cos^2(z_2/\beta_w)}{\beta_0 + iz_2} - ik\frac{z_1 - z_2}{\beta_w^2} & \frac{1}{2}\frac{k\sin(2z_1/\beta_w)}{\beta_0 - iz_1} + \frac{1}{2}\frac{k\sin(2z_2/\beta_w)}{\beta_0 + iz_2} \\ \frac{1}{2}\frac{k\sin(2z_1/\beta_w)}{\beta_0 - iz_1} + \frac{1}{2}\frac{k\sin(2z_2/\beta_w)}{\beta_0 + iz_2} & \frac{\beta_y}{\varepsilon_y} + \frac{k\beta_w^2\sin^2(z_1/\beta_w)}{\beta_0 - iz_1} + \frac{k\beta_w^2\sin^2(z_2/\beta_w)}{\beta_0 + iz_2} - ik(z_1 - z_2) \end{bmatrix}.$$

Here, F_x and F_y represent the effects of the x and y emittances of the electron beam.

The optical beam travels between two mirrors in the optical cavity and is amplified to saturation with each pass in the FEL. The time structure of the optical beam is determined by that of the electron beam. Typically, electron beams in RF based linacs or storage rings are bunched, i.e., they are not continuous. Similarly, the

time structure of these bunched electron beams is imprinted on the optical beams in the FELs. In this case, we express the laser field in terms of the longitudinal modes of the optical cavity. For typical FELs, there are a large number of coupled longitudinal modes. For example, the number of modes $N \geq L_c / \sigma_z$ (L_c: cavity length, σ_z: electron bunch length) for the Duke/OK-4 SR FEL (L_c = 53.73 m and $\sigma_z \approx$ 1 ~ 3 cm) is approximately 10^3. To simplify the description of these 10^3 modes, supermodes were first introduced by Dattoli *et. al.* [Dattoli 1981a, 1981b]. Supermodes are defined as a configuration of spatial longitudinal modes that reproduce themselves after one passage through the interaction region. The lethargic response of the FEL gain medium (which is on the same time-scale as the slippage process) causes gain to occur dominantly on the trailing edge of the optical pulse. Over many passes, amplification of the optical pulse is shifted to the tail and the pulse group velocity is slower than c. To maximize the overlap between electron and optical pulses in the FEL interaction region, the optical cavity length should be slightly shortened to advance the optical pulse after each pass.

In the small-signal, small-gain regime, the propagation of the optical beam in each turn can be written as [Elleaume 1985, Litvinenko 1991]:

$$A_{m+1}(s+\delta) \cong A_m(s)\left(1-\frac{G_{th}}{2}\right)+\frac{G(s)}{2}A_m(s-\Sigma), \qquad (2.4.15)$$

where G_{th} is the cavity loss per turn and G(s) is the longitudinal gain profile. Σ is the FEL slippage and δ is the difference in separation between two successive electron bunches and the roundtrip cavity length of the optical beam. As the gain is

proportional to the peak current, the longitudinal gain profile depends on the longitudinal electron beam distribution. Since the optical bunch length is much shorter than the electron bunch length, we can expand $G(s)$ around the maximum value $G_0 = G(0)$:

$$G(s) \approx G_0(1-\frac{s^2}{2\sigma_s^2}), \tag{2.4.16}$$

where σ_s is the bunch length of the electron beam. In a long electron bunch, (i.e., σ_s $>> \Sigma$ or δ), we can assume that

$$\frac{1}{A(s)}\frac{\partial A(s)}{\partial s} << |\delta|^{-1}, \Sigma^{-1}. \tag{2.4.17}$$

Using Taylor's expansion, we can rewrite Equation 2.4.15 as:

$$\frac{\partial A(s,m)}{\partial m} + \xi(s)\frac{\partial A(s,m)}{\partial s} - \zeta(s)\frac{\partial^2 A(s,m)}{\partial s^2} - g(s)A(s,m) = 0, \tag{2.4.18}$$

$$\xi(s) = \frac{G_0\Sigma}{2}(1-\frac{s^2}{2\sigma_s^2}) + \delta,$$

$$\zeta(s) = \frac{G_0\Sigma^2}{4}(1-\frac{s^2}{2\sigma_s^2}) + \frac{1}{2}\delta^2,$$

$$g(s) = \frac{G_0}{2}(1-\frac{s^2}{2\sigma_s^2}) - \frac{G_{th}}{2}.$$

The general solution of Equation 2.4.18 is a linear combination of the so-called supermodes,

$$A(s,m) = \sum_n \beta_n e^{\gamma_n m/2} A_n(s). \tag{2.4.19}$$

Substituting Equation 2.4.19 into Equation 2.4.18 and using Equation 2.4.17, one reduces Equation 2.4.18 to:

$$\frac{d^2A_n(s)}{ds^2}-\frac{2}{\Sigma}\left(1+\frac{2\delta}{G_0\Sigma}\right)\frac{dA_n(s)}{ds}+\left(\frac{2}{G_0\Sigma^2}(G_0-G_{th}-\gamma_n)-\frac{s^2}{\Sigma^2\sigma_s^2}\right)A_n(s)=0\,. \quad (2.4.20)$$

The solution of the second order differential equation is [Litvinenko 1995d]

$$A_n(s)=H_n(s/\sqrt{\Sigma\sigma_s})\exp\left[-\frac{(s-s_0)^2}{2\Sigma\sigma_s}\right], \quad (2.4.21)$$

$$s_0=\sigma_s\left(1+\frac{2\delta}{G_0\Sigma}\right), \quad (2.4.22)$$

$$\gamma_n=(G_0-G_{th})-\frac{G_{th}}{2}\left(1+\frac{2\delta}{G_0\Sigma}\right)^2-\frac{\Sigma}{\sigma_s}(n+\frac{1}{2})G_0\,, \quad (2.4.23)$$

where $H_n(z)$ is a Hermite polynomial. For the lowest mode, i.e., n = 0, the longitudinal mode is a Gaussian

$$A_0(s,m)=\beta_0 e^{\gamma_0 m/2}\exp\left[-\frac{(s-s_0)^2}{2\Sigma\sigma_s}\right], \quad (2.4.24)$$

$$\gamma_0=(G_0-G_{th})-\frac{G_{th}}{2}\left(1+\frac{2\delta}{G_0\Sigma}\right)^2-\frac{G_0\Sigma}{2\sigma_s}. \quad (2.4.25)$$

The bunch length of the optical pulse can be as short as $\sqrt{\Sigma\sigma_s}$. If $\delta = 0$, the optical pulse has a maximum at $s = \sigma_s$. If $\delta=-\frac{G_0\Sigma}{2}$, the optical pulse has a maximum at $s = 0$. The ratio of maximum amplitude of these two detuning conditions is

$$\frac{A_0(\delta=0)}{A_0(\delta=-G_0\Sigma/2)}=e^{-G_0m/4}. \quad (2.4.26)$$

Therefore, the optical pulse has a maximum gain when the detuning condition is $\delta = -\frac{G_0\Sigma}{2}$, which is caused by the lethargic effect of the FEL. Saturation occurs at $G_0 = G_{th}/(1-\Sigma/2\sigma_s)$ when $\delta = -\frac{G_0\Sigma}{2}$. We observed the supermodes in the Duke/OK-4 SR FEL, by tuning the cavity length in steps of less than 0.2 μm (which corresponds to the revolution frequency in steps less than 5×10^{-3} Hz) at 200 nm with a 2% cavity loss.

2.5. Storage ring interactions

2.5.1. The motion of electrons in a storage ring

After passing the FEL interaction region of the optical klystron, the electrons travel through the rest of the ring, which consists of bending magnets, focusing or defocusing magnets, and an RF cavity. These electrons experience betatron and synchrotron oscillations. The restoring forces for the transverse betatron oscillations arise from the quadrupoles (focusing or defocusing magnets). For the longitudinal oscillations, the RF cavity together with certain lattice properties (compaction factor α_c: dependence of electron orbit on energy) determines the synchrotron oscillations. The revolution period of an electron around the ring depends on its energy and the lattice design. The momentum compaction factor α_c is defined as:

$$\alpha_c = \frac{\Delta C}{C_0} \Big/ \frac{\Delta p}{p_0}, \qquad (2.5.1)$$

where C_0 is the ring circumference and p_0 is the momentum of the synchronous electron. In a ring with positive momentum compaction, the electrons with high energy (or momentum) will travel in longer orbits than electrons with low energy. The RF cavity provides an energy kick to the electrons which compensates for the losses due to the synchrotron radiation caused by the bending magnets and wigglers. There are two RF phases with opposite slopes satisfying the condition for compensation of energy losses:

$$eV_{RF}\cos\varphi_s = \Delta E_{loss}\,. \tag{2.5.2}$$

The stable RF phase is determined by the following conditions: the electrons with low (high) energy (compared to the synchronous electrons) arrive earlier (later) at the cavity and therefore gain more (less) energy than the synchronous electrons. This effect is responsible for a stable synchrotron (energy) oscillation.

The equation of motion of an electron in a storage ring can be described using the Hamiltonian $\mathcal{H}$ [Wu 1995 and references therein] :

$$\frac{d\mathbf{X}}{dt} = \mathbf{S}\cdot\frac{\partial\mathcal{H}(\mathbf{X},t)}{\partial\mathbf{X}} - \left(\frac{d\mathbf{X}}{dt}\right)_{rad.damping}, \tag{2.5.3}$$

where

$$\mathbf{S} = \begin{bmatrix} \sigma & 0 & 0 \\ 0 & \sigma & 0 \\ 0 & 0 & \sigma \end{bmatrix} \text{ with } \sigma = \begin{bmatrix} 0 & -1 \\ 1 & 0 \end{bmatrix},$$

$$\mathbf{X}^T = \left[x, P_x, y, P_y, l/c, \varepsilon\right].$$

$\mathbf{X}$ is six dimensional vector of canonical conjugate variables. x (or y) and P_x (or P_y) are the transverse displacement and the canonical momentum respectively. $\varepsilon = E -$

E_0 is the deviation of energy from the synchronous electrons and l is the distance from the center of the electron beam (synchronous particle).

In the case of no coupling between x and y, the general solutions of the transverse motion are [Sands 1970]:

$$x(s) = Ae^{-s/\beta c\tau_x}\left(\sqrt{\beta_x(s)}\cos[\psi_x(s)+\varphi]+\eta_x(s)\frac{\varepsilon}{E_0}\right), \tag{2.5.4}$$

$$x'(s) \cong Ae^{-s/\beta c\tau_x}\left(\frac{\beta_x'(s)}{2\sqrt{\beta_x(s)}}\cos[\psi_x(s)+\varphi]-\frac{1}{\sqrt{\beta_x(s)}}\sin[\psi_x(s)+\varphi]+\eta_x'(s)\frac{\varepsilon}{E_0}\right),$$

$$y(s) = Ae^{-s/\beta c\tau_y}\sqrt{\beta_y(s)}\cos[\psi_y(s)+\varphi], \tag{2.5.5}$$

$$y'(s) \cong Ae^{-s/\beta c\tau_y}\left(\frac{\beta_y'(s)}{2\sqrt{\beta_y(s)}}\cos[\psi_y(s)+\varphi]-\frac{1}{\sqrt{\beta_y(s)}}\sin[\psi_y(s)+\varphi]\right),$$

$$(x'(s)=\frac{p_x}{p_s} \text{ and } y'(s)=\frac{p_y}{p_s}),$$

where

$$\psi_{x,y}(s)=\int\frac{ds}{\beta_{x,y}(s)},\ Q_{x,y}=\frac{1}{2\pi}\oint\frac{ds}{\beta_{x,y}(s)}=\frac{\mu_{x,y}}{2\pi},$$

$$\eta_x(s)=\frac{\sqrt{\beta_x(s)}}{2\sin(\mu_x/2)}\int_s^{s+C_0}\frac{\sqrt{\beta_x(\tau)}}{\rho(\tau)}\cos(\psi_x(\tau)-\psi_x(s)-\mu_x/2)d\tau. \tag{2.5.6}$$

Here, $\beta_{x,y}(s)$ are the beta functions, $\psi_{x,y}(s)$ are the phase advances, $\eta_x(s)$ is the eta function (dispersion function), $\rho(s)$ is the radius of curvature in bending magnets, $\tau_{x,y}$ are the radiation damping times of the betatron oscillations, $Q_{x,y}$ are the betatron tunes (the number of betatron oscillations per turn), and βc is the velocity of the

electron. In general, since the period T_β ($=\beta_{x,y}/c$) of the betatron oscillation is 5 - 10 times smaller than the revolution period T_0 (= C_0/c)and much smaller than the radiation damping time τ_β (In the Duke SR, T_0 is 358 nsec and τ_β is tens of msec), we can consider the damping term as a constant for betatron oscillations.

The typical solutions in the longitudinal motion are [Sands 1970]:

$$\varepsilon(t) = Ae^{-t/\tau_\varepsilon}\sin(\Omega_s t+\varphi_0), \tag{2.5.7}$$

$$l(t) = b\cdot Ae^{-t/\tau_\varepsilon}\cos(\Omega_s t+\varphi_0), \tag{2.5.8}$$

where

$$\Omega_s = f_0\sqrt{2\pi h\alpha_c\frac{eV_{RF}\cos\phi_s}{E_0}}, \tag{2.5.9}$$

$$b = \frac{\alpha_c C_0 f_0}{E_0\Omega_s}, \tag{2.5.10}$$

where Ω_s is the synchrotron frequency, h is the RF harmonic number f_{RF}/f_0, and ϕ_s is the synchronous phase. In general, the period T_s (= $1/2\pi\Omega_s$) of the synchrotron oscillation is much smaller than the radiation damping time τ_ε, but much larger than the revolution period T_0. Hence, the electrons in the longitudinal phase space experience damped oscillations.

The emission of synchrotron radiation provides damping in all six degrees of freedom of the electron motion. Damping of energy oscillations is simply caused by the energy dependence of the synchrotron radiation power (i.e., $P_{SR} \propto E^2B^2$). A particle with higher energy than the synchronous particle radiates more and a particle with low energy radiates less. The longitudinal deviation l is damped because l and ε

are canonical conjugates. Damping of transverse oscillations is caused by a loss in transverse momentum. The energy loss due to synchrotron radiation is compensated only in the longitudinal direction from the RF cavity, while the electrons lose their momentum in the direction of the particle motion at the moment of spontaneous emission. Therefore, the amplitude of transverse betatron oscillations is damped as well. Technically it is possible to design "separate-function lattices" to avoid or minimize coupling effects between the different pairs of conjugate coordinates. Then the coupling effects can be treated as perturbations. However, there is still direct coupling between synchrotron and horizontal betatron oscillations due to the non-zero dispersion function $\eta(s)$ (see Equations 2.5.4 and 2.5.5). However, the frequencies are so different from one another that the synchrotron oscillations can be ignored compared to the betatron oscillations. Similarly, we average over betatron oscillations when considering the synchrotron oscillations.

The damping coefficients can be calculated in a linear approximation [Sands 1970, Wiedemann 1993].

$$\alpha_i = J_i \frac{U_{SR}(E_0)}{2T_0 E_0} \equiv \frac{1}{\tau_i}, \quad (i = x, y, \varepsilon) \tag{2.5.11}$$

$$J_x = 1 - \mathscr{D}, \; J_y = 1, \text{ and } J_\varepsilon = 2 + \mathscr{D}, \tag{2.5.12}$$

where

$$\mathscr{D} = \frac{\oint \eta(s) \rho_0^{-1} (2K_1 + \rho_0^{-2}) ds}{\oint \rho_0^{-2} ds}.$$

J_i are the damping partition numbers and $\mathscr{D}$ (determined by the lattice design) is usually small. $U_{SR}(E_0)$ is the radiation energy loss per turn:

$$U_{SR}(E_0)[GeV] = 8.8575\times10^{-5}\cdot\frac{E_0{}^4[GeV]}{\rho_0[m]}, \tag{2.5.13}$$

for the synchronous electron with energy E_0. The energy loss per turn is much smaller than the electron's energy in our study. For example, in the Duke storage ring, the energy loss of the electron at 1 GeV is about 42 keV. For a lattice with a very small $\eta(s)$, the damping in betatron oscillations is almost two times slower than in synchrotron oscillations. The total damping decrement, $1/\tau_t$, (the sum of all damping decrements for the different modes of oscillation) is a constant known as "*Robinson's criterion*".

$$\frac{1}{\tau_t} = \frac{1}{\tau_x} + \frac{1}{\tau_y} + \frac{1}{\tau_\varepsilon} = 2\frac{P_{SR}}{E_0} \tag{2.5.14}$$

The total damping of the six-dimensional phase space volume depends only on the synchrotron radiation power and the electron energy. The lattice parameters such as $\eta(s)$ and $\rho(s)$ will not affect the total damping rate, but may shift the damping mechanism from one mode of oscillation to another. In typical lattices, this shift in damping mechanism occurs between the horizontal betatron oscillation and the synchrotron oscillation.

The previous equations 2.5.4, 2.5.5, 2.5.7, and 2.5.8 describe the time-averaged behavior of the electrons. Radiation is the emission of quanta of energy (photons) and thus differs from the classical (averaged) radiation process. Each time a photon is emitted, an electron experiences a small discontinuous jump in its energy.

The random emissions occur almost instantaneously (at the time scale of different types of oscillations). Since the energy jump due to the emission of a photon is a very small fraction of the electron's energy, we may consider the emission process as a stochastic process. This sudden energy change disturbs the reference trajectory and introduces random fluctuations (diffusion) in the betatron or synchrotron motions causing a quantum excitation. The quantum excitation depends on the fluctuations of the random photon emission, whereas the radiation damping depends on the average rate of emissions. In a steady state, a balance is reached between quantum excitation and radiation damping leading to a statistically stationary distribution of oscillation amplitudes and phases of the electrons in the bunch. The energy spread of the electron beam is primarily caused by changes in the electron energy due to quantum emission. The emission of a photon hardly changes the electron's position or direction, but does change the energy. In horizontal oscillations, the position and direction of an electron with respect to the reference trajectory changes mainly due to the non-zero dispersion functions, i.e., $\Delta x \approx -\eta(s)\varepsilon/E_0$ and $\Delta x' \approx -\eta'(s)\varepsilon/E_0$. In vertical oscillations, the contribution of the quantum excitation is small in a typical storage ring with plane symmetry, because the synchrotron radiation is emitted into a cone with a small angle $\pm \gamma^{-1}$. So $\Delta y' \approx -\theta \cos\varphi \varepsilon/E_0$, if a photon is emitted at an angle (θ, φ) with respect to the trajectory. The quantum excitation in vertical oscillation is much smaller than that in horizontal oscillation, while the radiation damping is of about the same order in both oscillations. Therefore, the vertical beam size is much smaller than the horizontal beam size in a storage ring which is

symmetric with respect to the horizontal plane. The distributions of the fluctuations are calculated using photon statistics (refer to [Wiedemann 1993] and the references therein).

We can determine the evolution of the electrons in phase space by using the Fokker-Planck equation. In a stationary state, the electron distribution in storage rings can be described as a Gaussian distribution. Electron distributions are discussed in detail in the next section.

2.5.2. Distribution of electrons in a storage ring FEL

The presence of an FEL modifies the evolution of the electron beam in a storage ring. The electron distribution function may be derived from the Fokker-Planck equation, if the process is stochastic [Renieri 1980, Litvinenko 1989]. The stochastic process is realized if the time interval Δt is sufficiently long for particles to encounter a large number of individual random kicks but still short enough for the fluctuations during period Δt to be small. In the six-dimensional phase space, the evolution of the electron beam distribution can be written as

$$\frac{\partial f}{\partial t}+\frac{\partial}{\partial X_\alpha}\left(\frac{dX_\alpha}{dt}\cdot f\right)-\frac{\partial}{\partial X_\alpha}\frac{\partial}{\partial X_\beta}\left[\frac{1}{2}\left\langle \delta X_\alpha \delta X_\beta \right\rangle \cdot f\right]=0, \qquad (2.5.15)$$

where $f \equiv f(\mathbf{X},t)$ is the distribution function and $\mathbf{X}^{\mathrm{T}}=[x,x',y,y',l,\varepsilon]$. In a stationary state with FEL-off, we can write the electron distribution function as a Gaussian:

$$f(\mathbf{X},t)=\frac{1}{\prod_{i=1}^{6}\sqrt{2\pi}\sigma_i}\exp\left[-\sum_{i=1}^{6}\frac{x_i^{\,2}}{2\sigma_i^{\,2}}\right]. \qquad (2.5.16)$$

When the FEL is on, electrons interact with the optical field in the FEL interaction region and exchange energy. As mentioned before, the FEL interaction causes bunching which leads to gain. If the beam modulation is on a scale of the wavelength λ and is unchanged for re-injection into the FEL interaction region, the gain remains high on each turn and the FEL has high power [Deacon 1980]. However, the concept of an isochronous storage ring has a large number of unresolved issues, especially, for short wavelength FELs.

The energy modulation, $\delta\varepsilon$, is a function of the phase difference, φ, between the optical field and the electron beam at the entrance time in the FEL interaction region. The phase difference, φ, for an electron displaced by Δs is $\varphi = \varphi_0 + 2\pi\Delta s/\lambda$, where φ_0 is the phase difference relative to the synchronous electron. In typical storage rings, the length of the electron orbit depends on the electron energy and the displacement of the electron after one turn, $\Delta s \equiv s_{n+1} - s_n = -\alpha_c C_0 \sigma_\varepsilon / E_0$. Since, in general, $\Delta s >> \lambda$, electrons lose their phase correlation after one turn. For example, Δs is ~ 100 μm in the Duke storage ring at a 500 MeV operating energy, while λ is ~ 200 nm. Therefore, the phase difference φ may be regarded as random at each entrance into the FEL interaction region. Furthermore, as the period, T_s, of the synchrotron oscillation is much longer than the revolution period, T_0, and much

shorter than the radiation damping time, τ_ε, $\delta\varepsilon$ may be regarded as an additional stochastic process that perturbs the synchrotron motion.

For the Duke/OK-4, $\eta(s)=0$ and $\eta'(s)=0$ in the interaction region. The quantum excitation effects on the betatron oscillation are negligible in FELs where the dispersion function is zero. Therefore, we can assume that changes in the transverse motion are negligible in the interaction region. Hence, we can now reduce the six-dimensional Fokker-Planck equation to a two-dimensional equation.

The equations of motion in longitudinal displacement ($l = z - z_0$) and energy deviation ($\varepsilon = E - E_0$) are:

$$\frac{dl}{dt} = -\alpha_c C_0 f_0 \frac{\varepsilon}{E_0}, \tag{2.5.17}$$

$$\frac{d\varepsilon}{dt} = f_0 \cdot \left(\Delta U_{RF}(s) - \Delta U_{rad}(\varepsilon) + u_{noise} + \Delta\varepsilon_{FEL}\right), \tag{2.5.18}$$

where

$$\Delta U_{RF}(s) \approx eV_{RF}\frac{2\pi h f_0 \cos\phi_s}{c} l,$$

$$\Delta U_{rad}(\varepsilon) \approx \left(\frac{dU_{rad}}{d\varepsilon}\right)_0 \cdot \varepsilon = \frac{2T_0}{\tau_\varepsilon}\varepsilon,$$

$$\langle \delta l \delta\varepsilon \rangle = 0 = \langle \delta l^2 \rangle,\ \langle \delta\varepsilon \rangle \cong \langle \Delta\varepsilon_{FEL} \rangle,\ \langle \delta\varepsilon^2 \rangle = \langle u_{noise}{}^2 \rangle + \langle \Delta\varepsilon_{FEL}{}^2 \rangle,$$

$$\langle u_{noise}{}^2 \rangle = \frac{55}{24\sqrt{3}} U_{SR}(E_0)\hbar\omega_c,\ \langle \Delta\varepsilon_{FEL} \rangle = \frac{1}{2}\frac{\partial}{\partial\varepsilon}\langle \Delta\varepsilon_{FEL}{}^2 \rangle,$$

$$\langle \Delta\varepsilon_{FEL} \rangle_{\varphi_0} = -\frac{1}{2}(\Delta E_0)^2 k \frac{ds}{dE}\sin k\left(\Delta s + \frac{ds}{dE}\varepsilon\right),$$

$$\left\langle \Delta\varepsilon_{FEL}{}^2 \right\rangle_{\varphi_0} = (\Delta E_0)^2 \left(1 + \cos k \left(\Delta s + \frac{ds}{dE} \varepsilon \right) \right),$$

where $\omega_c = 3c\gamma^3/2\rho$ is the critical frequency of synchrotron radiation from the electrons passing through the bending magnets. By defining the diffusion coefficients to be D_0 and D_{FEL} and using the synchrotron frequency Ω_s and the coefficient b in Equations 2.5.9 and 2.5.10, respectively, we can write the Fokker-Planck equation as:

$$\frac{\partial f}{\partial t} - b\Omega_s \varepsilon \frac{\partial f}{\partial l} + \frac{\Omega_s}{b} l \frac{\partial f}{\partial \varepsilon} - \frac{\partial}{\partial \varepsilon} \left[\frac{2}{\tau_\varepsilon} \varepsilon f + (D_0 + D_{FEL}) \frac{\partial f}{\partial \varepsilon} \right] = 0, \qquad (2.5.19)$$

where $D_0 = \frac{1}{2} f_0 \left\langle u_{noise}{}^2 \right\rangle$ and $D_{FEL} = \frac{1}{2} f_0 \left\langle \Delta\varepsilon_{FEL}{}^2 \right\rangle$, which correspond to the natural energy spread and the induced energy spread of the electrons. This second order partial differential equation can be simplified by changing variables to action, I, and the angle, φ_s, by defining

$$I = \frac{\varepsilon^2}{2} + \frac{l^2}{2b^2} \text{ and } \varphi_s = \Omega_s t + \varphi_0 . \qquad (2.5.20)$$

Then, $\varepsilon = \sqrt{2I} \cos\varphi_s$ and $l = b\sqrt{2I} \sin\varphi_s$. Since the distribution is in stationary state when quantum excitations are balanced by radiation damping, we average over one period ($T_s << \tau_\varepsilon$) of synchrotron oscillation. Dropping the $\frac{\partial f}{\partial \varphi_s}$ terms (i.e., $f \equiv f(\varepsilon, l, t) \equiv f(I, t)$), the Fokker-Planck equation of Equation 2.5.17 is reduced to:

$$\frac{\partial f}{\partial t} - \frac{\partial}{\partial I} \left(\frac{2}{\tau_\varepsilon} I f \right) - \frac{\partial}{\partial I} \left[I (D_0 + \tilde{D}_{FEL}) \frac{\partial f}{\partial I} \right] = 0, \qquad (2.5.21)$$

$$\tilde{D}_{FEL} \equiv \tilde{D}_{FEL}(I,t) = \frac{1}{\pi}\int_0^{2\pi} D_{FEL}(I,\varphi_s,t)\cos^2\varphi_s \, d\varphi_s \,. \qquad (2.5.22)$$

By solving this equation, we can observe how electrons in a storage ring evolve under the influence of interactions with the FEL. This equation can be solved analytically in a limited number of cases. In the stationary state, the distribution is a simple Gaussian if the diffusion coefficient is constant (i.e., does not depend on *I*). However, since the diffusion coefficient depends on I ($\tilde{D}_{FEL} \equiv \tilde{D}_{FEL}(I,t)$), the distribution is not Gaussian. Assuming that the electron beam and the optical bunch are well synchronized, one can analytically derive the form of the electron distribution in a steady state. The solution of Equation 2.5.19 becomes

$$f(I) = A\exp\left[-\int_0^I \frac{2}{\tau_\varepsilon(D_0 + \tilde{D}_{FEL}(I'))}dI'\right], \qquad (2.5.23)$$

$$A = \left[2\pi b\int_0^\infty dI \exp\left[-\int_0^I \frac{2}{\tau_\varepsilon(D_0 + \tilde{D}_{FEL}(I'))}dI'\right]\right]^{-1},$$

where A is a normalization factor. In order to study effects of the FEL interaction on the electron beam distribution, we first derived the analytical form of $\tilde{D}_{FEL}(I)$ (diffusion coefficient averaged over one period of synchrotron oscillation) for a plane wave in the FEL and proved that the electron distribution is not a Gaussian form but a bell-like shape with flattened.

For a plane wave in the FEL,

$$\left\langle \Delta\varepsilon_{FEL}{}^2 \right\rangle_{\varphi_0} = \left(\frac{1}{2}e\mathscr{E}_0 L_w[JJ]\frac{K_w}{\gamma}\right)^2\left(1+\cos k\Delta s_0\left(1-\frac{2\varepsilon}{E_0}\right)\right)\exp\left[-\frac{l^2}{\sigma_l^2}\right], \qquad (2.5.24)$$

and D_{FEL} for an optical klystron is expressed by

$$D_{FEL}(\varepsilon,s)=\frac{1}{2}f_0\left\langle\Delta\varepsilon_{FEL}{}^2\right\rangle_{\varphi_0}$$

$$=\frac{1}{2}f_0\left(\frac{1}{2}e\,\mathscr{E}_0 L_w[JJ]\frac{K_w}{\gamma}\right)^2\left(1+\cos k\Delta s_0\left(1-\frac{2\varepsilon}{E_0}\right)\right)\exp\left[-\frac{l^2}{\sigma_l^2}\right],$$

(2.5.25)

where $[JJ]=\left[J_0(\xi)-J_1(\xi)\right]$, with $\xi=\frac{K_w^2/4}{1+K_w^2/2}$. $\mathscr{E}_0$ is the peak value of the amplitude of the optical field, Δs_0 is the slippage of the synchronous electron, σ_l is the rms bunch length of the optical beam, and $J_n(z)$ is a Bessel function. To arrive at the maximum gain condition, the diffusion coefficient in the (l, ε) phase space is shown in Figure 2.5.1.

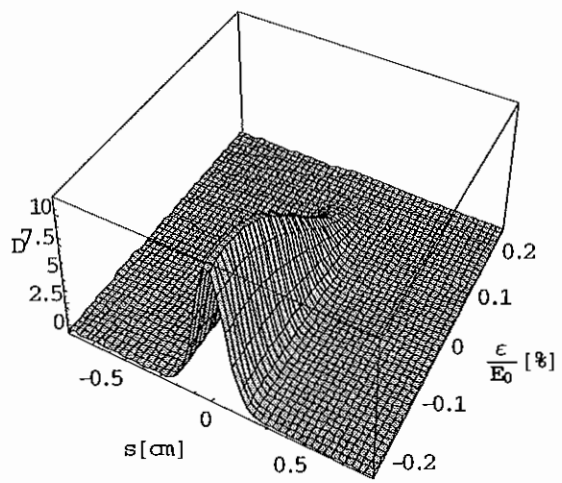

Fig. 2.5.1. Diffusion coefficient in (s, ε) phase space. Diffusion coefficient in (s, ε) for the electron beam interacting with the optical field with a peak amplitude $\mathscr{E}_0$ and a bunch length σ_l.

The average of the diffusion coefficient over one period of synchrotron oscillation is [see Appendix D]

$$\tilde{D}_{FEL}(I) \approx \frac{1}{2} f_0 \left(\frac{1}{2} e \mathscr{E}_0 L_w [JJ] \frac{K_w}{\gamma} \right)^2 \left(I_0(qI) + I_1(qI) \right) \cdot e^{-qI}, \qquad (2.5.26)$$

where $q = \frac{b^2}{\sigma_I^2}$ and $I_n(z)$ is a modified Bessel function satisfying the relationship $I_n(z) = i^{-n} J_n(iz)$. The averaged diffusion coefficient depends on the action I and on the optical bunch length σ_l for the given ring parameters. Substituting $\tilde{D}_{FEL}(I)$ into $f(I)$ for Equation 2.5.23, we arrive at the electron distribution in phase space. The distribution of electrons is a bell-like shape with flatter top than Gaussian (see Figures 2.5.2 and 2.5.3).

Figures 2.5.2 and 2.5.3 show theoretical graphs related to the diffusion induced by the FEL interaction with different parameters of the FEL optical pulses. As we expected, it is noticeable from Figure 2.5.2 that increasing the length of the FEL optical pulse by a factor of 1.5, while keeping its peak power constant, causes larger diffusion and energy spread. The same increase of the length of the FEL optical pulse, while keeping its energy constant, causes less diffusion and less energy spread growth (see Figure 2.5.3).

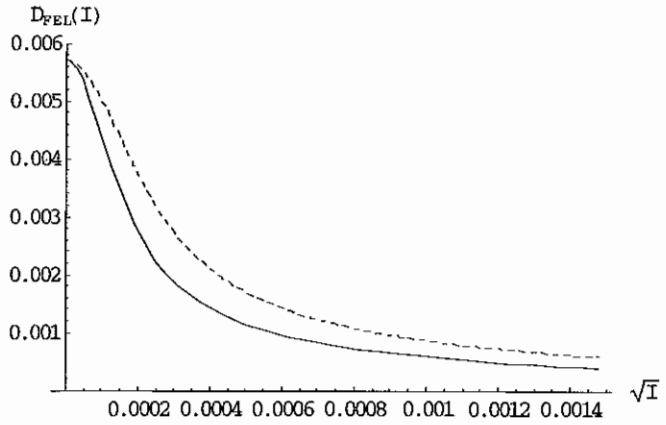

(a) Averaged diffusion coefficient

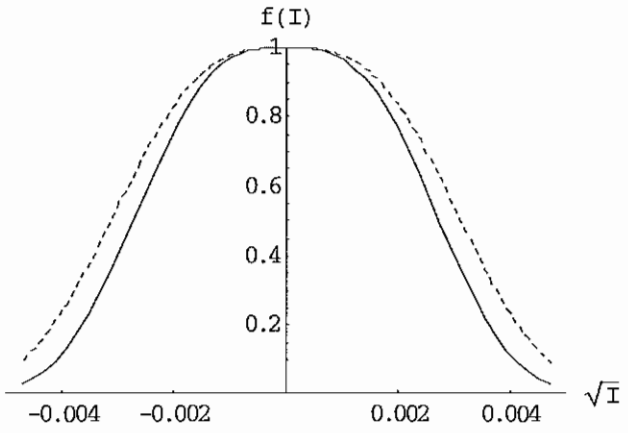

(b) Distribution of electron beam

Fig. 2.5.2. The averaged diffusion coefficients and the electron beam distribution as a function of $\sqrt{I}$ with a constant peak FEL power. The solid curve (a) is for the optical bunch length $\sigma_{l,a}$ = 1.92 mm and the dashed curve (b) is for the optical bunch length $\sigma_{l,b}$ = 1.28 mm. (i.e., $\sigma_{l,a} = 1.5\sigma_{l,b}$)

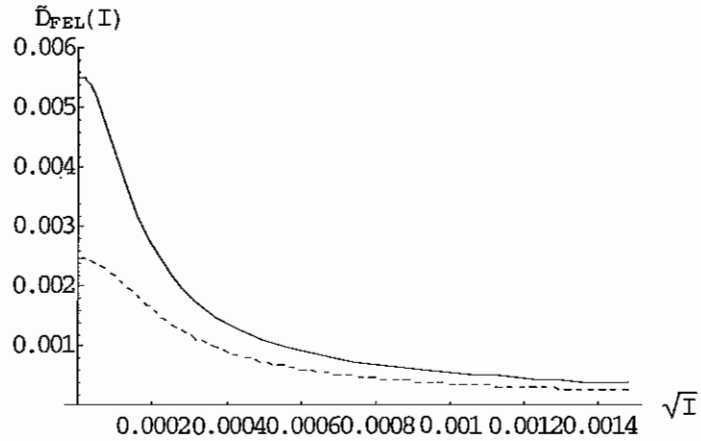

(a) Averaged diffusion coefficient

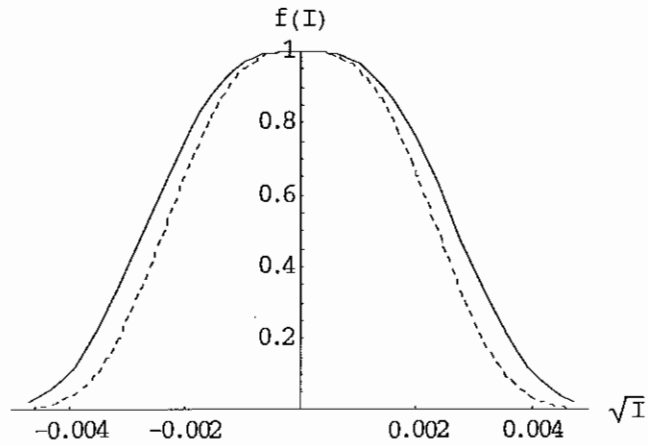

(b) Distribution of electron beam

Fig. 2.5.3. The averaged diffusion coefficients and the electron beam distribution as a function of $\sqrt{I}$ with a constant average FEL power. The solid curve (c) is for the optical bunch length $\sigma_{l,c} = 1.92$ mm and the dashed curve (d) is for the optical bunch length $\sigma_{l,d} = 1.28$ mm. (i.e., $\sigma_{l,c} = 1.5\sigma_{l,d}$)

For the simple case of a long optical pulse, the diffusion coefficient depends weakly on the action I so the electron distribution is assumed to be a Gaussian. By averaging over the electron distribution, we can get a simple form for the average power [Litvinenko 1989, Dattoli 1980]

$$P_{ave} = -J_e P_{SR} \frac{\sigma_E^2 - \sigma_{E_0}^2}{E_0} k \left|\frac{ds}{dE}\right| \frac{M \sin k\Delta s}{1 + M \cos k\Delta s}, \tag{2.5.27}$$

where M is the modulation rate,

$$M = \exp\left[-\frac{1}{2}\left(k \frac{ds}{dE} \sigma_E\right)^2\right], \tag{2.5.28}$$

$ds/dE = -2\,\Delta s/E_0$, and Δs is total slippage. For a maximum gain, i.e., $\sin k\Delta s = -1$,

$$P_{ave} = J_e P_{SR} \frac{\sigma_E^2 - \sigma_{E_0}^2}{\sigma_k E_0} e^{-\frac{1}{2}\left(\sigma_E / \sigma_k\right)^2}, \tag{2.5.29}$$

where $\sigma_k = 1 \Big/ k\left|\frac{ds}{dE}\right|$. The maximum power arises when $\sigma_k = \sigma_E$. Hence, Renieri's limit is

$$P_{ave,\max} = J_\varepsilon P_{SR} \frac{\sigma_{E,\max}^2 - \sigma_{E_0}^2}{\sigma_{E,\max} E_0} e^{-1/2} = J_\varepsilon P_{SR} \frac{\sigma_{\varepsilon,\max}^2 - \sigma_{\varepsilon_0}^2}{\sigma_{\varepsilon,\max}} e^{-1/2}, \tag{2.5.30}$$

where σ_ε is the induced relative energy spread. For $\sigma_{\varepsilon,\max} >> \sigma_{\varepsilon_0}$,

$$P_{ave,\max} \approx J_e P_{SR} \sigma_{\varepsilon,\max} \cdot e^{-1/2}, \tag{2.5.31}$$

which shows that the saturated FEL power depends on the synchrotron radiation power of the bending magnet and the induced energy spread due to FEL interactions. Since P_{SR} depends on N_e and E_0^4, the saturated power increases as the electron

energy, γ^4, and the beam current, I_e^{α}. We will show in following sections that the total flux of the γ rays generated via intra-cavity Compton backscattering, also, increases with the electron energy γ^4 and the beam current $I_e^{\alpha+1}$. The factor α includes the contribution of the beam current to the induced energy spread.

Chapter 3

Storage Ring FEL: Experiment

3.1. Introduction

The first lasing of a storage ring FEL occurred on the ACO at Orsay, France in 1983 using an optical klystron [Elleaume 1984]. This success occurred at a wavelength of 650 nm. The laser was tuned to 463 nm in 1985 [Billardon 1986]. Then in 1988 lasing in the visible (580 nm – 690 nm) and the UV range (240nm – 270 nm and 460 – 370 nm) was achieved on the VEPP-3/OK-4 FEL in Novosibrisk, Russia [Kulipanov 1990]. Successful lasing at 240 nm promised the possibility of developing SR FELs for short wavelength applications.

SR FELs were proposed for many facilities throughout the world in the late 1980s and 1990s: Super-ACO (Orsay, France), Delta (Dortmund, Germany), NIJI-IV (Tsukuba, Japan), UVSOR (Okazaki, Japan), new SUBARU (Harima, Japan), and Duke/OK-4 (Duke University, USA). The performances of SR FELs have been consistently improved since 1985. VEPP-3 demonstrated a narrowing of lasing linewidth [Litvinenko 1991a, 1991b], Super-ACO increased the average power of the FEL and the stability of the laser [Roux 1998], and UVSOR operated in different polarization modes [Hama 1995]. In August 1999, the OK-4/Duke SR FEL lased at a wavelength of 193.7 nm, breaking the 200 nm barrier [Litvinenko 1999b]. At Duke

University, a better understanding of the storage ring FEL has led to improvements in FEL stability and operating conditions. In addition the UV FEL light was provided to external researchers for their applications. New developments and modifications are underway that will result in higher power operation and shorter wavelengths.

The Duke storage ring is dedicated to operate FELs; the ring consists of a racetrack configuration with two 35 m dispersion-free straight sections for the insertion devices. The lattice was designed to minimize the emittance and maximize admittance. Since the first lasing at wavelengths between 345 nm and 412 nm in 1996 [Litvinenko 1997, 1998], the spectral tunability has been expanded upward to 730 nm and downward to 193.7 nm. The main problem when lasing at short wavelengths is mirror degradation caused by the high harmonic radiation from the optical klystron. However, successful lasing at 212 nm in NIJI-IV (ETL, Japan) [Yamada 1999] was achieved using Al_2O_3/SiO_2 multilayer dielectric mirrors. Mirror degradation studies of Al_2O_3/MgF_2 multilayer dielectric mirrors at 220 nm in the Duke/OK-4 demonstrated that the MgF_2 material has less resistance to high harmonic radiation, although its reflectance below 200 nm is rather large. The main factors contributing to lasing below 200 nm are changes of operating conditions of the storage ring and optical properties of the cavity mirrors. The changes of betatron tunes below the quarter resonance reduced the transverse instabilities and made it possible both to store high current beam and to achieve higher gain. The combinations of Al_2O_3/SiO_2 and Al_2O_3/MgF_2 multilayer coatings for the cavity

mirrors increased the resistance to high harmonic radiation. The average laser power is only a few mW at around 3 mA electron beam current.

3.2. The Duke/OK-4 Storage Ring

The layout of the Duke storage ring is shown in Figure 3.2.1. The main parameters of the Duke storage ring are listed in Table 3.2.1.

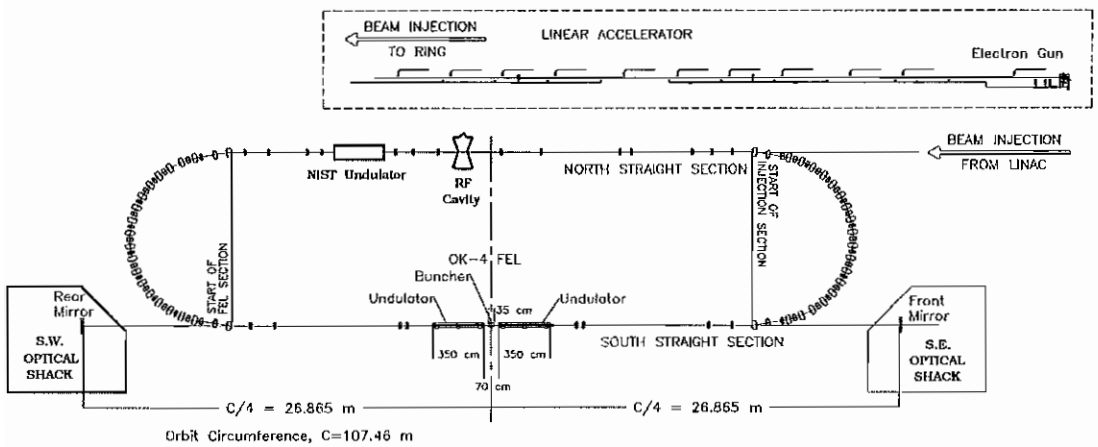

Fig. 3.2.1. Layout of the Duke storage ring.

Table 3.2.1. Parameters of the Duke Storage Ring.

Parameters	Designed	Measured
Operating energy, E_e, [GeV]	0.25 – 1.0	0.23 – 1.1
Ring circumference, C_0, [m]	107.46	107.46±0.003
Revolution frequency, f_0, [MHz]	2.7898	
RF frequency, f_{RF}, [MHz]	178.547	
Betatron tunes, Q_x and Q_y	9.11, 4.18	9.118, 4.145
Momentum compaction factor, α_c	0.0086	
Natural chromaticities, C_x and C_y	-10.0, -9.78	
Compensated values, C_x and C_y	+0.1, +0.1	+0.1, +0.1
Dynamic aperture, A_x and A_y, [mm mrad]	56.0, 16.0	> 54, > 15.0
Energy acceptance, $\Delta E/E$, of the ring	> ± 5.0 %	± 6 %
Limited by existing RF cavity at 1 GeV	± 2.8 %	± 2.6 %
Maximum β-functions, β_x and β_y, [m]	13.6, 21.3	12.92, 21.81
η-function in the straight section [m]	0	< 0.005
Multi-bunch beam current [mA]	100	155
Single bunch beam current [mA]	40	17[a]
Peak current [A]	80 – 130	33[a]
Emittance at 1 GeV, ε_x and ε_y, [nm rad]	18, < 1.8	18 ± 1, < 1
Relative energy spread (1 GeV, low current)	0.0005	0.0005
Relative energy spread (5mA/bunch, 0.5 GeV)		0.0011
Bunch length (low current, 0.5 GeV) [psec]	16	17
Bunch length (5mA/bunch, 0.5 GeV) [psec]		60
Impedance of the ring, Z_n/n, [Ω]		2 – 3.5[c]
Beam size in the OK-4, σ_x and σ_y, [mm]	0.27, 0.085	
Lifetime [hour]	> 4	2 – 6[b]

[a] *: 0.5 GeV with 500 kV RF voltage*
[b] *: depends on operating energy*
[c] *: depends on the beam lines*

3.2.1 Beam diagnostics system

Recent developments towards improving the understanding of operation of the FEL include an electron beam orbit measurement system, a gain modulator for the high peak FEL power, and a beam diagnostics system that uses a streak camera. Upgrades have been made to the temperature measurement system, tune measurement system, and photo injection system which consists of a high peak power, low time jitter nitrogen laser.

The orbit measurement system consists of 34 Bergoz BPM (Beam Position Monitor) units and is used to measure the electron beam orbits. Although the calibration is not complete, the repeatability allows one to monitor and reproduce the electron orbits for lasing. In γ-ray generation mode, the orbit measurement system is especially useful as the flux of γ rays passing through the collimator may be optimized by adjusting the electron beam angles.

The gain modulator consists of a fast steering magnet with a ferrite yoke and control electronics [Pinayev 1999]. This system has been in operation for over six months generating a high peak power of approximately 0.3 MW.

The betatron tune measurement system has been upgraded with an HP network analyzer. Two long strip lines were installed to pick up small signals. These improvements allow us to measure the tune, to shift the tune away from resonance, and to suppress transverse instabilities. A transverse feedback system is under development.

The UV nitrogen laser used for the photo injection has 800 kW peak power, less than 500 psec pulse duration, and less than 1 nsec time jitter. Average electron beam currents can be stored at a rate of about 0.5 mA per shot and up to ~ 20 mA per bunch. Although we can store approximately 20 mA of electron beam in a single bunch, typically one half of the current is lost during the ramping from injection energy to operating energy. This loss is mostly due to instabilities caused by the higher order modes of the RF cavity. The number of electron bunches in the ring can be controlled by adjusting the injection timing of the electron beam. For γ-ray generation, two bunches separated by half of the circumference or four bunches separated by a quarter of the circumference are stored in the ring. Electrons can be stored in any of the sixty-four possible bunches of the Duke storage ring. However, as the number of bunches increases, the operation becomes more sensitive to instabilities in the RF cavity.

A Hamamatsu streak camera has been installed downstream of the optical cavity to measure the bunch length of the optical beam and the electron beam. By using a MgF_2 window for the photo cathode and focusing mirror input optics, the bunch lengths can be measured down to 140 nm. Optimization of lasing conditions is accomplished by monitoring the macro-temporal structure and power of the optical beams. The dual sweep mode of the streak camera is used to measure both the micro-temporal (vertical axis) pulses and macro-temporal (horizontal axis) structure (evolution of the FEL). In addition, a Si photo diode is also used to monitor the macro-temporal structure on a LeCroy digital oscilloscope. By adjusting the

revolution frequency in 0.1 to 0.01 Hz steps, one may observe the macro-temporal behavior of natural lasing in the FEL. The four ranges (Range 1 to Range 4) of fast sweep time with better than 2 psec resolution (1.5 psec FWHM resolution at Range 1, which has 150 psec full time scale) and the variable horizontal sweep time (from 100 nsec to 100 msec) make it possible to study instabilities of the electron beam caused by microwave instability and noise. It is observed that jitter in the electron beam at low frequency is mostly due to noise from the power supplies and at the synchrotron frequency is due to the high order modes of the RF cavity (shown in Figure 3.2.2). The amplitude of the oscillation can be reduced (but not totally eliminated) by adjusting the RF voltage and higher order modes using two tuners in

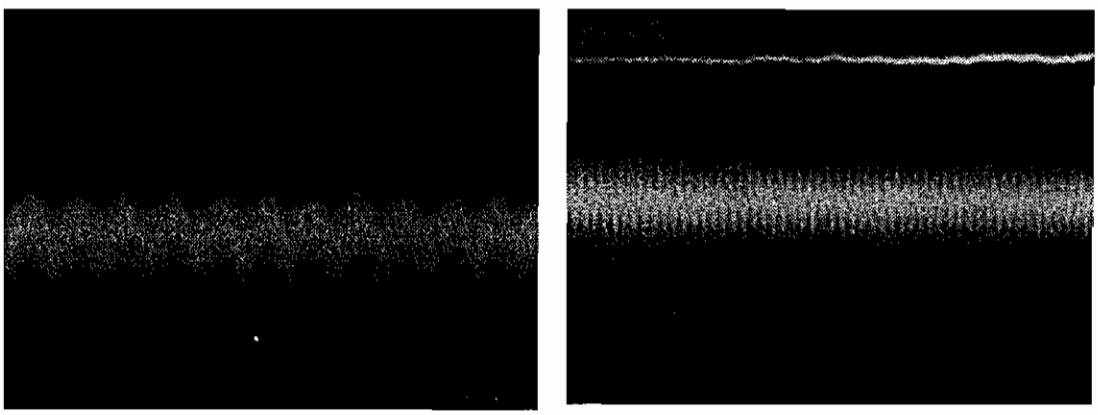

(a) (b)

Fig. 3.2.2. Electron beam oscillation due to high order modes of the RF cavity and its influence on the FEL. (a) is measured at 600 MeV ring energy and 550 kV RF voltage. Amplitude of longitudinal oscillation (vertical axis) is ~ 7.5 mm (i.e., ~ 25 psec). (b) is measured at 460 MeV ring energy and 500 kV. Upper line is the FEL light and lower line is the electron beam (spontaneous radiation from the OK-4). The FEL jitter on the several psec time scale is due to oscillation of the electron beam.

the RF cavity. Improvements to the feedback system are underway which will reduce the undesirable fluctuations at the synchrotron frequency. Replacement of magnet coils and power supplies are scheduled for early 2000 and should help stabilize the electron beam orbit..

3.2.2. Measurements of electron beam parameters

We measured the beta functions in the interaction region (the south straight section) for beam size and angular spread measurements and in the northwest corner for emittance measurements. By measuring the betatron tune shift, $\Delta Q_{x,y}$, while changing the quadrupole strength, ΔK_1, one can calculate the beta functions at each magnet (dipole or quadrupole magnets) as followings (refer to [Wu 1995] and the references therein):

$$\Delta Q_{x,y} = \frac{1}{4\pi}\int_{quad}(\Delta K_1)_{x,y}\beta_{x,y}ds \cong \frac{1}{4\pi}(\Delta K_1)_{x,y}(\beta_{ave})_{x,y}l_{quad} \qquad (3.2.1)$$

$$(\beta_{ave})_{x,y} = \frac{4\pi\Delta Q_{x,y}}{(\Delta K_1)_{x,y}l_{quad}}. \qquad (3.2.2)$$

At a 460 MeV operating energy, the horizontal beta function in the FEL interaction region is ~ 3.84 m (close to the design value of 4 m). This result is reasonable as one expects a smaller value for the horizontal beta function than the designed one because the Rayleigh range of the optical resonator is ~ 3.4 m. This Rayleigh range is smaller than the design value of 4 m. Both the electron beam and the optical beam should be matched to optimize FEL gain and power. For high operating energies around 600 MeV measurements become quite sensitive to drifts of the magnet power

supplies. These cause drift in the betatron tunes. Measurements in the northwest corner have a similar problem. Table 3.2.2 and Table 3.2.3 summarize the results of the measurements.

Ring energy (MeV)	β_x at S2F (entrance)	β_x at S4F (exit)	β_x in the OK-4	Focal point (from the center of OK-4)
460	11.517 m	9.745 m	3.838 m	22.6 cm
600	10.576 m	10.641 m	4.643 m	-1.72 cm

Table 3.2.2 The beta functions in the FEL interaction region.
S2F and S4F are quadrupole magnets adjacent to the OK-4 FEL.

Ring energy	β_x at N8F	β_x at W01F	β_x at the bending magnet
460 MeV	5.906 m	2.803 m	1.0252 m
600 MeV	8.696 m	2.717 m	0.693 m

Table 3.2.3 The beta functions at the bending magnet in the northwest corner
N8F and W01F are quadrupole magnets adjacent to the bending magnet.

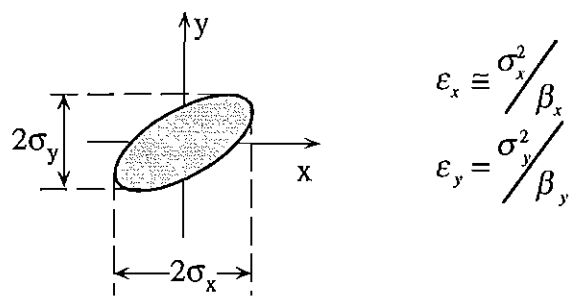

Fig. 3.2.3 Schematics of emittance measurements

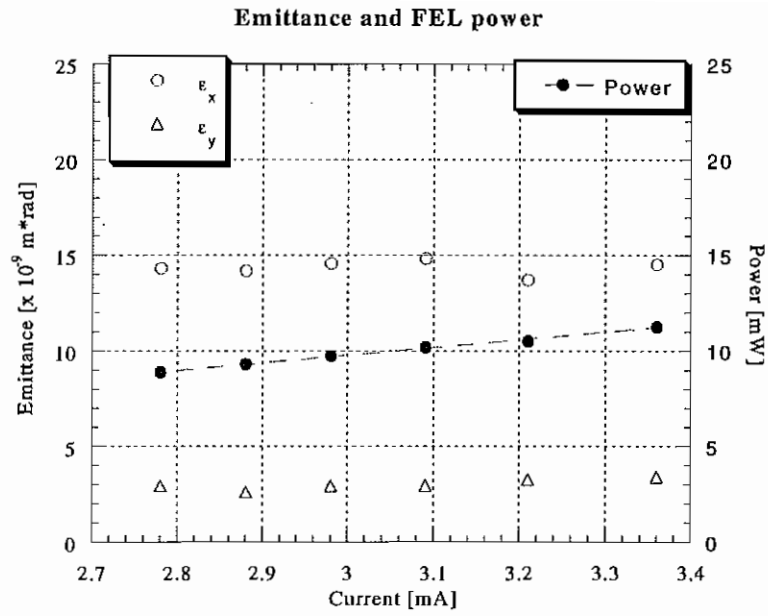

Fig. 3.2.4 Dependence of emittance on electron beam current at 600 MeV in the FEL mode.

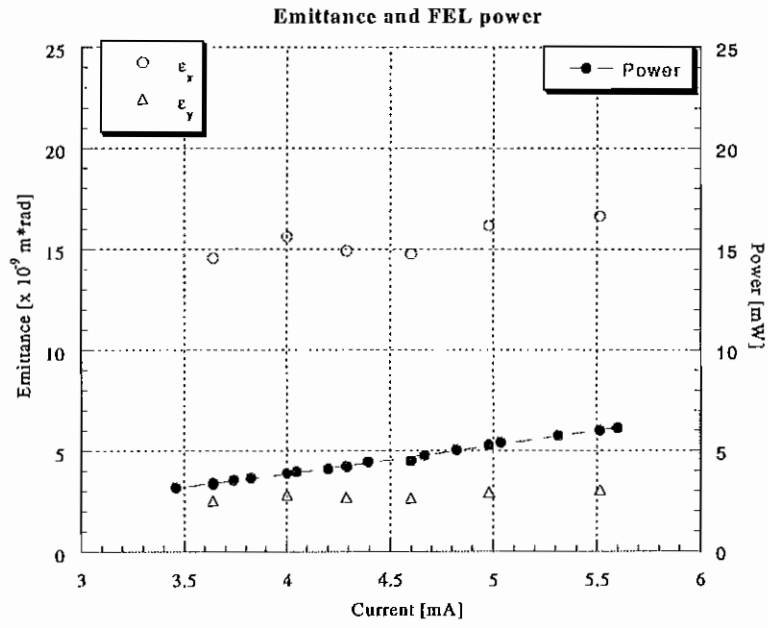

Fig. 3.2.5 Dependence of emittance on electron beam current at 460 MeV in the γ-ray mode.

Emittance can be measured indirectly by measuring the beta function and the beam size as shown in Figure 3.2.3. To avoid the diffraction limit, it is desirable to select shorter wavelengths or high operating energy. We used 1:1 lens optics and a red filter to reduce dispersion effects. The emittance during FEL and γ-ray operation was approximately constant with electron beam current. Figure 3.2.4 and Figure 3.2.5 show the dependence of emittance on the electron beam current at a 600 MeV

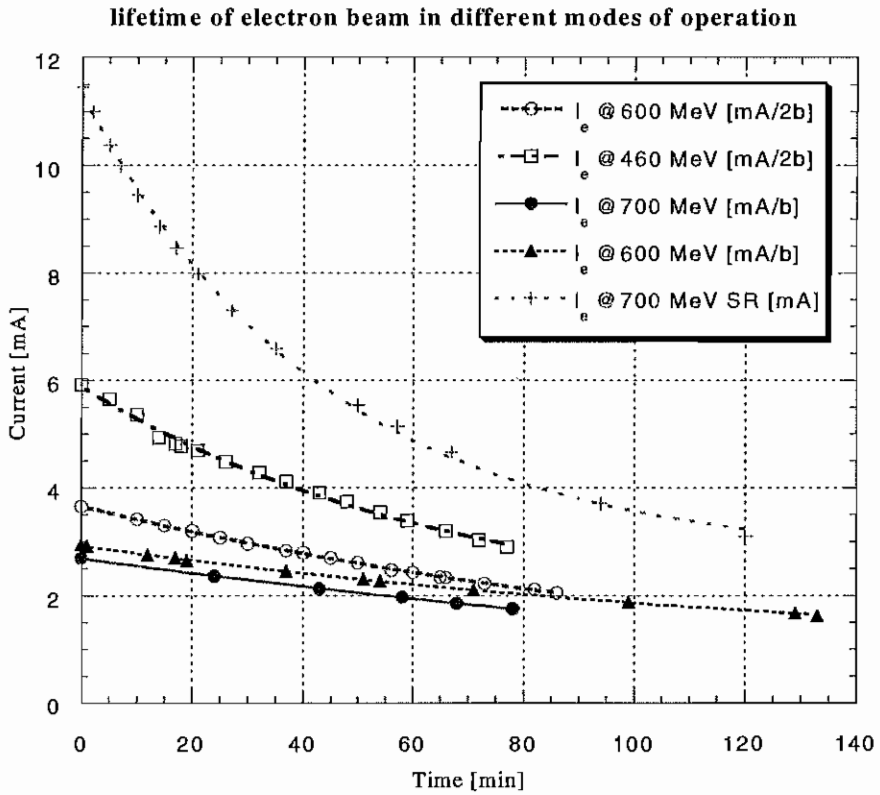

Fig. 3.2.6 Lifetime of electron beam in different modes of operation.
(○: γ-ray mode at 600 MeV, $\tau = 130$ min; □: γ-ray mode at 460 MeV, $\tau = 65.2$ min;
●: FEL mode at 700 MeV, $\tau = 214.7$ min; ▲: FEL mode at 600 MeV, $\tau = 147.9$ min;
+: Spontaneous radiation mode at 700 MeV, $\tau = 43.9$ min)

ring energy in FEL mode and at a 460 MeV ring energy in γ-ray mode. The transverse beam size during lasing or not lasing is approximately the same which indicates that the transverse size of the electron beam is not dominated by the FEL interactions.

The electron beam lifetimes are different for the different operating modes (see Figure 3.2.6). In the no-lasing mode, the beam lifetime is determined by the Touschek effects. In the lasing mode, the beam lifetime is longer due to bunch lengthening effects. In the γ-ray mode (as compared to the FEL mode), the lifetime is reduced by collisions between electrons and photons.

3.3 Spontaneous radiation from the OK-4

The resonant wavelength of spontaneous radiation from the OK-4 depends upon the wiggler period λ_w, the wiggler parameter K_w, and the electron beam energy γ (= E_e/m_ec^2). This dependence is given by

$$\lambda_{2n+1} = \lambda_0/(2n+1) \qquad \text{with} \quad \lambda_0 = \frac{\lambda_w}{2\gamma^2}\left(1+\frac{K_w^2}{2}+\gamma^2\theta^2\right), \tag{3.3.1}$$

where λ_0 is the fundamental wavelength and λ_{2n+1} are odd harmonics from the planar wiggler. The tunability of the spectral range of the fundamental wavelength λ_0 in the OK-4 FEL is illustrated in Figure 3.3.1. The relevant parameters of the OK-4 magnetic system are listed in Table 3.3.1. We measured the spectrum of the high harmonics to demonstrate the tunability of the OK-4. The tunable range of the OK-4

at 1 GeV is from 18 nm to 140 nm (limited by maximum tunable range of wiggler currents) for the fundamental wavelength.

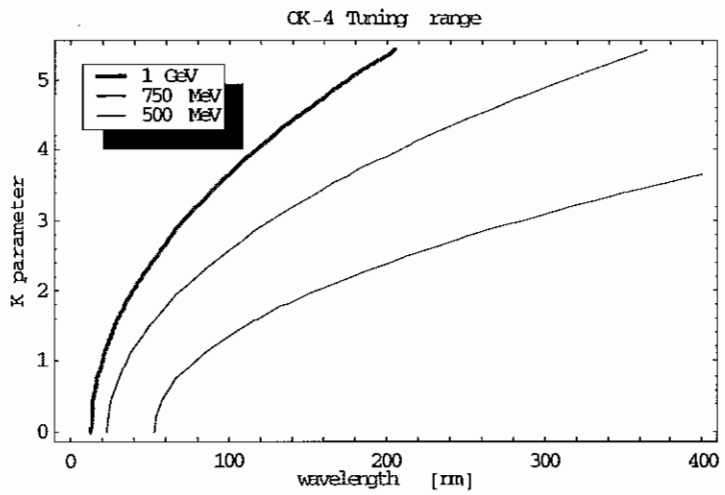

Fig. 3.3.1. Tunability of the fundamental wavelength of the OK-4 FEL.

	Parameters	Designed
	Total length [m]	7.8
Wiggler	Length, L_w, [m]	3.4
	Period, λ_w [cm]	10
	Magnetic field [kGs]	0 – 5.8
	Wiggler parameter, K_w	0 – 5.42
	Tuning range ($\lambda_{max}/\lambda_{min}$)	15.67
Buncher	Length [m]	0.34
	Magnetic field [kGs]	0 – 12.0

Table 3.3.1 Parameters of the OK-4 magnetic system.

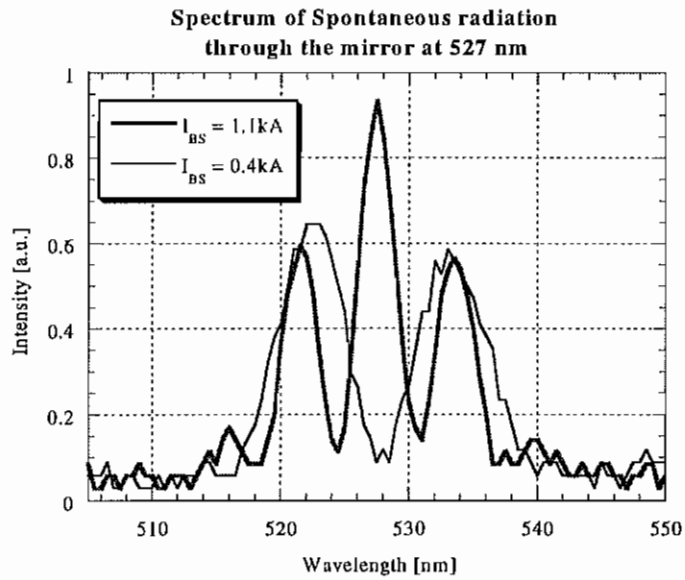

Fig. 3.3.2. Spectra of the spontaneous radiation from the OK-4 with two different buncher currents.

The spontaneous radiation of the optical klystron plays a key role in understanding the electron beam characteristics and in aligning the electron beam in the optical cavity. The direction of the electron beam in the optical klystron can be changed by adjusting the trims of the quadrupole magnets located at both ends of the optical klystron. As the buncher current is increased, the number of fringes in fine structure of the spontaneous radiation is also increased (see Section 2.2). Figure 3.3.2 shows the fine structure for two different buncher currents. The number N_d of periods of light of wavelength λ passing over an electron in the bunching section is obtained by measuring the separation of the adjacent peaks in the fine structure of the spectrum.

$$N_d \cong \frac{1}{2}\frac{\lambda_1+\lambda_2}{\lambda_1-\lambda_2} - N_w, \tag{3.3.2}$$

where λ_1 and λ_2 are the wavelengths of the adjacent peaks and N_w is the number of wiggler period. The simultaneous lasing at two wavelengths can be achieved by optimizing equally the gains at the two wavelengths separated by $\Delta\lambda \approx \lambda_0/(N_w + N_d)$, as shown in Figure 3.3.2. Since electrons with different energy, angle, and transverse position produce a spontaneous radiation spectrum shifted in wavelength from λ_0, the measured spectrum always has an incomplete modulation, as was mentioned in Section 2.2. The modulation depth f is defined as:

$$f = \frac{I_{\max} - I_{\min}}{I_{\max} + I_{\min}}. \tag{3.3.3}$$

The modulation depth is determined mostly by the energy spread of the electron beam. By attempting to fit the spontaneous radiation spectrum to a known distribution, we can estimate the resonant wavelength, the total slippage, and the energy spread. The natural energy spread (due only to synchrotron radiation damping and quantum excitation) can be measured at low current to avoid anomalous bunch lengthening effects. The modulation due to the electron beam energy spread and angular spread are (assuming the energy distribution of the electrons is Gaussian),

$$f_e = \exp\left[-\frac{1}{2}\left(4\pi(N_w + N_d)\frac{\sigma_\varepsilon}{E_0}\right)^2\right], \tag{3.3.4}$$

$$f_{x'} = \left[1 + \left(k(L_w + L_d)\sigma_{x'}^2\right)^2\right]^{-1/4} \quad (x' \text{ or } y').$$

If the angular spread is neglected, then the energy spread of the electron beam is given by

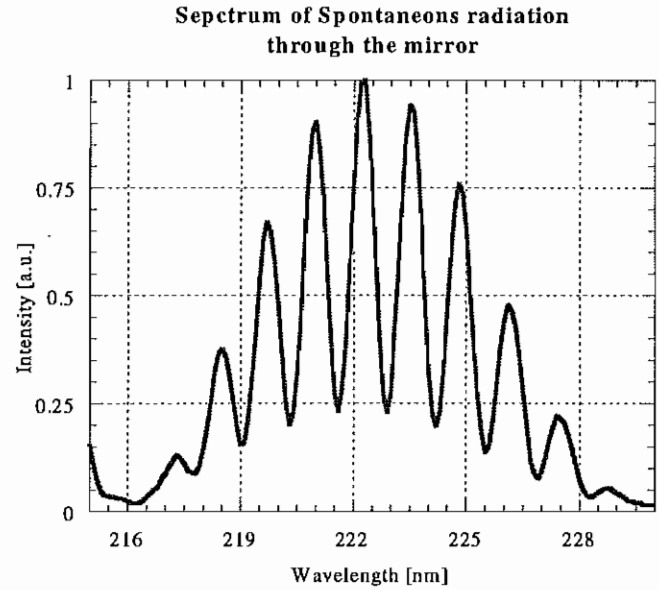

(a)

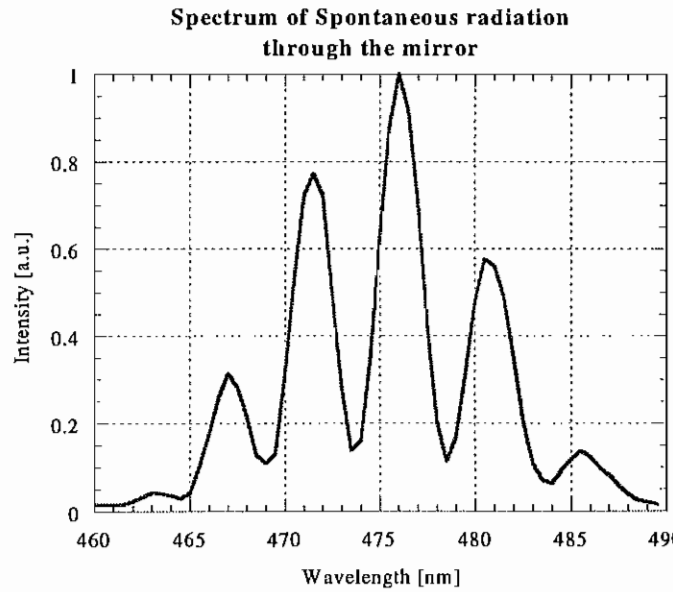

(b)

Fig. 3.3.3. Spectra of the spontaneous radiation from the OK-4 at 500 MeV electron beam energy.
(a) $I_e < \sim 1$ mA and $I_{BS} = 1.2$ kA: $N_d = 141.25$ and $f = \sim 0.63$, $\lambda = 222.47$ nm.
(b) $I_e = \sim 0.25$ mA and $I_{BS} = 1.2$ kA: $N_d = 70.45$ and $f = \sim 0.8$, $\lambda = 474$ nm.

$$\frac{\sigma_\varepsilon}{E_0} \cong \frac{\sqrt{-2\ln f}}{4\pi(N_w + N_d)}. \qquad (3.3.5)$$

Typical spectra at a buncher current of ~ 1.2 kA with 500 MeV electron beams are shown in Figure 3.3.3 at two different wavelengths. The modulation depths are ~ 0.63 and ~ 0.8 in (a) and (b), resulting in energy spreads of 5.10×10^{-4} and 4.46×10^{-4}, respectively. These values are a factor of 2 larger than the theoretically calculated natural energy spread, indicating the contributions of transverse size, angular spread, and dispersion in the monochromator.

3.4. Lasing

Lasing of the Duke/OK-4 SR FEL at deep UV and visible wavelength was achieved in 1998 and 1999. The condition for lasing and the laser tunability depend critically on the optical properties of the cavity mirrors. Our cavity mirrors were fabricated and coated at GSI Lumonics in Canada. The size of the cavity mirrors is large enough to capture the TEM_{22} mode of the optical beam. The materials for the multi-layered dielectric coatings are: HfO_2/SiO_2 for 245 nm, 380 nm, and the broadband visible range, Al_2O_3/MgF_2 for 225 nm, and Al_2O_3/SiO_2 on a Al_2O_3/MgF_2 multilayer for 200 nm. These cavity mirrors will be discussed in detail in Chapter 4. The lasing spectra and loss measurements are shown in Figure 3.4.1 – 3.4.5 [Litvinenko 1997,1998,1999a, 1999b] and the relevant parameters of the Duke/OK-4 SR FEL are listed in Table 3.4.1. As mentioned in Section 3.1, the FEL lased from 193.67 nm to 730 nm using the five different sets of optical cavity mirrors.

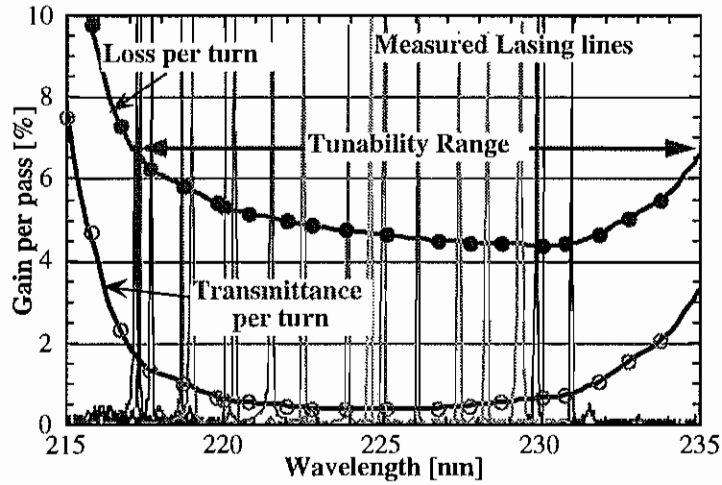

Fig. 3.4.1. Lasing spectrum, cavity loss, and gain per turn at the central wavelength of 225 nm. (Al_2O_3/MgF_2 dielectric multilayered cavity mirrors) (solid lines: measured lasing lines; –●–: cavity loss per turn; –o–: transmittance per turn)

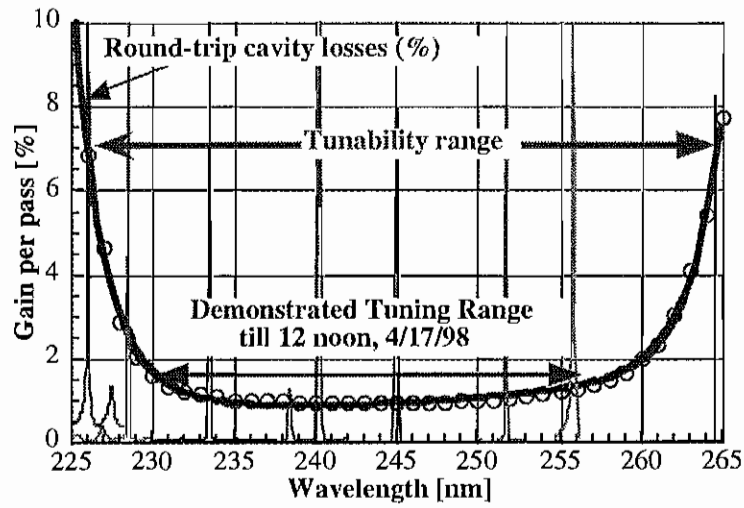

Fig. 3.4.2. Lasing spectrum, cavity loss, and gain per turn at the central wavelength of 245 nm. (HfO_2/SiO_2 dielectric multilayered cavity mirrors) (solid lines: measured lasing lines; –o–: cavity loss per turn)

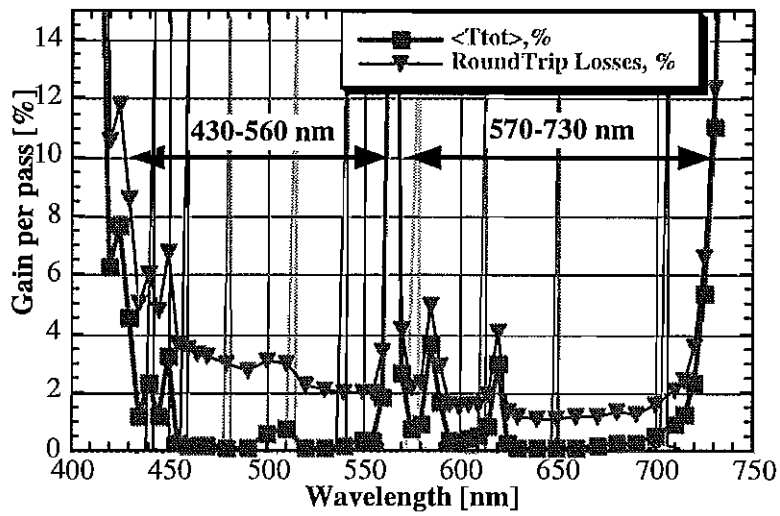

Fig. 3.4.3. Lasing spectrum, cavity loss, and gain per turn at broad band visible range. (HfO_2/SiO_2 dielectric multi-layered cavity mirrors) (solid lines: measured lasing lines; –▼–: cavity loss per turn; –■–: transmittance per turn)

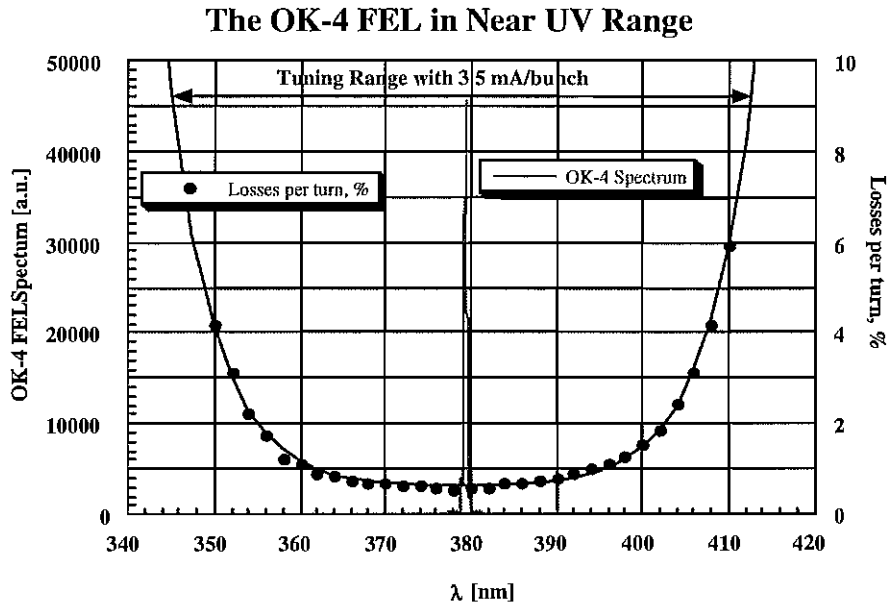

Fig. 3.4.4. Lasing spectrum, cavity loss, and gain per turn at the central wavelength of 385 nm. (HfO_2/SiO_2 dielectric multi-layered cavity mirrors) (solid lines: measured lasing lines; –●–: cavity loss per turn)

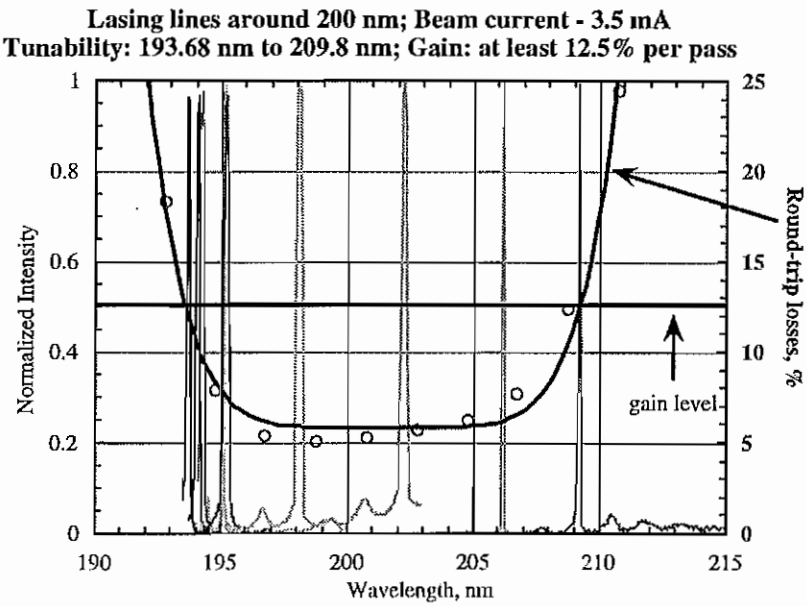

Fig. 3.4.5. Lasing spectrum, cavity loss, and gain per turn at the central wavelength of 200 nm. (The dielectric multilayered cavity mirrors coated with Al_2O_3/SiO_2 on the top of Al_2O_3/MgF_2) (solid lines: measured lasing lines; –o–: cavity loss per turn)

The resonator ring-down time is measured using either spontaneous radiation from the OK-4 or FEL light. Each time the electron beam is kicked out of orbit the decaying light signal is transmitted into a monochromator and then into the Hamamatsu photomultiplier, as shown Figure 3.4.6. The signal from the photomultiplier is displayed and measured using a LeCroy digital oscilloscope. The cavity losses are determined by the reflectance of the cavity mirrors. The gain per pass is approximately equal to the cavity loss on the edges of the tuning range of FEL wavelengths for given dielectric cavity mirrors, as lasers cannot operate when the cavity loss per turn is larger than the gain per turn. According to our measurements, the gain per round-trip at ~ 2 mA of electron beam current is

Table 3.4.1. Parameters of the Duke/OK-4 Storage Ring FEL.

Parameters	Projected	Demonstrated
Tuning range (fundamental) [nm]	50 - 800	193.7 - 730
Tuning range (harmonics) [nm]	4 - 100	
Electron beam energy for FEL [GeV]	0.25 – 1.0	0.24 – 0.8
Electron beam current for FEL [mA]	100	16
Average lasing power [W]	2 - 4	0.5 – 0.9 [a]
Extracted lasing power [W]	0.1 - 20	0.005 – 0.3 [b]
Giant pulses		
Repetition rate [Hz]	1 - 100	1 - 60
Extracted energy per macropulse [mJ]	20 - 200	0.05 – 3 [b]
Duration of macropulse [μsec]	30 - 100	1 - 60
Extracted peak power [MW]	3 - 100	0.1 – 0.3
Intracavity peak power [GW]	1 - 10	~ 0.1
Linewidth, $\Delta\lambda/\lambda$, natural	$(1-3) \times 10^{-4}$	$(1-4) \times 10^{-4}$
with linewidth narrowing	$(5-30) \times 10^{-7}$	28×10^{-7} [c]
Micropulse duration, σ_τ, natural, [psec]	3 - 30	1.4 - 26
Micropulse separation [nsec]	358.45 – 5.6	358.45 – 5.6
Spatial distribution	TEM_{00}	TEM_{00} [d]
Spectral brightness [number of photons/sec/mm^2/mrad^2/10^{3}BW]		
Average	5×10^{24}	$(2-4) \times 10^{20}$
Peak (CW mode)	~ 10^{27}	4×10^{24}
Peak (giant pulse mode)	~ 10^{30}	3×10^{26}
Compton γ rays		
Energy [MeV]	1 - 200	2 - 58
Total flux [γ's/sec]	10^8 - 10^{11}	$10^6 - 5 \times 10^7$
Energy resolution, FWHM, %	1	0.5 – 1
Polarization	~ 100 %	~ 100 %
Lifetime of electron beam [hr]	> 4	~ 3.5
Lifetime of laser [hr]	> 4	~ 3 [e]

[a] : *typical for 240 nm and 380 nm mirror sets*

[b] : *depends on wavelength and efficiency of extraction (~ mW at λ < 200nm and ~ 10^2 mW at λ > 230 nm)*

[c] : *demonstrated in 1990 with the OK-4 FEL in Novosibirsk* [Litvinenko 1991]

[d] : *observed up to* TEM_{22} *modes*

[e] : *continuous lasing is possible by continuously injecting the electron beam and lasing.*

approximately 6.5% at 217 nm, 6.9% at 226 nm, and 9.1% at 345 nm. The outcoupled power passing through the upstream cavity mirror is 23.6 mW at 4.2 mA of stored electron beam current operating at 600 MeV. The stability and lifetime of FELs are highly sensitive to the tuning conditions of the electron beam orbit, optical beam axis, and the high order modes of the RF cavity. The laser is more stable at high electron energy because the electron beam is more stable at high energies. The maximum stored current in a single bunch is limited by the vertical head-tail instability. We moved the betatron tunes below the quarter resonance in both the transverse motions. These betatron tunes avoid a strong vertical resonance. At this operating condition, we can store up to 20 mA in a single bunch, which results in a gain improvement of up to 15%. The high gain at this new operating point as well as the high radiation resistance of the Al_2O_3/SiO_2 dielectric coating makes it possible to lase at wavelengths below 200 nm.

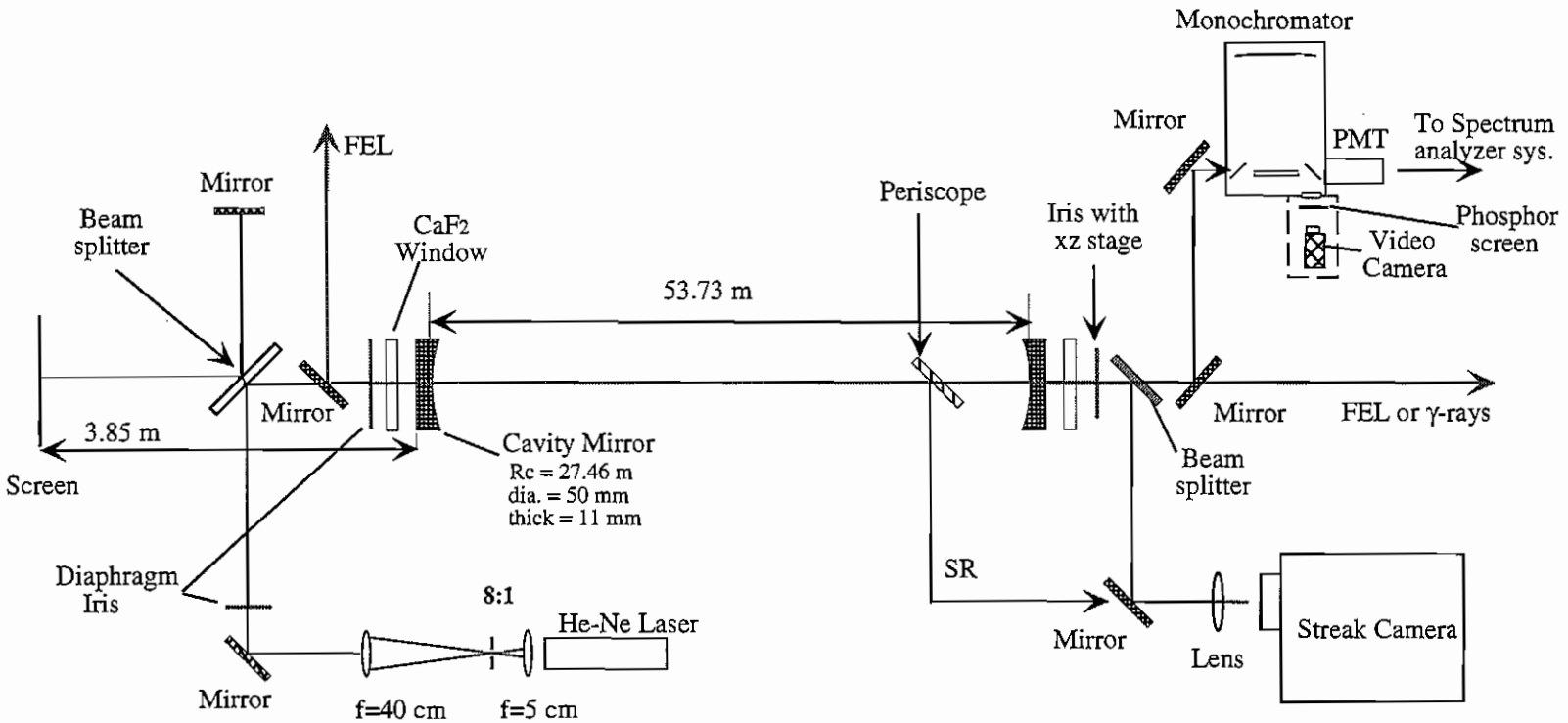

Fig. 3.4.6 Experimental setup of the optical tables for FEL operation.

The typical linewidth $\Delta\lambda/\lambda$ of the lasing lines is of the order of 10^{-4} as shown in Figure 3.4.7. The shortest lasing pulses observed were Fourier limited (the first Fourier limited pulse in SR FELs) and had a Gaussian shape with a 1.4 psec rms bunch length, as shown in Figure 3.4.8. The Fourier limit of 1.4 psec micropulses at a wavelength 385 nm gives a FWHM linewidth of 1.73 x 10^{-4}. At a wavelength of 218.65 nm, the Fourier limit of 1.4 psec micropulses will give a FWHM linewidth of 0.983 x 10^{-4}, which is in good agreement with the measured linewidth of 0.979 x 10^{-4} in Figure 3.4.7. Under these operating conditions, the laser power is steady, except for longitudinal time jitter at the few psec time scale. This jitter could be related to instability of the electron beam or the mirror feedback system.

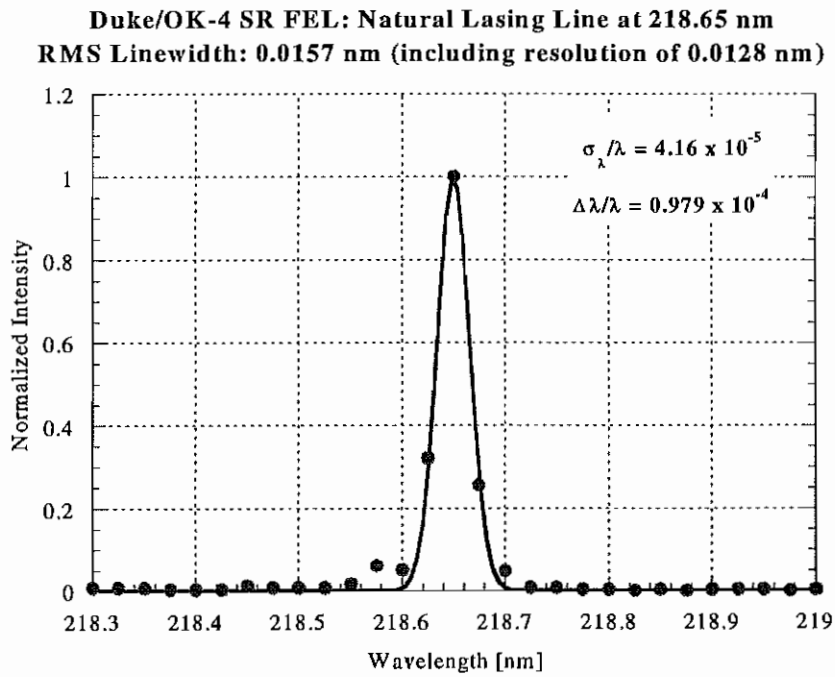

Fig. 3.4.7. Linewidth of the FEL light.

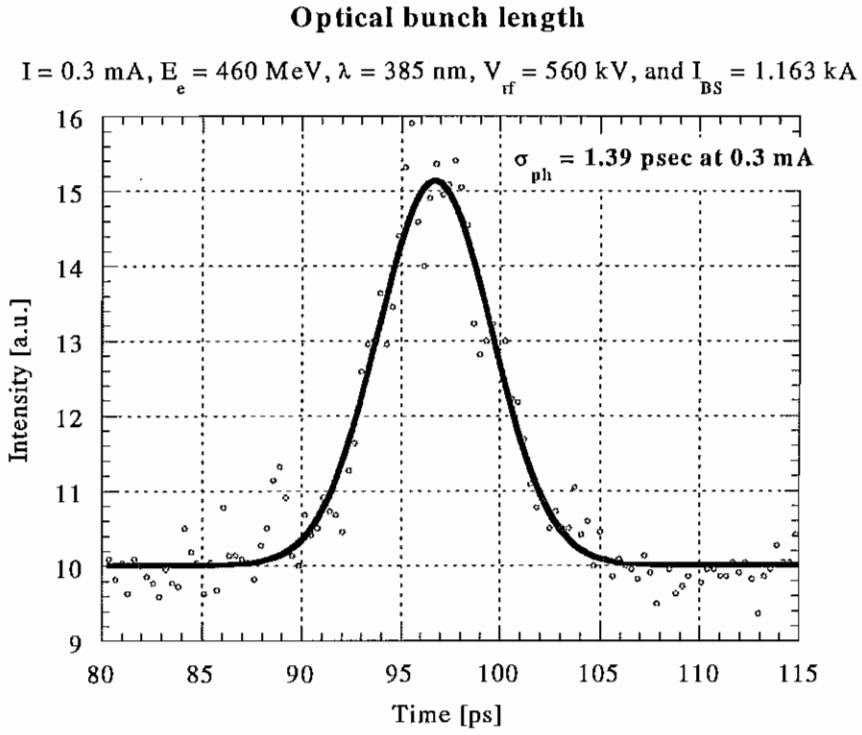

Fig. 3.4.8. Fourier limited optical pulse.

3.5. Saturation

The maximum saturated lasing power of the Duke/OK-4 FEL is given by

$$P_{ave,\max} \cong 2.07 \cdot P_{SR} \frac{\sigma_\varepsilon^2 - \sigma_{\varepsilon_0}^2}{\sigma_\varepsilon} e^{-1/2}, \tag{3.5.1}$$

where $\sigma_\varepsilon (=\sigma_E/E_0)$ is the induced energy spread due to the FEL interaction and $\sigma_{\varepsilon_0} (=\sigma_{E_0}/E_0)$ is the natural energy spread. J_ε is 2.07 for the Duke SR FEL. The

optical cavity efficiency η_c is defined as: $\eta_c \equiv$ (transmittance of mirror)/(cavity loss per turn). This efficiency is equal to the ratio of measured FEL power to optimum FEL power (which is calculated theoretically). Using the experimentally measured induced energy spread and laser power, the cavity efficiency of the Duke/OK-4 FEL at a 600 MeV electron energy and 370 nm laser wavelength is approximately 0.5. This efficiency agrees with the predicted ratio of the transmittance of the cavity mirror to the cavity loss measured. Figures 3.5.1 and 3.5.2 illustrate the dependence of FEL power on the electron beam current. The theoretical calculations use experimentally measured parameters, i.e., the induced energy spread of the electron beam and the optical cavity efficiency. These theoretical predictions agree with the experimental data.

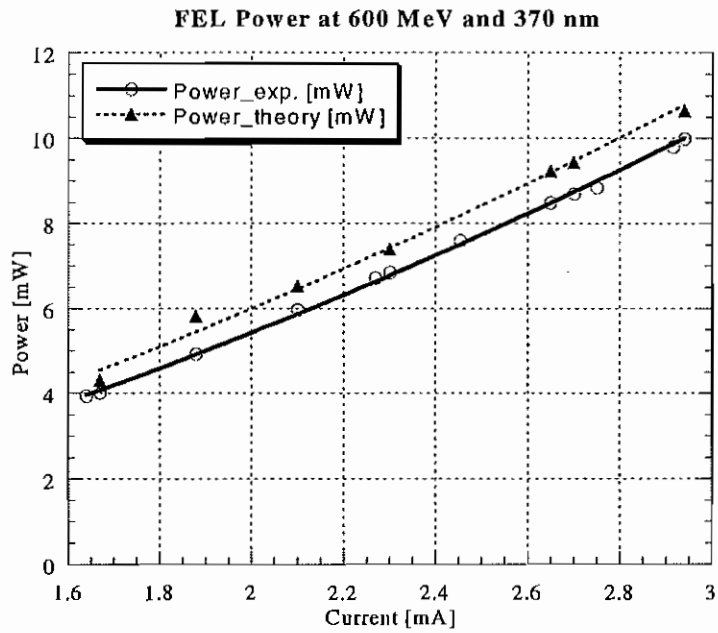

Fig. 3.5.1. The FEL power with respect to e-beam current in FEL mode operation.
(○: Experimental measurements; ▲: Theoretical calculation using measured energy spread of electron beam and optical cavity efficiency; at 600 MeV , 370 nm, and 600 kV RF voltage)

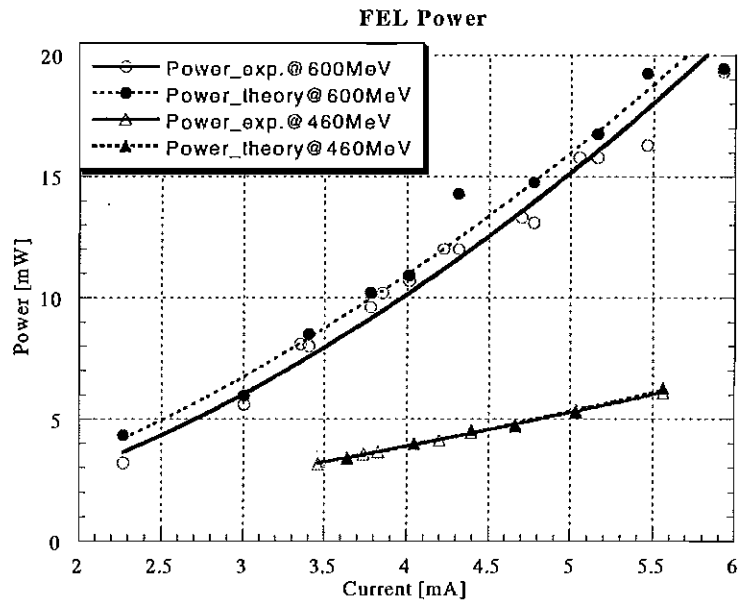

Fig. 3.5.2. The FEL power with respect to e-beam current in γ-ray mode operation.
(○: Experimental data; ●: Theoretical calculation at 600MeV and 370 nm, 600 kV RF voltage)
(△: Experimental data; ▲: Theoretical calculation at 460MeV and 385 nm, 500 kV RF voltage)

The FEL power at 600 MeV is approximately 2.89 times larger than the power at 460 MeV because the saturated power is proportional to E_e^4 as mentioned in Section 2.5. Small discrepancies between the experimental data and the theoretical estimate are caused by measurement errors of the parameters.

As mentioned in Section 2.2, an increase of the slippage at the bunching section increases the gain and reduces the homogeneous width of the gain curve. The slippage at the bunching section is proportional to I_{BS}^2 (I_{BS}: buncher current) and inversely proportional to E_e^2 (E_e: electron energy). One can vary the slippage by changing the buncher current. The dependence of FEL power on buncher current is given in Figure 3.5.3. At lower buncher currents, saturation occurs when the FEL

interaction increases the bunch length of the electron beam which decreases the peak current so that the gain per turn is reduced almost to the cavity loss per turn. In this case, the induced energy spread of the electron beam is less than in the optimal case. In the optimal regime, the energy spread of the electron beam is related to the total slippage as follows:

$$\frac{\sigma_E}{E} = \frac{1}{4\pi(N_w + N_d)}. \tag{3.5.2}$$

As the buncher current increases (i.e., N_d increases), the early saturation occurs when the induced energy spread of the electron beam reaches a level just above that given

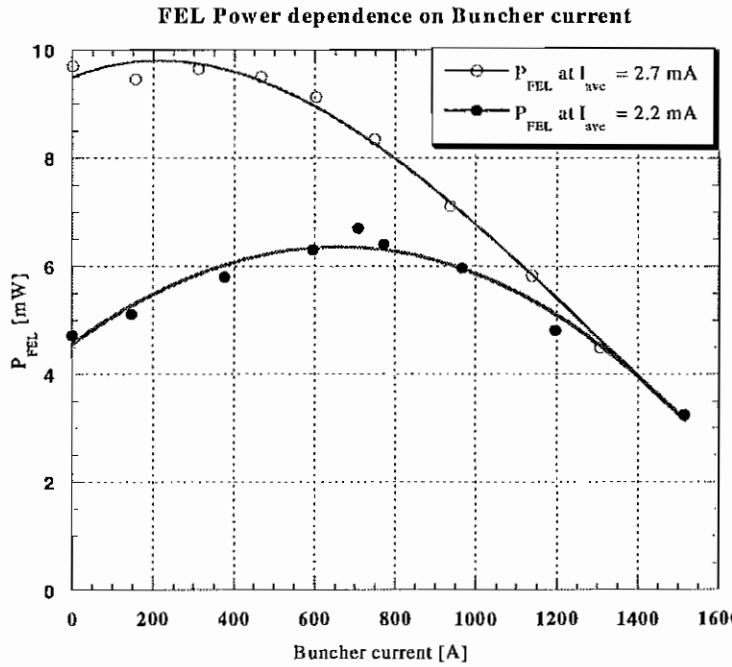

Fig. 3.5.3. The FEL power with respect to buncher currents. The electron beam energy is 600 MeV, the FEL wavelength is 370 nm, and RF voltage is 550 kV. (○: ~ 2.7 mA average current; ●: ~2.2 mA average current)

by Equation 3.5.2. It means that an increase of N_d causes the reduction of the induced energy spread and the power. If we optimize the lasing power using N_d satisfying Equation 3.5.2, the FEL gain is proportional to the bunch current and inversely proportional to the square of energy spread (see Equation 2.4.14 and Equation 2.5.8 to find that $\sigma_s = b\sigma_E$). At the same time, in a steady state, the FEL gain is equal to the loss of the optical cavity. It means that in optimal conditions (i.e., Equation 3.5.2) the energy spread is proportional to the $I_b^{1/2}$ (because $G_{th} = G_{FEL} \sim I_b/\sigma_E^2$). Therefore, from Equation 2.5.31, the maximum FEL lasing power will grow with its bunch current as $n_b I_b^{3/2}$, because P_{SR} is proportional to the bunch current and number of bunches n_b.

3.6. Temporal structure

FEL performance is sensitive to the tuning condition between the optical bunch and the electron bunch. As shown in Figure 3.6.1, the detuning range of natural lasing for a ring current of 3.6 mA is approximately 4 Hz which corresponds to a cavity length detuning range of 0.15 mm. A Molectron power meter is used to measure the average laser power, while a silicon photodiode (fast response time of about 3 μsec) is used to observe the macro-temporal structure of the laser power. When the optical bunch is synchronized with the electron bunch, the macrostructure of the FEL is a continuous wave (CW) mode that has the maximum lasing power and minimum bunch length. The bandwidth of the CW zone is very narrow at the center of the

detuning curve, approximately 0.05 Hz ($\Delta L_c \approx 2$ μm) at 3.6 mA and 600 MeV. The bandwidth becomes wider at a higher ring current per bunch and at higher operating energies. This indicates that stability of the electron beam is better at the higher ring energies. The stability of the CW laser is also sensitive to the higher order modes of the RF cavity.

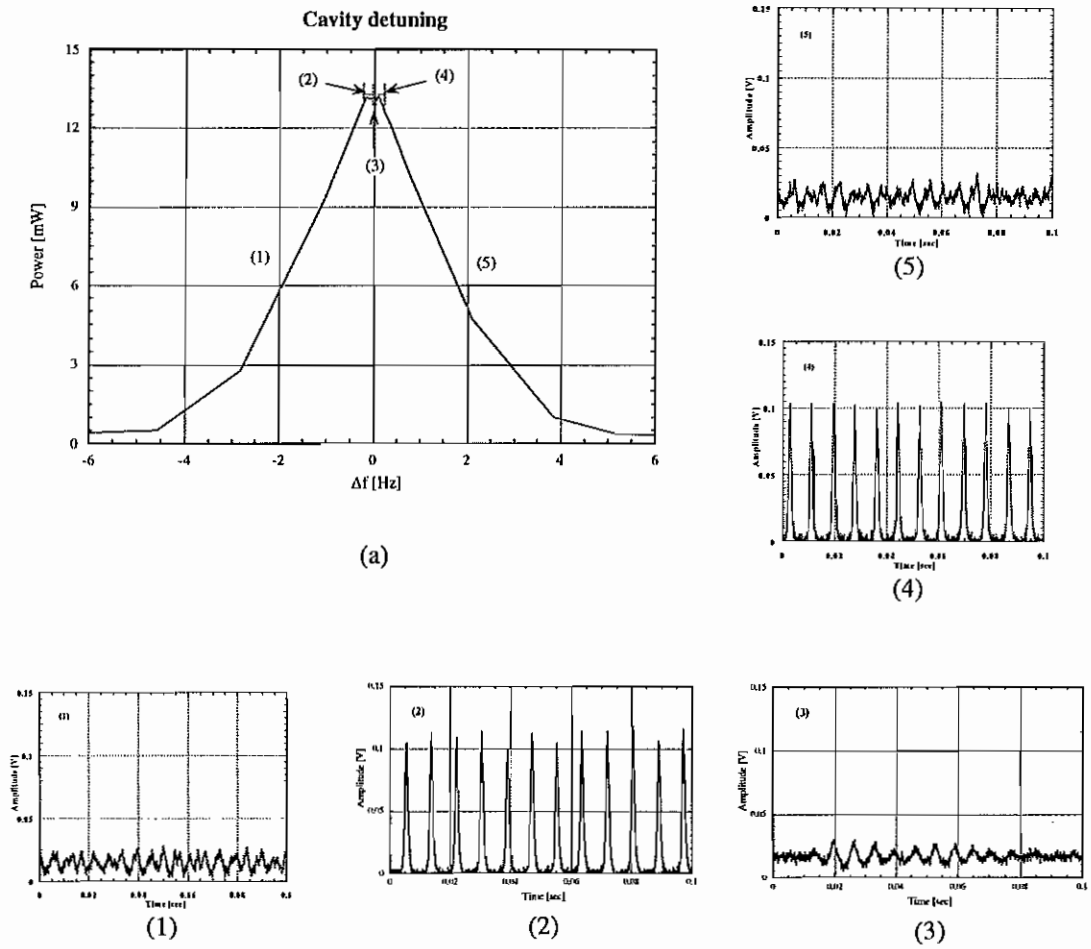

Fig. 3.6.1. The OK-4 FEL cavity detuning curve and typical macro-temporal structures measured at I_e = 3.6 mA, E_e = 600 MeV, λ_{FEL} = 385 nm, and V_{rf} = 600 kV. (a) Average power measured by Molectron power meter: the signal is ~ 73% of outcoupled average power through the upstream cavity mirror. (1) – (5) are temporal macro-structures at each zone measured by Si photodiode and LeCroy digital oscilloscope: the signal is only ~ 6.4% of outcoupled power.

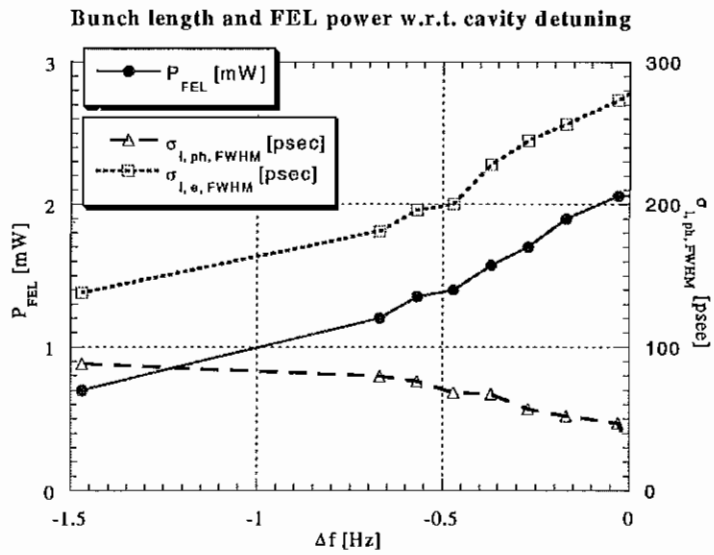

Fig. 3.6.2. Bunch length and FEL power with cavity detuning measured at 460 MeV and 500 kV. As the revolution frequency is detuncd, the optical bunch length increases and the FEL power and the induced bunch length of electron beam decrease.
(•: FEL power; △: FWHM optical bunch length; □: FWHM electron bunch length)

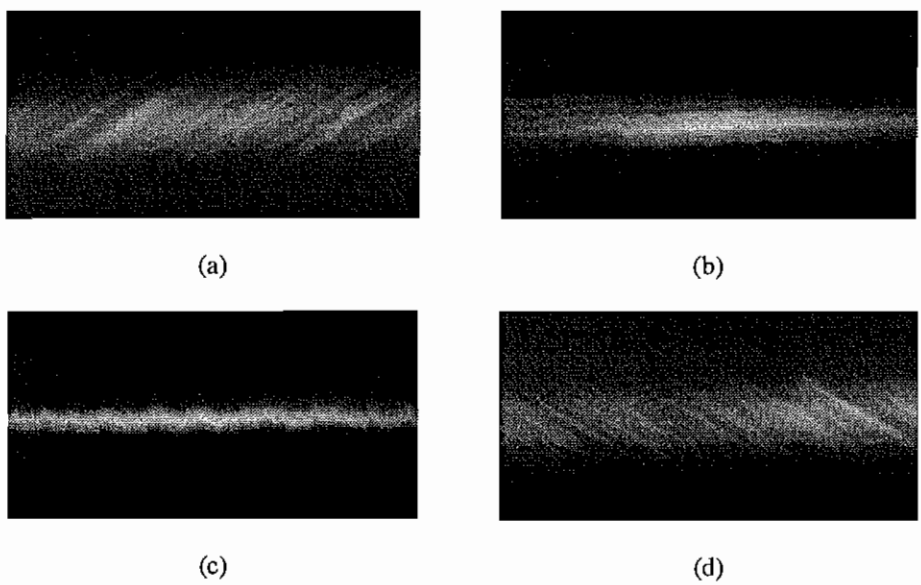

Fig. 3.6.3 Temporal structure behavior as a result of detuning the cavity length. The cavity length is detuned by changing the revolution frequency of the electron beams. When tuned, the FEL has CW modes (c) and the shortest temporal bunch length. (a) –> (d) shows the temporal structures as the cavity length inereases.

If the electron beam and the optical beam are detuned slightly by a few steps of 0.01 Hz, the laser power becomes pulsed with a repetition rate of 120 Hz. A pulsed mode exists on both sides of a perfectly tuned CW zone over the range of approximately 0.2 Hz. The periodic behavior of the OK-4 FEL is caused by gain modulation due to variations of the electron beam parameters. Since the 120 Hz frequency is twice the frequency of the main power line, the noise in the power supplies are one of the main perturbations to the stability of the CW mode. As the detuning increases, CW lasing appears again. In this regime, the lasing becomes much more stable, but the bunch length is longer and the laser power is decreased as shown in Figure 3.6.2. Figure 3.6.3 shows the typical temporal behaviors of the Duke/OK-4 SR FEL as the optical cavity length is detuned by changing the revolution frequency of the electron beams.

The bunch lengths of both the electron beam and the optical pulse were measured to within a resolution of 4.34 pixels using additional lens input optics and a 30 μm pinhole slit, which corresponds to 2.5 psec resolution in Range 2. To study the micro-temporal structure of the optical beam or electron beam with the laser-off, we used Range 1 (full time scale of 150 psec). Range 2 (full time scale of 700 psec) was used for simultaneous measurements of the micro-temporal structure of the electron beam and the optical beam during FEL operation. The typical rms bunch length of the optical pulse of the synchronized CW laser is about 9 psec for stored currents of approximately 2 to 3 mA, whereas the rms bunch length of the electron beam is about 45 psec with a rms induced bunch length of about 120 psec due to

FEL interactions. When not lasing, the electron bunch length and the energy spread are determined by the saturated microwave instability, $\sigma_{l,e} \propto (I_{ave}/V_{RF})^{1/3}$.

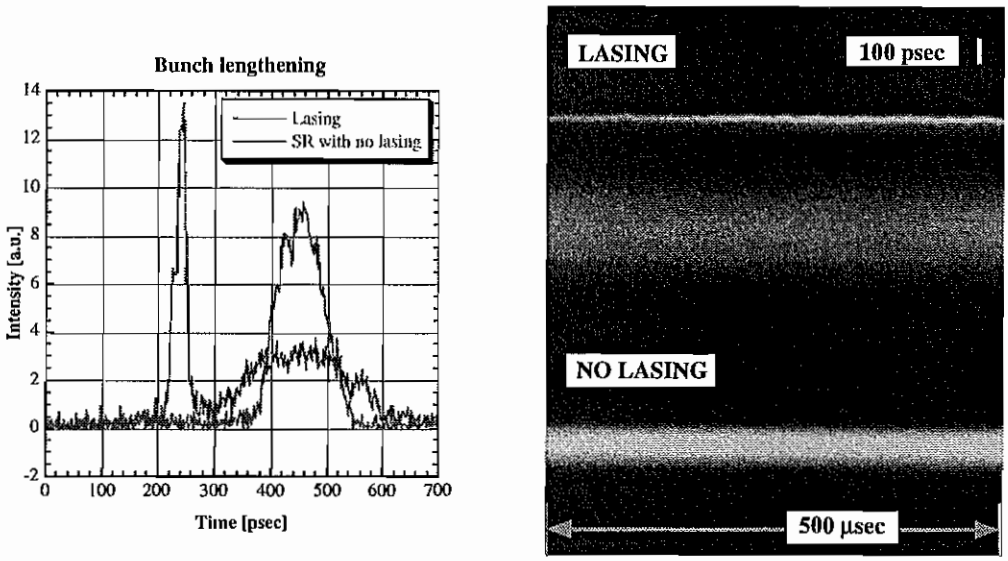

Fig. 3.6.4. Bunch lengthening measured using Hamamatsu streak camera in dual sweep mode.

The typical bunch lengthening due to the FEL interaction is a factor of 2.4, as shown in Figure 3.6.4, while the maximum observed factor is 3.36. Therefore, the microwave instability could be suppressed by increasing the energy spread induced FEL lasing. Figure 3.6.5 shows the bunch length of the electron beam without lasing (i.e., determined by microwave instabilities) and with lasing and the theoretical calculations of the bunch length due to the microwave instability as a function of the average beam current. The measured bunch lengthening was a factor of 2.15 at low

current and 2.5 at high current. This indicates that the induced energy spread due to the FEL interaction suppresses the microwave instability.

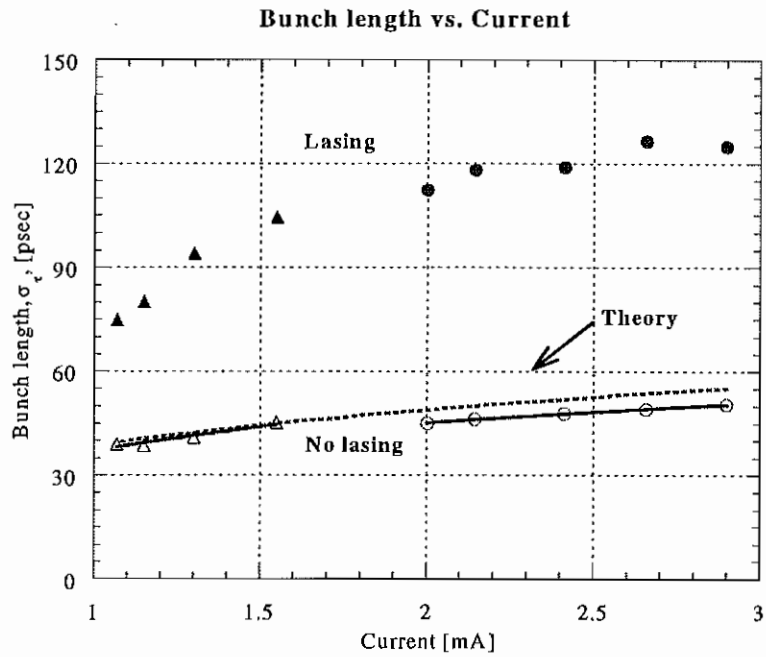

Fig. 3.6.5. Dependence of the bunch length of the electron beam on stored current. The measurement was performed at a 460 MeV operating energy and a 500 kV RF cavity voltage. The dashed curve shows the theoretical curve for bunch length as a function of average ring current.

3.7. Transverse mode structure

When the electron beam axis and the optical axis coincide, the transverse mode structure of the Duke/OK-4 SR FEL is typically a Gaussian TEM_{00} mode. The size of the TEM_{00} mode at 1.13 m from the cavity mirror is 3.73 mm (w), which results in a Rayleigh range of 3.36 m and waist at the focal point of 0.629 mm (w_0) at a wavelength of 370 nm. When the cavity mirrors are mechanically distorted, the

round shape becomes elliptical due to an asymmetric radius of curvature. We discuss the effect of these mechanical distortions in detail in Section 4.4. As the electron beam position shifts with respect to the optical axis, one observes higher order transverse modes. Using Equation 2.4.5, one can plot the expected transverse mode on the cavity mirror as shown in Figure 3.7.1. The same set of transverse modes observed in the Duke/OK-4 SR FEL is shown in Figure 3.7.2. The highest order mode observed depends on wavelength, for example, a TEM_{22} mode at 370 nm and a TEM_{33} mode below 240 nm.

The average power is smaller for high order modes, because the gain for the high order modes and the filling factor (ratio of the overlap in transverse size of the electron beam and optical beam) are lower. Table 3.7.1 lists the average FEL power for different transverse modes and electron beam orbits in the interaction region.

Current [mA]	Power [mW]	e-beam orbit [mm]	TEM modes
1.31	0.12	(+0.59, 1.0)	TEM_{11}
1.27	0.20	(+0.12, 0.87)	TEM_{01}
1.24	0.92	(-0.1, 0)	TEM_{00}

Table 3.7.1 FEL power vs. the transverse mode structure at 500 MeV and 380 nm. The e-beam orbit (x_1, x_2) indicates that x_1 is the x position before entering the wiggler and x_2 is the x position after passing the wiggler orbit positions.

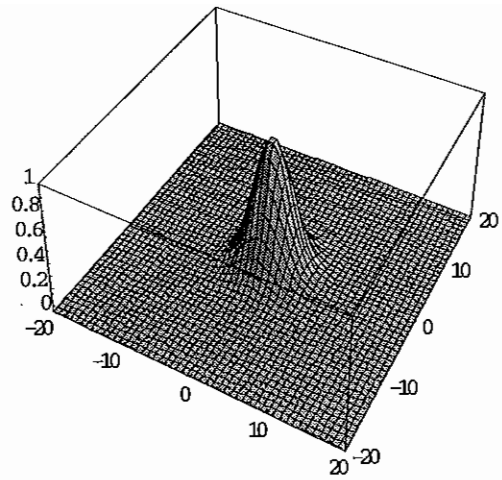

(a) TEM_{00}

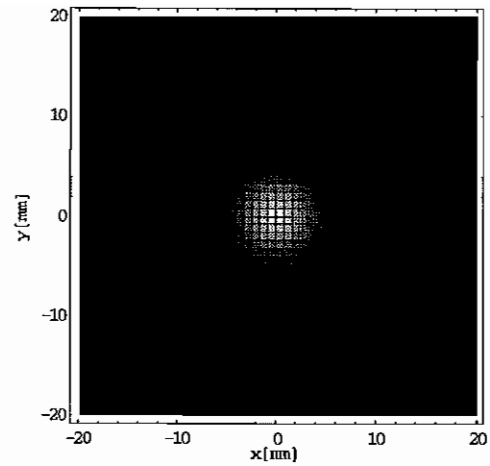

(b) TEM_{00}

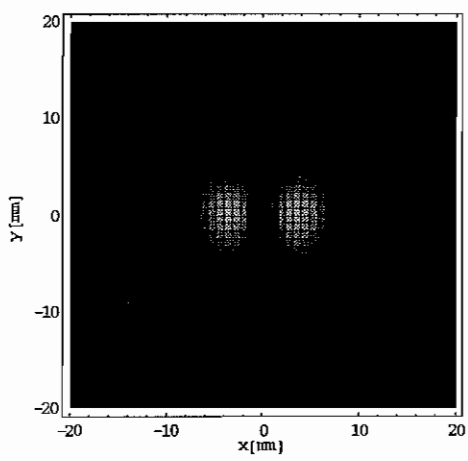

(c) TEM_{10}

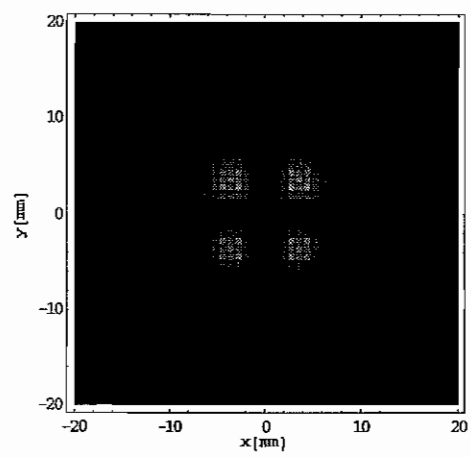

(d) TEM_{11}

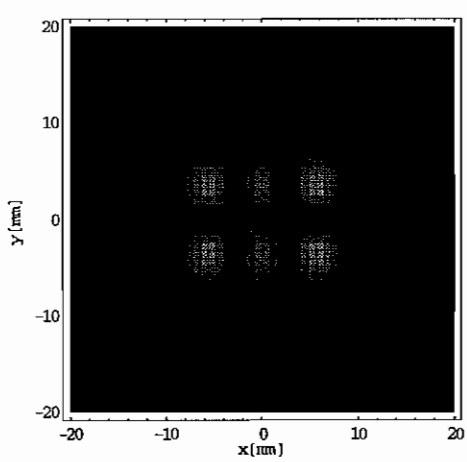

(e) TEM_{21}

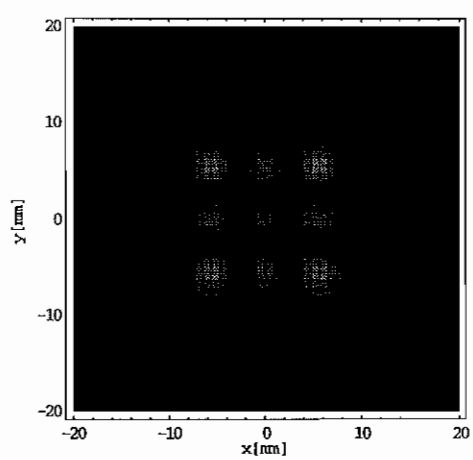

(f) TEM_{22}

Fig. 3.7.1. Transverse mode structures of Hermite-Gaussian modes.

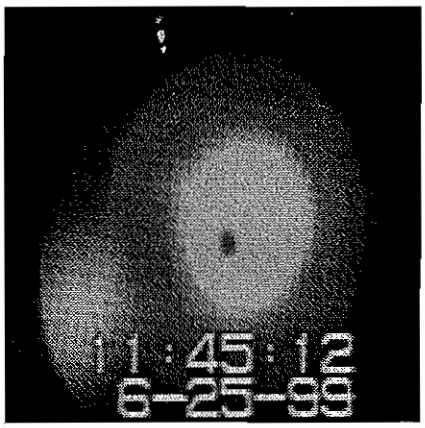

TEM_{00}

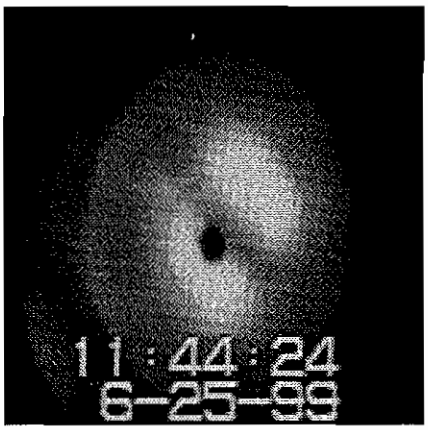

TEM_{10}

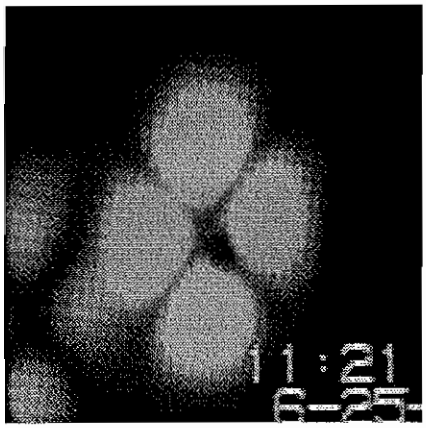

TEM_{11}

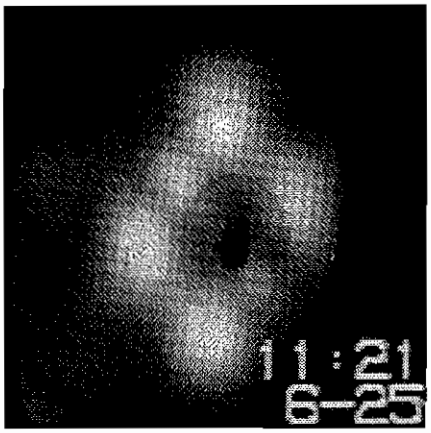

TEM_{21}

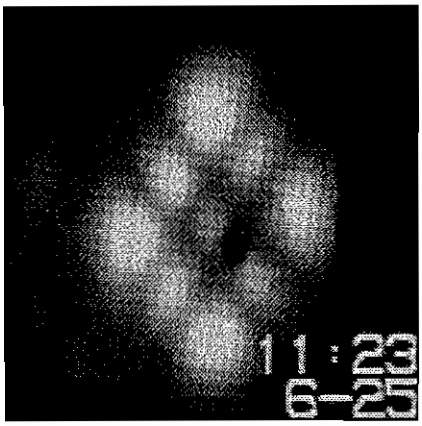

TEM_{22}

Fig. 3.7.2 Transverse mode structures of the Duke/OK-4 FEL.

In order to maximize FEL power, the electron beam and optical beam should overlap in the interaction region. Table 3.7.2 demonstrates the changes of the beta function and focal point of the electron beam in the OK-4 in the two different optical beam transverse profiles. The measurement errors of the beta function of the electron beam and the Rayleigh range of the optical beam are approximately 20% and less than 10% respectively. Because of mechanical distortions and manufacturing errors, the broadband mirrors have strong astigmatism resulted in elliptical profiles of the TEM_{00} mode. The Raleigh ranges and focal points along two axis of the ellipse are shown in Table 3.7.2. They are different from designed parameters.

	At 385 nm (385 nm cavity mirrors)		At 600 nm (broadband cavity mirrors)	
	β_0 [m]	z_0 [cm]	β_0 [m]	z_0 [cm]
Electron beam	3.838	22.6	3.537	87.7
Optical beam (axis 1)	3.359	~ 0	0.85	183.2
(axis 2)			1.96	156.0

Table 3.7.2. Rayleigh range β_0 and location of focal point z_0 of the electron and optical beams. (The optical beam transverse profiles are circular at 385 nm and elliptical at 600 nm.)

Chapter 4

Optical cavity

4.1. Introduction

The geometry of the Duke/OK-4 storage ring FEL resonator is both nearly concentric and symmetric and has a cavity length of 53.73 m, which is one half of the circumference of the Duke storage ring. In order to synchronize the optical and the electron bunches, the optical cavity length must satisfy the condition that $mL_c = nC_0$ (where m and n are integer numbers). We chose m = 2 and n = 1 because the cavity mirrors must be placed outside of the 34 m long narrow straight section for the interaction region in order not to interrupt the electron beam pass. For long cavity lengths, the resonators most commonly used are of the near-concentric type to optimize the overlap between the optical beam and the electron beam. An advantage of this configuration is that the reduced density of power on the cavity mirrors reduces the radiation damage of the cavity mirrors. However, the resonator is highly sensitive to misalignment and this sensitivity increases at longer wavelengths. The cavity mirror in the Duke/OK-4 FEL is 50 mm in diameter, 11 mm in thickness, and has a 27.27 m radius of curvature. The radius of curvature is chosen to optimize the gain at wavelengths of approximately 200 nm for the OK-4 geometry by avoiding

the diffraction loss due to the vacuum chamber (beam line). Theoretically, the maximum gain occurs at $\beta_0 \approx L_w/2$ (β_0: Rayleigh range, L_w: wiggler length) for a Gaussian optical wave. However, the Duke/OK-4 has $\beta_0 \cong L_w$. The stability parameter g (a measure of the sensitivity) and the Fresnel number N_F (a measure of the diffraction) are related by [Siegman 1986]

$$g^2 = g_1 g_2 = \left(1 - \frac{L_c}{R_1}\right)\left(1 - \frac{L_c}{R_2}\right) \text{ and } \quad N_F = \frac{a^2}{\lambda L_c} \tag{4.1.1}$$

where L_c is the cavity length, R_i is the radius of curvature of the cavity mirror, and a is the radius of the cavity mirror. For the Duke/OK-4, $g_1 = g_2 = g = -0.97$ and N_F is 60 at 193 nm and 16 at 720 nm. The main diffraction loss arises from the vertical dimension of the temporary crotch chambers where the electron beam is deflected from or into the optical beam axes. The Fresnel number, as determined by the vertical dimension of the crotch chamber, is reduced by a factor of 2.5. With these parameters, the main concerns for the Duke optical cavity (especially in the UV and VUV spectral ranges) are its sensitivity to angular misalignment and changes in optical mode parameters caused by thermal or mechanical distortions of the cavity mirrors. Below, we estimate the tolerances of the Duke optical system to angular misalignments, thermal heating, and mechanical stress.

4.2. Misalignments

For resonators with spherical mirrors, the optical field always passes along the optical axis, a line that connects the centers of curvature of the two cavity

mirrors. In a near-concentric optical cavity, the optical axis is considerably tilted by small angular misalignments of the cavity mirrors. This sensitivity is due to the fact that the centers of curvature are close to one another. Assuming that the positions of the cavity mirrors do not move, the new optical axis shifted through angular misalignments $\Delta\theta_i$ of mirror M_i (i = 1,2) can be expressed by an angle θ_{new} as (see Figure 4.2.1):

$$\tan\theta_{new} = \frac{R_1 \sin\Delta\theta_1 - R_2 \sin\Delta\theta_2}{R_1 \cos\Delta\theta_1 + R_2 \cos\Delta\theta_2 - L_c}, \tag{4.2.1}$$

$$C_i' = \left(R_i \cos\Delta\theta_i - L_c/2, R_i \sin\Delta\theta_i\right), (i = 1,2),$$

where C_i' (i = 1,2) are the new centers of the radii of curvature. Since $a/L_c \sim 10^{-3}$ radians in the Duke/OK-4, $\Delta\theta_i << 1$ and for $R_1 = R_2 = R_c$,

$$\theta_{new} \approx \frac{\Delta\theta_1 - \Delta\theta_2}{1+g}. \tag{4.2.2}$$

The corresponding changes in the cavity length and the Rayleigh range are small, because they depend on second order angular shifts. The new focal point becomes

$$\mathbf{x}_f \equiv (x_f, z_f) \approx \frac{R_c(\Delta\theta_1 + \Delta\theta_2)}{2}\left(\frac{1}{2}(\Delta\theta_1 - \Delta\theta_2), 1\right). \tag{4.2.3}$$

The acceptance angle (which is the maximum angle where the laser still works) is limited by the size of the cavity mirrors or the vacuum chamber (the diffraction of the optical beam). To minimize diffraction loss, the cavity mirrors must capture at least α times the optical beam waist w_m at the cavity mirror, satisfying $\alpha w_m > R_c\theta_D$, where θ_D is the far field diffraction angle, $\sqrt{\lambda/\pi\beta_0}$. For the lowest optical mode, TEM_{00},

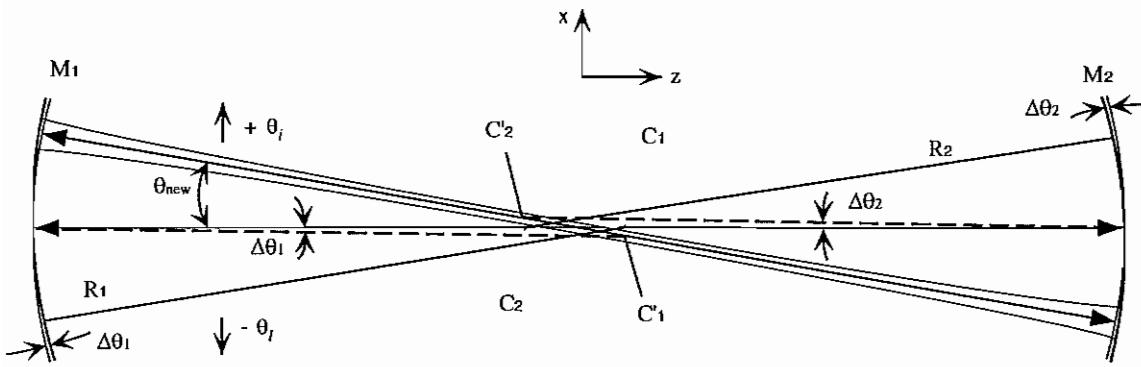

Fig. 4.2.1. New optical axis of the optical cavity due to angular misalignment of mirrors.
C_i : Center of curvature of mirror M_i, (i = 1, 2)
C'_i : Center of curvature of mirror M_i after a tilt by $\Delta\theta_i$, (i = 1, 2)
θ_{new} : Angle of the new optical axis with respect to the designed optical axis

		$\alpha = 1.5$		$\alpha = 2.0$	
Wavelength [nm]	Opening size [cm]	Tolerance $\Delta\theta_{max}$ [μrad]	Acceptance θ_{new} [μrad]	Tolerance $\Delta\theta_{max}$ [μrad]	Acceptance θ_{new} [μrad]
193	2.00	7.87	530	6.87	462
	1.58	5.59	376	4.58	308
720	2.00	5.06	341	3.12	210
	1.58	2.78	187	0.83	56

Table 4.2.1. Tolerance and acceptance angles due to angular misalignments.
(The diffraction loss is larger for smaller values of α.)

$$|\theta_{new}| < \frac{1}{R_c}(a - \alpha w_m) \text{ and } |\Delta\theta_i| < \frac{1}{2R_c}(a - \alpha w_m)(1+g), \text{ for } i = 1,2. \quad (4.2.4)$$

Since the cavity is limited by the size of the beam line pipe and not the mirror size, we use a_h = 1.58 cm and a_v = 2 cm, which are the opening sizes of the beam line pipe. Table 4.2.1 shows the maximum acceptable angle θ_{new} and maximum tolerance $\Delta\theta_{max}$ for wavelengths λ = 193 nm and 720 nm. As expected, the acceptable vertical angle is smaller than the horizontal one. The diffraction loss at longer wavelengths is increasingly sensitive to angular misalignments due to larger mode sizes at longer wavelengths. An accuracy of better than 10^{-6} radians is required for the mirror control system.

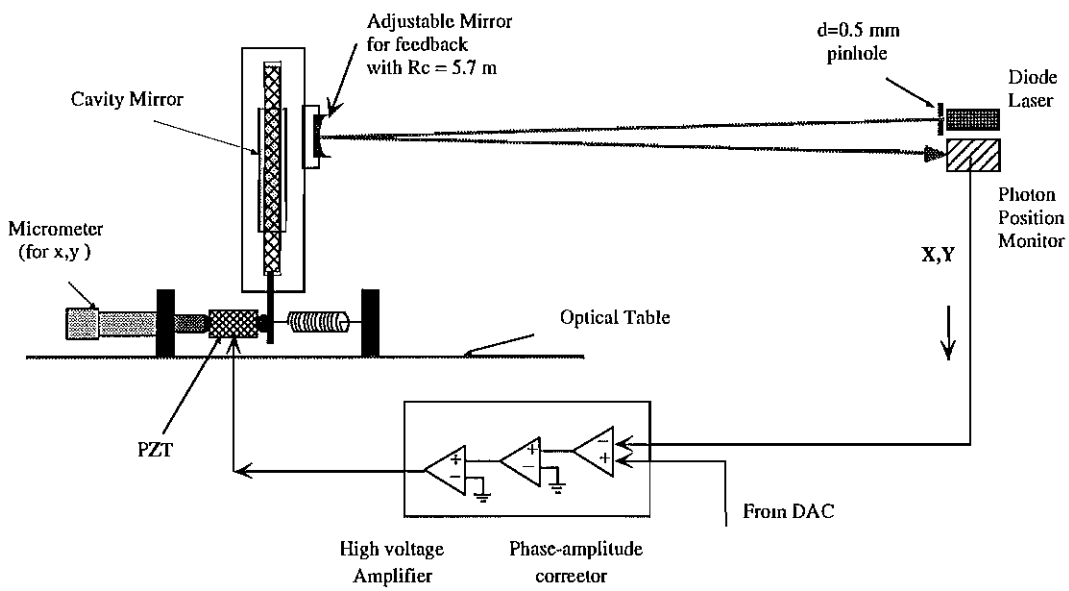

Fig. 4.2.2. Schematic layout of mirror feedback system.

The mirror feedback/control system [Pinayev 1998] (shown in Figure 4.2.2) was installed to compensate for external vibrations from the floor and air pressure. Small angular displacements of the cavity mirror are amplified by the geometry of 1:1 mirror optics in the feedback system and are stabilized by the feedback loop. The radius of curvature of the feedback system mirror is 5.7 m. The feedback system utilizes a two-dimensional position sensitive photodetector (S2044, Hamamatsu) that has a resolution better than 2.5 μm. The resolution of this system is given by $\Delta\theta \approx \Delta x/2l$ which results in a resolution of ~ 0.22 μrad, where $\Delta\theta$ is the angular displacement of the cavity mirror, Δx is the transverse displacement of the pinhole image of the diode laser, and l is the distance between the feedback system mirror and the photodetector. Since the adjustable range of the piezotranslator on the Gimble mirror mount is limited, a He-Ne laser is used for pre-alignment of the cavity mirrors to bring the cavity within the acquisition range of the mirror control system (below ~ 200 μrad). By using the EPICS (Experimental Physics and Industrial Control Systems) based control system, the position and angle of the optical cavity axis can be controlled within a step of 4×10^{-8} radians. The observed mirror vibrations are below 0.1 μrad, however, slow drifts and non-linearity in the electronics are still problematic. As this system is mounted outside the vacuum chamber (so it is easy to manage), noise from variations in air pressure and air flow can effect the stability of the FEL light.

4.3. Thermal distortions

High power of spontaneous radiation arising from the high harmonics radiation of the OK-4 wigglers (at high K_w and high electron energy) can distort the downstream mirror of the optical cavity. Since the average power in a storage ring FEL is small due to the saturation mechanism mentioned in the previous section, heating due to the FEL light is not significant. However, high harmonics from the wiggler do degrade the downstream mirror as the absorption coefficients of the mirror are large for these wavelengths. The thermal bowing increases the optical mode size and Rayleigh range, therefore reducing FEL gain.

We have investigated thermal distortions caused by the spatial power distribution on the downstream cavity mirror. For 20 mA of 750 MeV stored electron beam and for K_w = 4, the total absorbed power is 8 Watts. The heat transfer and thermal stress on the fused silica mirror substrate (50 mm in diameter and 11 mm thick) was computed using the finite element analysis package ANSYS (Swanson, Inc.). In this calculation it is assumed that the mirror makes uniform contact with the mirror holder around its edge and that the boundary condition satisfies $\Delta T = 0\ ^{\circ}C$. It is also assumed that the mechanical stress from the mirror holder is negligible. The new radius of curvature is calculated by minimizing the deviation $\delta z(x,y)$. Using an elliptic paraboloid wavefront equation [Thomas 1969], we can write the mirror deflection function in a first order perturbation as:

$$z(x,y) = \alpha_x x^2 + \alpha_y y^2 + \delta z(x,y), \qquad (4.3.1)$$

resulting in $R_{x,y} \approx \frac{1}{2\alpha_{x,y}}$ for a small deviation $\delta z(x,y)$. Because of the asymmetric distribution of the radiation power, the new radii of curvature differ in the x and y directions. As shown in Table 4.3.1, the estimated values for the radii of curvature are R_x = 27.640 m and R_y = 27.814 m for a 25 mm diameter opening to the TEM_{00} laser beam. These differ from R_c by 1.36% and 2.0% respectively. The maximum deviation δz and the rms deviation from the new radii of curvature are 3.8 nm and 0.92 nm, respectively. The increase of the mode size is about 10.0% in the horizontal direction and 13.8% in the vertical direction, which causes gain reduction. Also, one expects that in the γ-ray mode the flux of γ rays will be reduced not only due to an increase in the waist size but also in a shift of the focal point away from the collision point.

	ROC [m]	β_0 [m]	w_0 [mm]	$w_{m,\,DM}$ [mm]	$w_{m,\,UM}$ [mm]	focal point [cm]
R_c	27.27	3.30	0.450	3.694	3.694	(0, 0)
R_x	27.64	3.98	0.495	3.397	3.350	(- 18.93, 0)
R_y	27.81	4.26	0.512	3.298	3.232	(- 27.89, 0)

Table 4.3.1. Changes in optical modes of 200 nm optical beam due to thermal defocusing. (ROC: radius of curvature; DM: downstream mirror; UM: upstream mirror)

Through 1999, the FEL was operated mostly at a low average power with electron beam currents of less than 10 mA. For these conditions, there were no

significant changes in the optical mode waists in either the downstream or upstream mirrors. However, cavity losses were observed to increase over a long time scale.

When the FEL was operated at higher currents (above 20 mA) in four bunches, we observed a sudden shift of the optical axis and a drop in power. This is evidence of thermal expansion, i.e., the movement of the cavity mirror due to thermal heating. The power level and optical axis can be restored by adjusting the downstream mirror. This sudden slippage arises when the force generated by the thermal expansion of the mirror exceeds the strength of the finger clips which hold the mirror in place.

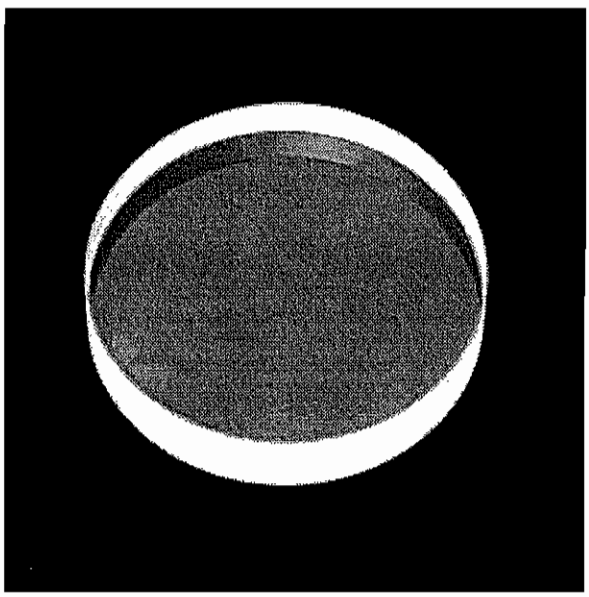

Fig. 4.3.1. Color change of the downstream mirror due to high harmonic radiation from the OK-4. (The picture is taken after one month of operation.)

We observed color changes in the downstream cavity mirrors which are caused by the high harmonic radiation from the wiggler. These changes are mostly due to carbon deposition on the mirror surface and are removable with cleaning. Figure 4.3.1 shows a downstream mirror after one month of operation that has a "footprint" of the beam line vacuum chamber, indicating radiation damage.

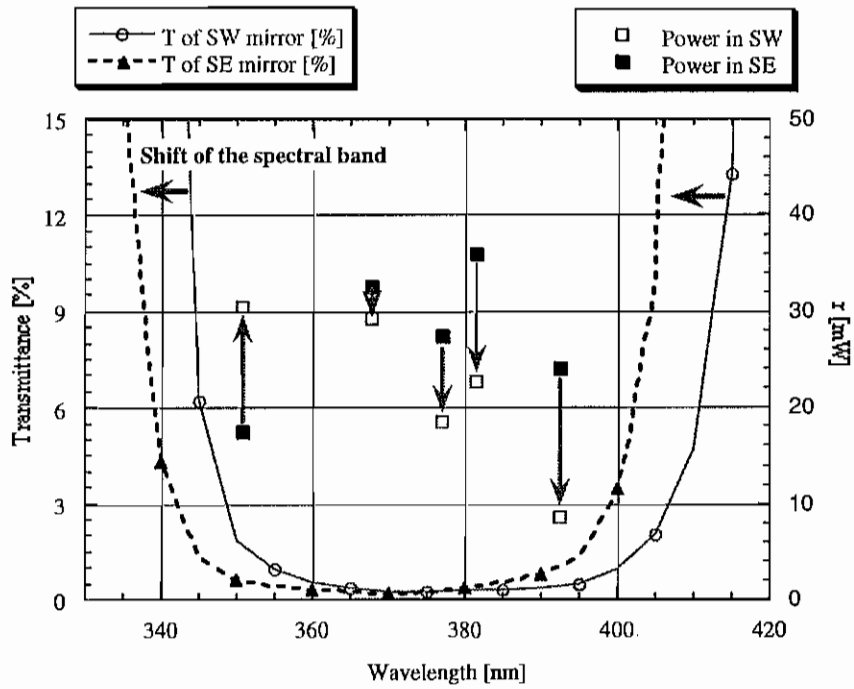

Fig. 4.3.2. Change of the spectral properties of the downstream cavity mirror due to high harmonic radiation.

We also observed a change in spectral properties due to heat generated by the high harmonic radiation of the OK-4. During four-months of operation, the bandwidth of the reflectivity of the downstream mirror gradually shifted towards

shorter wavelengths. The dependence of the outcoupling power with wavelength shows the shift of the spectrum in the downstream mirror (see Figure 4.3.2). Since the outcoupled power depends upon the transmittance of the cavity mirror, the difference between the power outcoupled to southwest (upstream) and southeast (downstream) became larger as the differences in the transmittance became larger.

Thermal effects become more crucial when the FEL is operated at the high current needed to obtain high gain and high power (especially at the short wavelengths). To avoid thermal problems, a more efficient mirror cooling system must be developed for use with the present cavity geometry or the optical cavity geometry should be modified to use a grazing incident configuration which could reduce the thermal load by a factor of $1/\cos\theta$. We will discuss this optical ring resonator in Section 4.6.

4.4 Mechanical distortions

Minimizing the mechanical stress caused by the mirror holder is crucial in a near-concentric long optical cavity like that of the Duke system. Mechanical stress can not only reduce the radius of curvature to below that of the stability threshold (for example, $R_{c,th} = 26.865$ m in the DFEL), but also distort the shape of the surface. The mirror holder is made of oxygen-free high conductivity (OFHC) copper and was designed to maximize the heat dissipation of the cavity mirror. However, the first lasing trial demonstrated that the stability of the optical cavity was extremely

sensitive to mechanical stress from the mirror holder. To allow a force free grip on the cavity mirror, finger clips were used to support the mirror from the top and not from the side. It should be stressed that even a 0.001 inches increase in the mirror diameter reduces the radius of curvature asymmetrically and causes a large elliptical optical beam profile at the cavity mirrors. The finger clip support configuration holds the cavity mirror without mechanical stresses However, the clip allows a slow drift of cavity mirror position and angle.

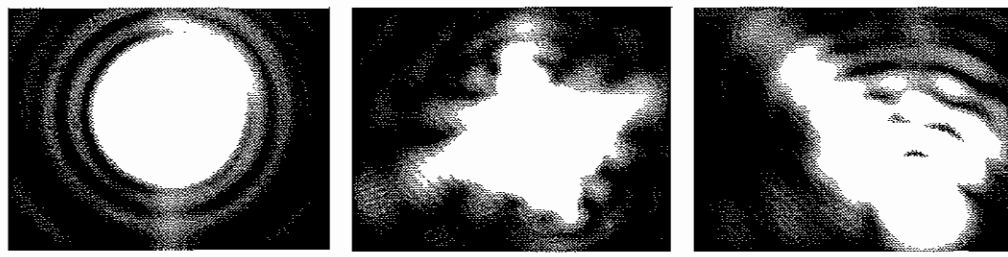

(a) $L = R_c = 27.31$ m (b) $L = R_c = 26.71$ m (c) $L = 26.71$ m ($R_c < L$)

Fig. 4.4.1. Images of a 400 μm pinhole spot of the diode laser due to the mechanical stress from the copper mirror holder. (a) free holding, (b) 1/16 turn of #8-32 screw, (c) 1/4 turn of #8-32 screw.

To study the mechanical stress caused by the mirror holder, a spring-type mirror holder was designed to provide a more flexible and uniform distribution of force around the mirror circumference. As shown in Figure 4.4.1 and Figure 4.4.2, the stress on the mirror from the spring-type holder is significantly less than the previous arrangement, but vertical vibrations due to the gravitational force make it

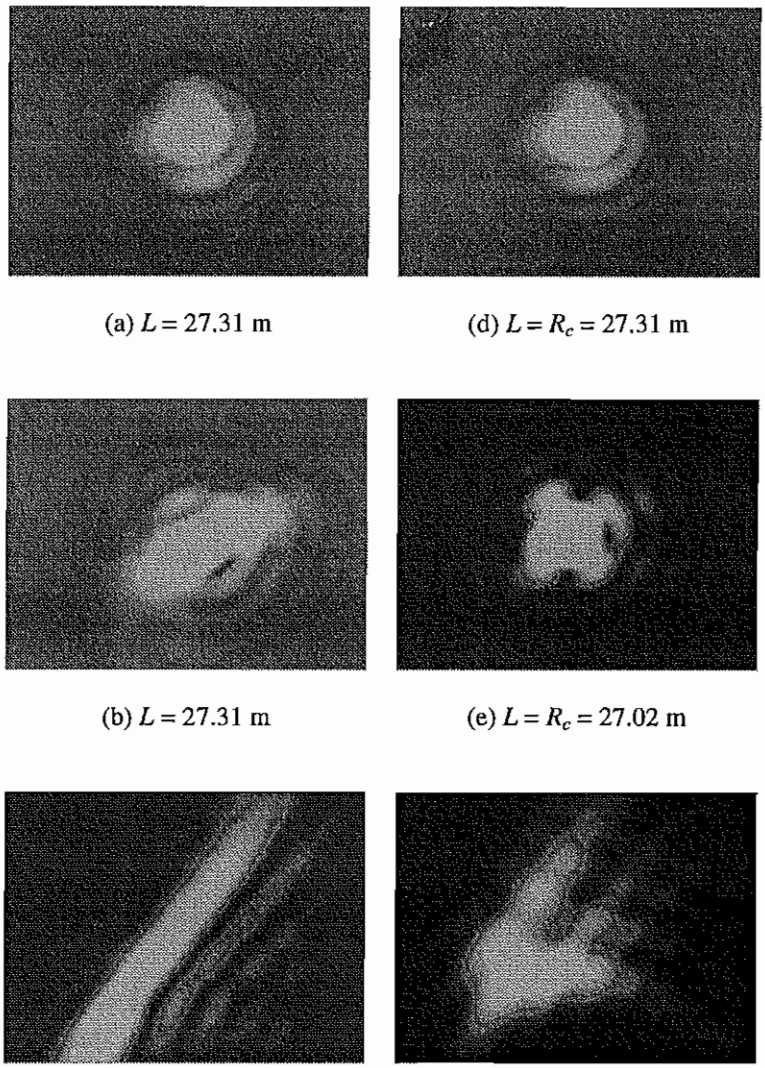

(a) $L = 27.31$ m (d) $L = R_c = 27.31$ m

(b) $L = 27.31$ m (e) $L = R_c = 27.02$ m

(c) $L = 27.31$ m (f) $L = R_c = 26.73$ m

Fig. 4.4.2. Images of a 200 μm pinhole spot of the diode laser due to the mechanical stress from the spring type mirror holder. (a) & (d) free holding, (b) & (e) 3/2 turn of #8-32 screw, (c) & (f) 2 turns of #8-32 screw. (a), (b), and (c) are images at the location of focal point of free holding, while (d), (e), and (f) are images at the focal points shifted due to the mechanical distortions.

unstable. Further, the asymmetric stress distribution due to a non-uniform contact still distorts the figure of the mirror surface. The total force applied to the mirror for the copper mirror holder is not measurable, but the total force applied by the spring-type holder can be approximately measured by using a spring washer. The total force applied is 465 N for (b) & (e) and 620 N for (c) & (f) in Figure 4.4.2. The copper mirror holder stresses the mirror more than the spring type holder even though the tightening forces are smaller. The total applied force of approximately 620 N changes the radius of curvature making the resonator unstable and further increasing cavity loss due to the distorted optical field profiles. Different types of cavity mirror holders are being investigated to solve the problem of the mirror distortion.

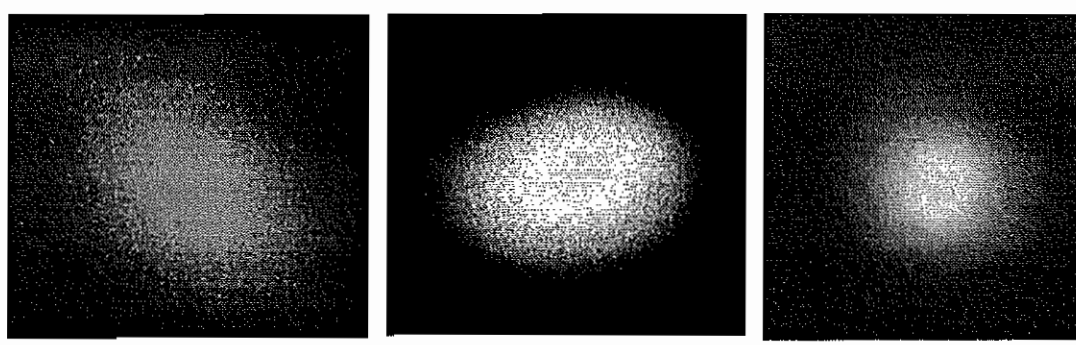

(a) (b) (c)

Fig. 4.4.3. Images of TEM_{00} modes of the FEL optical beams at the location of 1.13 m from the cavity mirror. This mirror substrate has a broadband multilayered coating (from 430 to 720 nm) and is approximately 0.001 inches larger in diameter than the other cavity mirror substrate. (a) is a beam profile before the adjustment of the mirror holder, while (b) is after the adjustment was made by slightly increasing the size of the mirror holder using the screw to freely fit the mirror into the holder. (c) is a typical TEM_{00} mode of FEL with no mechanical distortion taken at 370 nm.

In the initial lasing (without changing the mirror holder size) using the broadband mirror, the optical beam profile was larger than expected and was of elliptical shape instead of the expected symmetrical TEM_{00} Gaussian mode. At the southwest (upstream) mirror, the beam waists along the long and short axes were 10.18 mm and 6.65 mm, causing Rayleigh ranges of 0.85 m and 1.96 m. Further, the focal points were also shifted downstream by 1.83 m and 1.56 m. The cavity loss was also higher than expected from previous data on the transmittance of these mirrors. In γ-ray mode, the flux of the γ rays was smaller than expected because of the unstable optical cavity, low power of the laser, and low optical density at the collision point. Nevertheless, we were able to lase in wavelengths in the range from 430 nm to 720 nm due to reasonably high gain. Before the second operation, the mirror holder size was slightly increased using the screw. The optical beam shape was still elliptical and the long axis of the ellipse was rotated to the horizontal direction instead of to 45°, indicating that the mirror holder needed more adjustment to avoid mechanical distortion. However, we note that the beam size was reduced and the FEL performance was improved. Figure 4.4.3(c) shows the typical round-shape of TEM_{00} Gaussian mode of the optical beam taken at 370 nm having a waist of 3.73 mm (Rayleigh range of 3.36 m) at the same location where the size of the optical beam (a) was measured.

4.5. Optical cavity mirrors

As indicated earlier, each cavity mirror in the Duke/OK-4 SR FEL has a diameter of 50 ± 0.02 mm, a thickness of ~ 11 ± 0.5 mm, and a radius of curvature of 27.27 ± 0.05 m. Because of the limited availability of materials for VUV optics, the choice of the mirror substrate and the coating material is critical to FEL operation in the VUV range.

Materials capable of an extremely smooth surface finish are required for mirror substrates to reduce scattering losses. As shown in Fig. 4.5.1, the scattering loss can be critical at short wavelengths. As mentioned in the previous sections, substrates need to have low thermal expansion coefficients to reduce the distortion of the mirror surface due to high power loads from high harmonic radiation. Substrate materials should also have a high thermal conductivity to quickly dissipate a thermal load. Further, the substrate should have a small mass and high stiffness with low mass to reduce the mechanical distortion. Under these conditions, silicon crystal is the best choice, but is good only for metallic coatings because of its non-transparency. UV grade fused silica is chosen for a mirror substrate in the Duke/OK-4 because it can be polished to a super-smooth surface with a surface roughness of approximately 2 Å and is transparent down to 180 nm. This transparency makes it possible to extract the FEL light through the cavity mirrors to align the mirrors precisely. Below 180 nm the transmittance of fused silica drops rapidly; so we use CaF_2 or MgF_2 for the mirror substrates in this regime. Even though surface finishing

of CaF_2 or MgF_2 mirror substrates is not as good as for fused silica, these materials are transparent down to 140 nm and 120 nm, respectively.

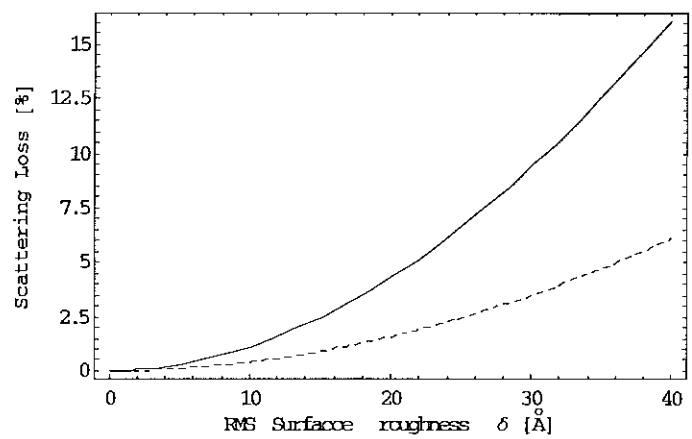

Fig. 4.5.1. Dependence of the scattering loss on the surface roughness.
The solid curve is for 120 nm light and the dashed curve is for 200 nm light.

Multilayer dielectric coated mirrors are used to achieve high reflectivity. The advantage of a dielectric coating is higher reflectivity but at the expense of a narrower bandwidth. The choice of the dielectric coating material for the VUV range is challenging. Above 240 nm, HfO_2/SiO_2 with HfO_2 as the top layer gives high reflectance and high radiation resistance. Mirror degradation due to high harmonic radiation was less than 1% during several months of operations (cavity mirrors with 226 – 256 nm spectral bandwidth and 365 – 412 nm spectral bandwidth). Because of the high absorption of HfO_2, MgF_2 is used as a low index material and Al_2O_3 as a

high index material below 220 nm. Al_2O_3/MgF_2 provides high reflectivity (greater than 96 – 99%) down to approximately 180 nm. However, it is too sensitive to radiation. Al_2O_3/MgF_2 coated mirrors used at the central wavelengths of 220 nm and 195 nm were rapidly degraded causing an increase in the cavity losses of approximately 20% in a week for 220 nm and in several hours for 195 nm. The first two attempts to lase at 193 nm failed because of high cavity loss of the cavity mirrors. Successful lasing at 212 nm in NIJI-IV demonstrated the high radiation resistance of Al_2O_3. However, a Al_2O_3/SiO_2 multilayer coating does not provide high reflectance below 200 nm. After consulting with GSI Lumonics in Canada (the vendor fabricating our cavity mirrors), the cavity mirrors were coated with Al_2O_3/SiO_2 multilayers on top of the original Al_2O_3/MgF_2 multilayers. The cavity loss in these mirrors was around 4%, which was much lower than previously observed. Further, the mirror degradation was also smaller, resulting in an approximately 5% cavity loss after a 2 week run. With these mirrors the Duke/OK-4 lased at 193.7 nm. Measuring mirror degradation due to radiation damage with different combinations of dielectric coating materials will be an extremely worthwhile future investigation.

4.6. Future plans for the optical cavity

A conventional optical cavity uses normal incidence reflection from the cavity mirrors. Multilayer dielectric mirrors provide high reflectivity with an

increasing number of the layers, but the larger number of layers dramatically decreases the bandwidth. At short wavelengths, it is difficult to find appropriate materials with high reflectivity and high radiation resistance. The optical ring resonator using multifaceted mirrors was proposed by B.E. Newnam [Newnam 1985, 1988]. This design results in high net reflectance of multiple mirrors using total external reflection (especially below 100 nm). The advantages of using a multifaceted ring resonator are the substantial reduction of the power load on the first downstream mirror and the broad tuning range of the FEL. The main disadvantages are difficulties in alignment and optical mode matching turn by turn. An optical ring resonator was conceptually designed for the Duke/OK-4 and its stability was investigated with respect to angular misalignments [Park 1996].

To synchronize with an electron beam circulating in the storage ring, the total path of the optical beam must be a simple fraction of the circumference of the storage ring, as mentioned in the section 4.1. For the Duke/OK-4, the total path length of the optical beam should be the same as the circumference (due to the long straight section), resulting in a length of 53 m and a height of 1.2 m as is shown in Figure 4.6.1. While the electron beam travels around a horizontal racetrack-shaped storage ring, the optical beam travels around a vertical racetrack-shaped optical ring because s-polarized optical fields have a high reflectivity compared to the p-polarized ones [refer to Born 1980]. The number of cavity mirrors as well as the incidence angles of the mirrors are chosen to optimize the net reflectance. The net reflectance decreases as the number of mirrors increases or as the incident angle

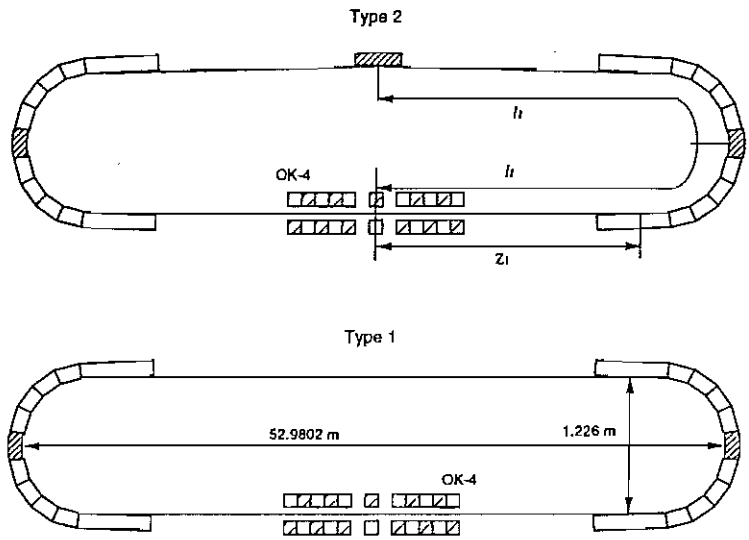

Fig. 4.6.1 Layout of optical ring resonators.
(▨:ellipsoidal mirrors; □: flat mirrors)

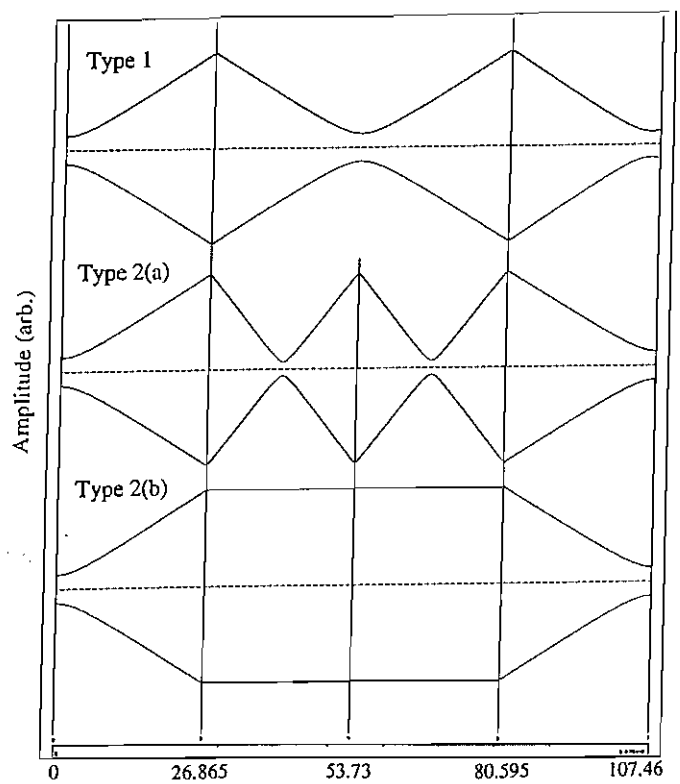

Fig. 4.6.2 Optical beam propagation in the ring resonator.

decreases. To keep the incident angles on each mirrors greater than 80° (corresponding to a reflectivity of greater than 98.5% per mirror at 80 nm), at least 22 mirrors are required, 2 focusing and 20 flat mirrors.

Figure 4.6.2 shows the optical beam in the ring resonator for different designs. Figure 4.6.3 shows the net reflectivity of the 22 mirrors with respect to the reflectivity of a single mirror. We compared the stabilities of the two designs: one has two identical focusing mirrors (Type 1) and the other has three mirrors (Type 2: two mirrors are identical and the last at the center has a different focal length). We assumed that the focusing mirrors are ellipsoidal so as to reduce astigmatism and spherical aberrations.

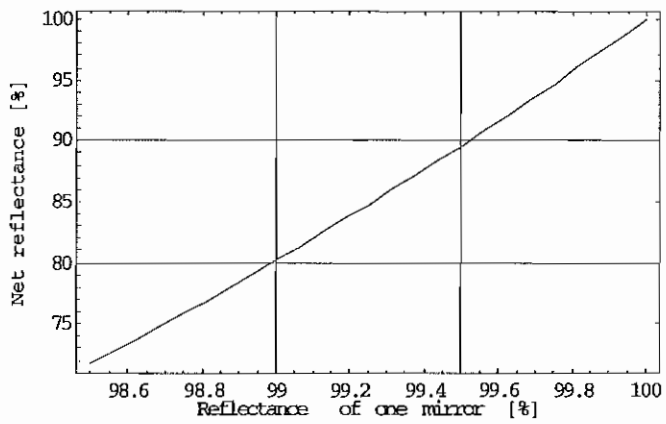

Fig. 4.6.3. The net reflectivity of 22 mirrors vs. the reflectivity of a single mirror.

Under a thin lens approximation, the ray-transfer matrix M of the ring resonator is

$$\mathbf{M}=\begin{bmatrix} a & b \\ c & d \end{bmatrix}=\begin{cases} \mathbf{M}_{l_1}\mathbf{M}_{R_1}\mathbf{M}_{l}\mathbf{M}_{R_1}\mathbf{M}_{l_1} & \text{, for Type 1} \\ \mathbf{M}_{l_1}\mathbf{M}_{R_1}\mathbf{M}_{l_2}\mathbf{M}_{R_2}\mathbf{M}_{l_2}\mathbf{M}_{R_1}\mathbf{M}_{l_1} & \text{, for Type 2} \end{cases}, \tag{4.6.1}$$

where the subscript l_i indicates a drift space and R_i indicates a focusing mirror with radius curvature of R_i. The position and angle after n turns can be written as:

$$\begin{pmatrix} x_n \\ x_n' \end{pmatrix}=\mathbf{M}^n\begin{pmatrix} x_0 \\ x_0' \end{pmatrix}. \tag{4.6.2}$$

To be stable, $x_n = x_0$ and $x_n' = x_0'$. The stability parameter g is given by

$$g^2=\sin^2(\mu/2)=\frac{1}{2}\left(1-\frac{1}{2}(a+d)\right). \tag{4.6.3}$$

The optical cavity is most stable for $\mu = (2m+1)\pi$ and most unstable for $\mu = 2m\pi$ (m: integer). Assuming that only the first flat mirror (located at $z = z_1$) is misaligned by an amount $\Delta\theta$, the new closed orbit should satisfy

$$\begin{pmatrix} x \\ x' \end{pmatrix}=\mathbf{M}\begin{pmatrix} x \\ x' \end{pmatrix}+\mathbf{R}_{\Delta\theta}\text{, where } \mathbf{R}_{\Delta\theta}=\mathbf{M}\begin{pmatrix} 1 & -z_1 \\ 0 & 1 \end{pmatrix}\begin{pmatrix} 0 \\ \Delta\theta \end{pmatrix}. \tag{4.6.4}$$

The solution of the new closed orbit is

$$\begin{pmatrix} x \\ x' \end{pmatrix}=\frac{\Delta\theta}{4g^2}\begin{pmatrix} 2b-2(a-1)z_1 \\ d-1-cz_1 \end{pmatrix}. \tag{4.6.5}$$

As summarized in Table 4.6.1, the Type 2 ring resonator is more stable than Type 1. There exist two different configurations in Type 2. For the Type 2 (a), the optical cavity has shorter focal lengths for the focusing mirrors and, therefore, is easier to fabricate. With a 5 μradian angular error, changes in x' for the Type 1

resonator are 20 times larger than for the Type 2 resonators, while the change in x is almost the same. Because of the shallow angle on the mirrors, the acceptable opening size is limited and the stability is quite sensitive to angular misalignments. Also, it is hard to match the optical beam mode and the electron beam. Another obstacle is the fabrication and polishing of the ellipsoidal mirrors. As part of a practical design effort, we will study the instabilities and the optical wave-front errors for combinations of cylindrical mirrors. Cylindrical mirrors are relatively easy to make but are subject to high spherical aberration errors.

Parameter	Type 1	Type 2(a)	Type 2(b)
β_0 [m]	4.0	4.0	4.0
ω_0 [mm]	0.32	0.319	0.32
β_1 [m]		0.984	183.45
ω_{10} [mm]		0.158	2.161
$f_1 = f_2$ [m]	13.73	9.05	27.16
f_3 [m]		6.75	1259.4
$\lvert g\rvert = \lvert\sin(\mu/2)\rvert$	0.29	0.96	0.999
For an angular tilt of $\Delta\theta = 5$ μrad of first downstream mirror			
x [μm]	62.8	134.5	128.5
x′ [μrad]	- 110.5	4.72	4.95

Table 4.6.1. Parameters for the design of the optical ring resonators and the new closed orbit due to angular misalignment of the first downstream flat mirror tilted by $\Delta\theta$. ω_0 & ω_{10} are the waists at the center of the OK-4 and between two focusing mirrors. β_0 & β_1 are the Rayleigh range at the center of the OK-4 and between two focusing mirrors. f_1 & f_2 are focal lengths of the first and second focusing mirror. μ is the phase advance of the transverse oscillations of the optical beam.

For a ring resonator, we would use Al coating on silicon crystal. The overall net reflectance of the design of the ring resonator can be calculated using optical constants measured by D.Y. Smith *et. al.* [Smith 1985] and D.F. Edwards [Edwards 1985]. The reflectance is approximately 75.6% at 80 nm and 80% at 200 nm. M.L. Scott *et. al.* [Scott 1988] measured the net reflectance of a nine-facet aluminum mirror at 58.4 nm to be 89 ± 3%, which agrees well with our calculated value. As mentioned above, the main advantage of a multi-facet ring resonator with metallic mirrors is that the tunable spectral range is broad. With aluminum mirrors, we can tune the FEL wavelength from VUV to IR range without changing the cavity mirrors. Secondly, we can achieve high reflectivity below 150 nm, where we do not have mirrors with good reflectivity at normal incidence. Third, the thermal effects on the cavity mirrors can be reduced by a factor of $1/\cos\theta$. While the reflectivity at wavelengths above 150 nm become smaller than that of dielectric mirrors, the radiation damage is much less than in dielectric mirrors. However, the mirror alignment and control/feedback system will become much more complicated.

A switching multiple mirror mount and control/feedback system is under development. This system will provide different spectral ranges to different users without spending 2 to 3 days changing the cavity mirrors. At least one day is needed for exchanging both cavity mirrors and 1 to 2 days of pumping time to reach a 10^{-10} torr vacuum.

Chapter 5

γ-ray Generation via Compton Backscattering

5.1 Introduction

Compton backscattering of laser light from a relativistic electron beam was first proposed as a method of generating quasi-monochromatic, polarized photons in 1963 [Milburn 1963, Arutyunian 1963]. Since then various techniques and applications of Compton backscattering have been proposed such as x-ray and γ-ray sources, γ-γ colliders, and electron beam diagnostics. In the earlier days, the backscattering was achieved using an electron beam from a linac and a photon beam from a conventional laser. Unfortunately, the flux of γ rays produced was not large enough to study various aspects of nuclear physics involving weak interactions and nuclear astrophysics. In order to increase the γ-ray flux, one needs large electron beam currents, high peak photon flux, and overlap between the two beams. Fortunately, the development of storage rings and free electron lasers opened new schemes for γ-ray generation. The storage ring can capture more current (typically from ~ 100 mA to ~ A) with a low emittance. Several facilities have produced γ rays using the existing storage rings and external lasers. However, the flux and the

tunability of the γ rays are limited by the external laser. As storage ring FELs with high peak intracavity power and good tunability were developed, it became possible to utilize this tunable high intracavity power. In addition, the electron beam and the photon beam for Compton backscattering in a storage ring FEL are well synchronized in time and aligned in position and angle when the FEL is optimized. SR FEL based γ-ray generation consists of two electron bunches separated by half of the ring circumference (for example, 53.73 m or 179.1 nsec at Duke). γ rays are generated via Compton backscattering of one electron bunch with the optical bunch produced by the second electron bunch. Theoretically, more electron bunch pairs can be stored in the FEL and used for γ-ray generation to increase the flux, however, the lasing condition becomes critically sensitive to instabilities in the electron bunches contained within the RF cavity. In the OK-4/Duke SR FEL, γ rays are generated using up to four electron bunches.

The production of γ rays using a SR FEL has been achieved at the Duke/OK-4 [Litvinenko 1997, Park 1999], UVSOR [Hosaka 1997], NIJI-4 [Ohgaki 1997], and Super-ACO [Nutarelli 1998]. The flux is typically $10^5 - 10^7$ γ's/sec and the energy resolution is ~ 0.5 % – 5 % depending on the facility and energy of the γ rays.

5.2 Compton backscattering: Theory

Compton scattering is the scattering of a photon with 4-momentum $k = (\omega/c, \vec{\mathbf{k}})$ by a free electron with 4-momentum $p = (E_e/c, \vec{\mathbf{p}})$ and results in a

scattered photon and electron with the frequency shifted. In the language of quantum electrodynamics an incoming photon with 4-momentum k is absorbed by a free electron with 4-momentum p and an outgoing photon with 4-momentum k' ($k' = (\omega'/c, \vec{\mathbf{k}}')$) is emitted. The Compton process differs from bremsstrahlung (which is a popular process used for x-ray or γ-ray generation) by the fact that an incoming real photon instead of the virtual photon interacts with a recoiling charged particle and is of second order (satisfying the energy conservation). For ultra-relativistic incoming electrons, most of the outgoing photons are scattered backward within an angle of approximately $1/\gamma$ (hence, the process is called Compton backscattering) and are well collimated compared to bremsstrahlung.

5.2.1. Energy of scattered photons

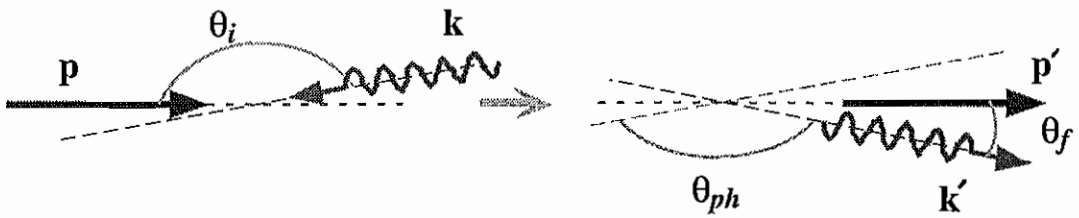

Fig. 5.2.1 Schematic picture of the process of Compton backscattering.
(left: Before scattering; right: After scattering)

Kinematics of the scattering of laser light by relativistic electrons can be derived using the conservation of four-momentum. As shown in Figure 5.2.1, the

Compton scattering process results in a scattered photon with $k' = (\omega'/c, \vec{\mathbf{k}}')$ and an electron with $p' = (E_e'/c, \vec{\mathbf{p}}')$. From the 4-momentum conservation law,

$$p + \hbar k = p' + \hbar k', \tag{5.2.1}$$

the energy of the scattered photon is

$$\hbar\omega' = \hbar\omega \frac{1 - \beta\cos\theta_i}{1 - \beta\cos\theta_f + \frac{\hbar\omega}{E_e}\left(1 - \cos\theta_{ph}\right)}, \tag{5.2.2}$$

where $\hat{p}\cdot\hat{k} = \cos\theta_i$, $\hat{p}\cdot\hat{k}' = \cos\theta_f$, and $\hat{k}\cdot\hat{k}' = \cos\theta_{ph}$. In spherical coordinates, (i.e., $\vec{\mathbf{k}} = (k,\theta,\varphi)$, $\vec{\mathbf{k}}' = (k',\theta',\varphi')$, and $\vec{\mathbf{p}} = (p,\theta_e,\varphi_e)$), the angles are rewritten as

$$\cos\theta_i = \cos\theta_e\cos\theta + \sin\theta_e\sin\theta\cos(\varphi_e - \varphi),$$

$$\cos\theta_f = \cos\theta_e\cos\theta' + \sin\theta_e\sin\theta'\cos(\varphi_e - \varphi'),$$

$$\cos\theta_{ph} = \cos\theta\cos\theta' + \sin\theta\sin\theta'\cos(\varphi - \varphi').$$

In an ultra-relativistic case, θ_e and θ' are approximately zero and θ is approximately π at the collision point (the focal point of the paraxial wave). By re-defining θ as $\pi - \theta$ and $\theta << 1$,

$$\cos\theta_i \approx -1 + \frac{1}{2}\theta_e^2 + \frac{1}{2}\theta^2 + \theta_e\theta\cos(\varphi_e - \varphi),$$

$$\cos\theta_f \approx 1 - \frac{1}{2}\theta_e^2 - \frac{1}{2}\theta'^2 + \theta_e\theta'\cos(\varphi_e - \varphi'),$$

$$\cos\theta_{ph} \approx -1 + \frac{1}{2}\theta^2 + \frac{1}{2}\theta'^2 + \theta\theta'\cos(\varphi - \varphi').$$

For head-on collisions, $\theta_i = \pi$ and $\theta_{ph} = \pi - \theta_\beta$ and so the energy becomes

$$\hbar\omega'\big|_{\theta_i=\pi} = \hbar\omega \frac{1+\beta}{1-\beta\cos\theta_f + \frac{\hbar\omega}{E_e}\left(1+\cos\theta_f\right)}. \tag{5.2.3}$$

Equation 5.2.3 has a maximum value at $\theta_f = 0$. For ultra-relativistic electrons, the peak energy produced via Compton backscattering is

$$E_{\gamma,\max} \approx 4\gamma^2\hbar\omega \Big/ \left(1+\frac{4\gamma^2\hbar\omega}{E_e}\right) \tag{5.2.4}$$

because $1-\beta \approx 1/2\gamma^2$ and $1+\beta \approx 2$. When the photon energy $\hbar\omega$ is much smaller than $E_e/4\gamma^2$, the maximum γ-ray energy $E_{\gamma,\max}$ is approximately $4\gamma^2\hbar\omega$. Figure 5.2.2 shows the dependence of the peak γ-ray energy on the energies of photons and electrons prior to scattering.

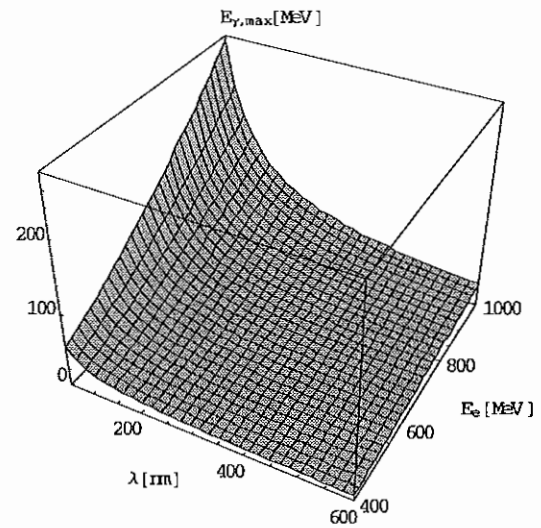

Fig. 5.2.2. Dependence of the peak γ-ray energy on the energies of photons and electrons prior to collision.

5.2.2. Scattering cross section and polarization effects

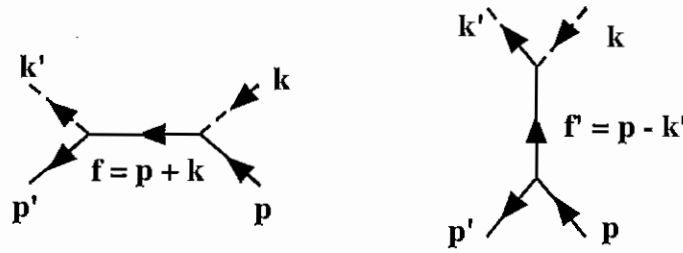

Fig. 5.2.3. Feynman diagrams for Compton scattering.

Compton scattering is a second-order process in covariant perturbation theory of the relativistic quantum theory. The corresponding S-matrix [Sakurai 1967] is

$$S_{fi} = e^2 \int d^4x_1 \int_{t_2<t_1} d^4x_2 \langle k'p' | \overline{\psi}(x_1)\gamma_\mu \psi(x_1) A_\mu(x_1) \overline{\psi}(x_2)\gamma_\nu \psi(x_2) A_\nu(x_2) | kp \rangle, \quad (5.2.5)$$

where $|kp\rangle$ and $|k'p'\rangle$ represent the initial state of the photon with wave vector k and the electron with momentum p and the final state of the photon with wave vector k', and the electron with momentum p'. The process can be visualized by drawing the Feynman diagram in Figure 5.2.3. The detail calculation of the scattering cross section is contained in many textbooks [Landau 1982, Sakurai 1967] where the differential cross section for unpolarized electrons and photons is giving by

$$d\sigma = \frac{8\pi r_e^2}{m^2} \frac{dt}{x^2} \left\{ \left(\frac{1}{x} - \frac{1}{y} \right)^2 + \left(\frac{1}{x} - \frac{1}{y} \right) + \frac{1}{4} \left(\frac{x}{y} + \frac{y}{x} \right) \right\}, \quad (5.2.6)$$

where $x = (s - m^2)/m^2$ and $y = -(u - m^2)/m^2$. The variables s, t, and u are kinematical invariants defined by

$$s = (p+k)^2 = (p'+k')^2 = m^2 + 2pk = m^2 + 2p'k'$$

$$t = (p-p')^2 = (k'-k)^2 = 2(m^2 - pp') = -2kk' \qquad (5.2.7)$$

$$u = (p-k')^2 = (p'-k)^2 = m^2 - 2pk' = m^2 - 2p'k$$

$$s + t + u = 2m^2$$

for $\hbar = 1$ and c = 1. For a given energy of the electrons and photons, i.e., s = const,

$$dt = -du = m^2 dy \qquad (5.2.8)$$

and the differential cross section of unpolarized electrons and photons becomes

$$d\bar{\sigma} = 8\pi r_e^2 \frac{dy}{x^2}\left\{\left(\frac{1}{x} - \frac{1}{y}\right)^2 + \left(\frac{1}{x} - \frac{1}{y}\right) + \frac{1}{4}\left(\frac{x}{y} + \frac{y}{x}\right)\right\}. \qquad (5.2.9)$$

The total cross section can be calculated by integrating $d\bar{\sigma}$ over the range $x/(x+1) < y < x$ and by satisfying the inequalities: $s \geq m^2$, $t \leq 0$, and $us \leq m^4$. Thus, the total cross section becomes

$$\sigma_{tot} = \frac{2\pi r_e^2}{x}\left\{\left(1 - \frac{4}{x} - \frac{8}{x^2}\right)\ln(1+x) + \frac{1}{2} + \frac{8}{x} - \frac{1}{2(1+x)^2}\right\}. \qquad (5.2.10)$$

In the laboratory frame,

$$x = \frac{2\gamma\hbar\omega(1 - \beta\cos\theta_i)}{mc^2}, \qquad (5.2.11)$$

$$y = \frac{2\gamma\hbar\omega'(1 - \beta\cos\theta_f)}{mc^2}. \qquad (5.2.12)$$

For the Duke case, $x << 1$ ($\hbar\omega \sim 2$ -10 eV and $\gamma \sim 10^3$), so

$$\sigma_{tot} \approx \frac{8\pi r_e^2}{3}(1-x), \qquad (5.2.13)$$

which differs only slightly from the classical Thompson scattering cross section. Note that the total cross section decreases with increasing electron energy and photon energy.

For the scattering of polarized photons by unpolarized electrons, the scattering cross section is [Landau 1982]

$$d\sigma = \frac{d\bar{\sigma}}{2} + \frac{2r_e^2 dy d\varphi}{x^2}\left\{-(\xi_3+\xi_3')\left[\left(\frac{1}{x}-\frac{1}{y}\right)^2+\left(\frac{1}{x}-\frac{1}{y}\right)\right]+\xi_1\xi_1'\left(\frac{1}{x}-\frac{1}{y}+\frac{1}{2}\right)\right.$$

$$\left.+\frac{1}{2}\xi_2\xi_2'\left(\frac{x}{y}+\frac{y}{x}\right)\left(\frac{1}{x}-\frac{1}{y}+\frac{1}{2}\right)+\xi_3\xi_3'\left[\left(\frac{1}{x}-\frac{1}{y}\right)^2+\left(\frac{1}{x}-\frac{1}{y}\right)+\frac{1}{2}\right]\right\}, \qquad (5.2.14)$$

where φ is the azimuthal angle and $\xi=(\xi_1,\xi_2,\xi_3)$ and $\xi'=(-\xi_1',-\xi_2',\xi_3')$ are the Stokes parameters of the incoming (initial) and outgoing (final) photons. A factor ½ in Equation 5.2.14 appears because there is no summation over the polarizations of the final photon (only the final electrons).

The directions of polarization of the photons are determined by the components of the three-vectors, $(e^{(1)},e^{(2)},\hat{k})$ and $(e'^{(1)},e'^{(2)},\hat{k}')$. $e^{(1)}$ and $e'^{(1)}$ are the directions of the polarizations perpendicular to the plane of scattering and $e^{(2)}$ and $e'^{(2)}$ are the direction of polarization in the plane of the scattering. That is,

$e^{(1)}$, $e'^{(1)} \parallel \hat{k}\times\hat{k}'$,

$e^{(2)} \parallel \hat{k}\times(\hat{k}\times\hat{k}')$ and $e'^{(2)} \parallel \hat{k}'\times(\hat{k}\times\hat{k}')$.

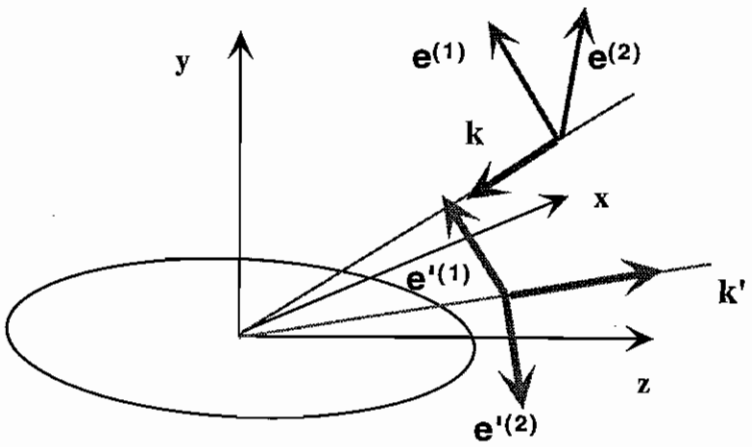

Fig. 5.2.4 Polarization vectors in Cartesian coordinates.

A change of sign $e^{(2)}$ in the photon density matrix is equivalent to a change of sign of ξ_1 and ξ_2 and therefore $\xi' = (-\xi_1', -\xi_2', \xi_3')$. The density matrices of the initial and final photons (referred to as the unit four-vectors $e^{(1)}$ and $e^{(2)}$) are

$$\rho^{(k)} = \frac{1}{2}(1+\xi\cdot\sigma) = \frac{1}{2}\begin{bmatrix} 1+\xi_3 & \xi_1 - i\xi_2 \\ \xi_1 + i\xi_2 & 1-\xi_3 \end{bmatrix}, \quad \xi_1^2 + \xi_2^2 + \xi_3^2 = 1, \qquad (5.2.15)$$

$$\rho^{(k')} = \frac{1}{2}(1+\xi'\cdot\sigma) = \frac{1}{2}\begin{bmatrix} 1+\xi_3' & -\xi_1' + i\xi_2' \\ -\xi_1' + i\xi_2' & 1-\xi_3' \end{bmatrix}, \quad \xi_1'^2 + \xi_2'^2 + \xi_3'^2 = 1, \quad (5.2.16)$$

where σ is the Pauli matrix. $\xi_3 = 1$ corresponds to the photons polarized in the direction perpendicular to the plane of scattering; $\xi_3 = -1$ corresponds to photons polarized in the direction parallel to the plane of scattering. $\xi_1 = 1$ describes 45° linear polarizations: Finally, ξ_2 characterizes circular polarizations. The quantities ξ_2 and $\sqrt{\xi_1^2 + \xi_3^2}$ are invariant under Lorentz transformation.

For incoming horizontally polarized photons, the ratio between the scattering cross sections of vertically polarized and horizontally polarized outgoing photons is described by a recoil parameter in the rest frame. For the most energetic photons scattered at $\theta_f = 0$, the ratio at $\theta = \theta_f = 0$ in head-on collisions is given by

$$\frac{d\sigma_{\perp}}{d\sigma_{\parallel}}(\theta = 0) = \frac{R^2}{(2+R)^2}, \tag{5.2.17}$$

$$R = \frac{2\gamma\hbar\omega(1+\beta)}{mc^2}.$$

Therefore for small recoil parameter R the probability of scattered photons existing with a vertical polarization becomes negligible. As an example, for the scattering of 6 eV photons by 500 MeV electrons, R = 0.046 and $d\sigma_{\perp}/d\sigma_{\parallel} \cong 5\times10^{-4}$. In the Duke/OK-4 FEL the optical beam is horizontally polarized in the xyz coordinate system, and therefore $\xi_1 = \sin2(\pi/2 + \varphi)$ and $\xi_3 = \cos2(\pi/2 + \varphi)$ for head-on collisions. Figure 5.2.5 illustrates the distributions 30 m away from the collision point of horizontally polarized and vertically polarized outgoing photons from the scattering of horizontally polarized incoming photons by unpolarized electrons.

Taking the sum over all polarizations of the outgoing photons, one arrives at the simple expression,

$$d\sigma = d\bar{\sigma} - \frac{4r_e^2 dy d\varphi}{x^2}\xi_3\left[\left(\frac{1}{x}-\frac{1}{y}\right)^2 + \left(\frac{1}{x}-\frac{1}{y}\right)\right]. \tag{5.2.18}$$

There is only one linear polarization parameter ξ_3 for the incoming photon. $\xi_3 = 0$ describes the circular polarization case, which corresponds to the scattering cross section of

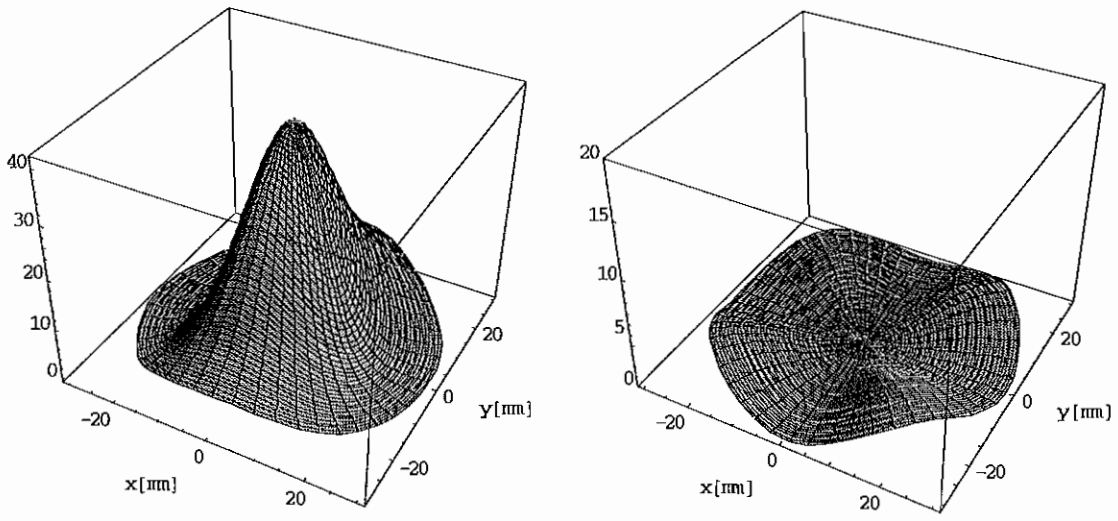

(a) (b)

Fig. 5.2.5. Distributions 30 m away from the collision point of outgoing photons scattered in a head-on collision of horizontally polarized photons of wavelength 370 nm with unpolarized electrons of 600 MeV. (a): horizontally polarized outgoing photons (b): vertically polarized outgoing photons

unpolarized electrons and photons. In case of head-on collisions, $\theta_i = \pi$ and one can reduce the variables to $\theta = \theta_f$ (the angle of the final photon in the laboratory frame). Writing dy in terms of $\sin\theta d\theta$,

$$dy = 2\left(\frac{\hbar\omega'}{mc^2}\right)^2 \sin\theta \cdot d\theta ,$$

the differential cross section in the lab frame becomes [Litvinenko 1995a]

$$\frac{d\sigma}{d\Omega} = \frac{8r_e^2}{x^2}\left\{(1-\xi_3)\left[\left(\frac{1}{x}-\frac{1}{y}\right)^2+\left(\frac{1}{x}-\frac{1}{y}\right)\right]+\frac{1}{4}\left(\frac{x}{y}+\frac{y}{x}\right)\right\}\left(\frac{\hbar\omega'(\theta)}{mc^2}\right)^2, \quad (5.2.19)$$

where

$$x=\frac{2\gamma\hbar\omega(1+\beta)}{mc^2},\quad y=\frac{2\gamma\hbar\omega(1-\beta\cos\theta)}{mc^2}\frac{(1+\beta)}{(1-\beta\cos\theta+(1+\cos\theta)\hbar\omega/\gamma mc^2)}.$$

The total distribution averaged over outgoing photon polarizations is azimuthally symmetric for circularly polarized incoming photons, whereas linearly polarized incoming photons result in azimuthal modulations of the averaged distribution. Figure 5.2.6 shows the density distributions of γ rays and their contour plots for circularly and linearly polarized incoming photons 30 m away from the collision point. For linearly polarized incoming photons, one observes a nodal point at $\theta \sim 1/\gamma$ (for an energy of 1 GeV and for l = 30 m, $l/\gamma \sim$ 15.3 mm), as expected for ultra-relativistic cases. The distribution for high energy electrons is narrower than that for lower energy electrons.

The energy of the scattered photons (as shown in Equation 5.2.2) is independent of the azimuthal angle φ. The cross section integrated over φ can be expressed in terms of the scattered photon energy $E_\gamma (= \hbar\omega')$. By introducing the ratio $\rho = \hbar\omega'/\hbar\omega'_{\max}$, one can derive the energy dependence of the scattering cross section,

$$d\sigma(x,y) \equiv f(x,y)dy = f(x,\rho)d\rho \equiv d\sigma_{en}(x,\rho). \qquad (5.2.20)$$

We define the g function $g(x, \rho)$, which is the partition function for outgoing photons scattered with energy $(E_\gamma, E_\gamma + \mathrm{d}E_\gamma)$, as [Litvinenko 1995a]

$$g(x,\rho)d\rho \equiv \frac{d\sigma_{en}(x,\rho)}{\int d\sigma_{en}(x,\rho)}. \qquad (5.2.21)$$

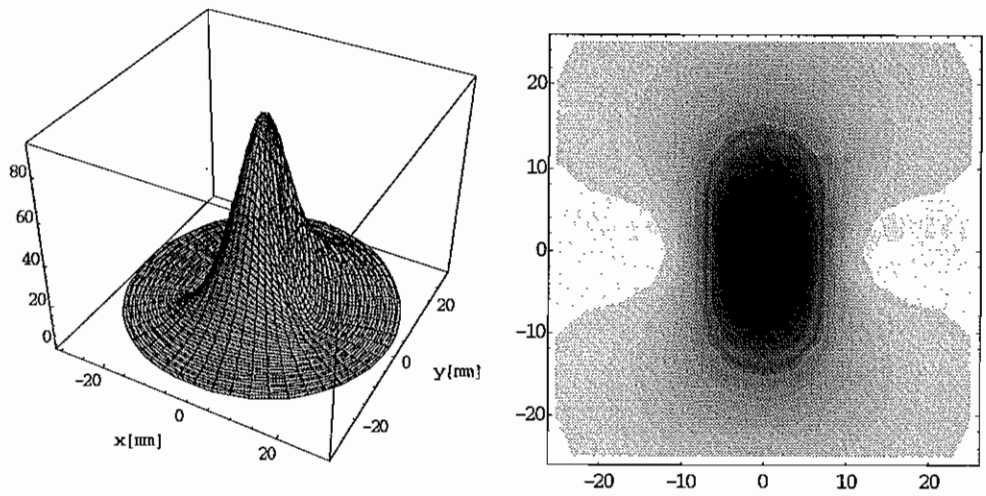

(a) Linearly polarized incoming photons

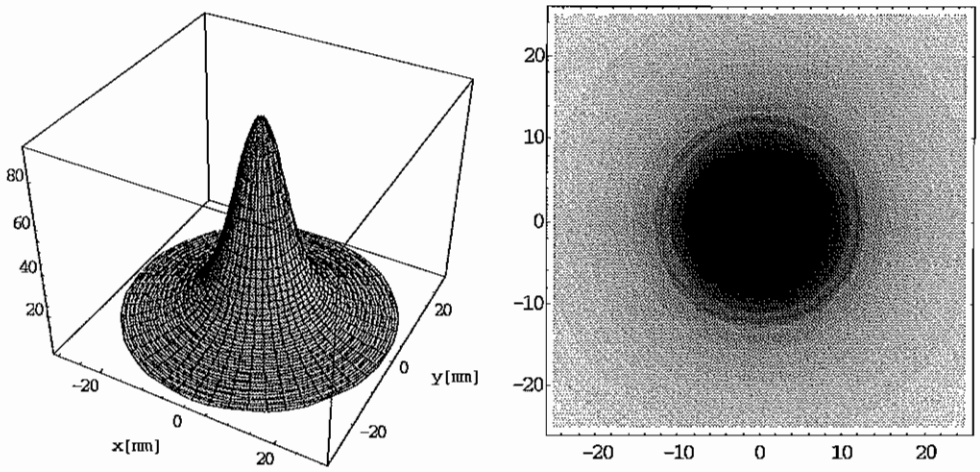

(b) Circularly polarized incoming photons

Fig. 5.2.6. The distributions of γ rays for circularly and linearly polarized incoming photons at the location 30 m from the collision point. (a): linearly polarized incoming photons of wavelength 120 nm and unpolarized electrons of energy 1 GeV; (b): circularly polarized incoming photons of wavelength 120 nm and unpolarized electrons of energy 1 GeV)

Then, it follows that,

$$g(x,\rho)=\frac{8\pi r_e^2}{\sigma_{tot}x^2}\left\{\left(\frac{1}{x}-\frac{1}{y}\right)^2+\left(\frac{1}{x}-\frac{1}{y}\right)+\frac{1}{4}\left(\frac{x}{y}+\frac{y}{x}\right)\right\}\frac{x^2(1+\beta)}{2(1+x)}d\rho\,, \qquad (5.2.22)$$

$$y=x\frac{\gamma\beta mc^2-\hbar\omega'}{\gamma\beta mc^2-\hbar\omega}=\frac{x}{2(1+x)}\frac{2\beta(1+x)-(1+\beta)x\rho}{\beta-r}\,,\ r=\hbar\omega/\gamma mc^2,$$

which satisfies

$$\int_{(1+x)/\gamma^2(1+\beta)^2}^{1} g(x,\rho)d\rho=1\,, \quad (\because \frac{x}{1+x}<y<x \Leftrightarrow 0<\frac{1+x}{\gamma^2(1+\beta)^2}<\rho<1),$$

where the expressions for x and σ_{tot} are given in Equation 5.2.19 and Equation 5.2.10. When the recoil R (or x) is small, $g(x, \rho)$ has a maximum of 1.5 at the peak energy. As the recoil increases, $g(x, \rho)$ increases at high energies and decreases at low energies. The number of scattered photons within energy (E_γ, $E_\gamma + \Delta E_\gamma$) is given by

$$\Delta N = N_{tot}\, g(x,\rho)\Delta\rho\,. \qquad (5.2.23)$$

With a 3 mm diameter collimator at a location 30 m from the collision point, the acceptance angle is approximately 10^{-4} radian. For a 600 MeV electron beam and a 370 nm wavelength optical beam, the partition function g is between 1.46 and 1.5 with an energy resolution of 1.3 %. The desired energy resolution can be achieved by selecting the appropriate collimator diameters.

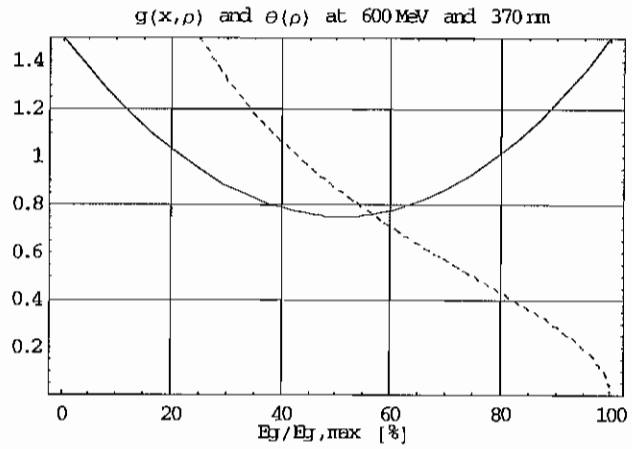

Fig. 5.2.7. The energy distribution function $g(x, \rho)$ (solid curve) and its observation angle $\theta(\rho)$ (dashed curve) for 600 MeV initial electrons and 370 nm incoming photons. ($\theta(\rho)$ in 10^{-3} radian.)

5.2.3. The flux of scattered photons

The number of collisions between particles in the volume dV in time dt in an arbitrary reference frame is defined as [Landau 1975]

$$d\nu = \sigma\sqrt{(\vec{\mathbf{v}}_1 - \vec{\mathbf{v}}_2)^2 - (\vec{\mathbf{v}}_1 \times \vec{\mathbf{v}}_2)^2}\, c \cdot n_1 n_2 dV dt\,, \tag{5.2.24}$$

where σ is the scattering cross section, n_1 and n_2 are particle densities, and $\vec{\mathbf{v}}_1$ and $\vec{\mathbf{v}}_2$ are dimensionless velocities of the particles. In Compton scattering, $\vec{\mathbf{v}}_1 = \beta\hat{p}$, $\vec{\mathbf{v}}_2 = \hat{k}$, and $\hat{p} \cdot \hat{k} = \cos\theta_i$. Therefore,

$$d\nu = \sigma\left|1 - \beta\cos\theta_i\right| c \cdot n_1 n_2 dV dt\,, \tag{5.2.25}$$

where $\sigma \equiv \sigma(\vec{\mathbf{p}}, \vec{\mathbf{k}})$ is the scattering cross section derived in Section 5.2.2.

Now, we consider electron beams and photon beams having finite distributions in phase space. $f_e(\vec{\mathbf{r}},\vec{\mathbf{p}},t)$ and $f_{ph}(\vec{\mathbf{r}},\vec{\mathbf{k}},t)$ denote the normalized distribution functions of electrons and photons in the phase space. The densities of incoming electrons and photons are given by

$$n_e = N_e f_e(\vec{\mathbf{r}},\vec{\mathbf{p}},t)dp^3, \tag{5.2.26}$$

$$n_{ph} = N_{ph} f_{ph}(\vec{\mathbf{r}},\vec{\mathbf{k}},t)dk^3, \tag{5.2.27}$$

where N_e and N_{ph} are the total number of electrons and photons in each bunch. The total number of scattered photons per collision between the electron and photon bunch is governed by

$$\nu_b = N_e N_{ph} c \int\int\int\int dp^3 dk^3 dV dt\, \sigma(\vec{\mathbf{p}},\vec{\mathbf{k}})|1-\beta\cos\theta_i| f_e(\vec{\mathbf{r}},\vec{\mathbf{p}},t) f_{ph}(\vec{\mathbf{r}},\vec{\mathbf{k}},t). \tag{5.2.28}$$

If the collisions occur periodically with frequency f_c, the total flux of scattered photons becomes

$$\dot{N} = f_c \nu_b. \tag{5.2.29}$$

According to Equation 5.2.10 for arbitrary incoming electron and photon energies, the total scattering cross section does not depend on the spatial coordinates. Therefore, when the distribution functions satisfy $f_e(\vec{\mathbf{r}},\vec{\mathbf{p}},t) = f_e(\vec{\mathbf{r}},t) f_e(\vec{\mathbf{p}})$ and $f_{ph}(\vec{\mathbf{r}},\vec{\mathbf{k}},t) = f_{ph}(\vec{\mathbf{r}},t) f_{ph}(\vec{\mathbf{k}})$, Equation 5.2.28 can be reduced to the following:

$$\nu_b = N_e N_{ph} \int\int dp^3 dk^3 f_e(\vec{\mathbf{p}}) f_{ph}(\vec{\mathbf{k}}) \frac{\sigma_{tot}(\vec{\mathbf{p}},\vec{\mathbf{k}})}{A(\vec{\mathbf{p}},\vec{\mathbf{k}})}, \tag{5.2.30}$$

where

$$A(\vec{\mathbf{p}},\vec{\mathbf{k}}) = \left(c\left|1-\beta\cos\theta_i\right|\iint dVdtf_e(\vec{\mathbf{r}},t)f_{ph}(\vec{\mathbf{r}},t)\right)^{-1}. \qquad (5.2.31)$$

$A(\vec{\mathbf{p}},\vec{\mathbf{k}})$ is the effective area containing particles of $(\vec{\mathbf{p}},\vec{\mathbf{k}})$.

We assume that the electron beams and the photon beams have Gaussian distributions, which proves to be a good approximation for the paraxial beams. Then the distribution functions can be written as:

$$f_e(\vec{\mathbf{r}},\vec{\mathbf{p}},t) = \frac{1}{(2\pi)^3\varepsilon_x\varepsilon_y\sigma_p\sigma_l}\exp\left[-\frac{(\gamma_x x^2+2\alpha_x xx'+\beta_x x'^2)}{2\varepsilon_x}-\frac{(\gamma_y y^2+2\alpha_y yy'+\beta_y y'^2)}{2\varepsilon_y}\right.$$

$$\left.-\frac{(p_z-p_0)^2}{2\sigma_p^2}-\frac{(z-ct)^2}{2\sigma_l^2}\right] \qquad (5.2.32)$$

$$\gamma_{x,y} = \frac{1+\alpha_{x,y}{}^2}{\beta_{x,y}}, \quad \alpha_{x,y} = -\frac{1}{2}\beta'_{x,y} \qquad (\alpha_{x,y},\ \beta_{x,y}, \text{ and } \gamma_{x,y} : \text{Twiss parameters})$$

$$\sigma_{x,y} = \sqrt{\varepsilon_{x,y}\beta_{x,y}}, \quad \sigma_{x',y'} = \sqrt{\varepsilon_{x,y}\gamma_{x,y}}$$

$$f_{ph}(\vec{\mathbf{r}},\vec{\mathbf{k}},t) = \frac{k^2}{(2\pi)^3\sigma_k\sigma_z}\exp\left[-\frac{k}{\beta_0}\left((x-\vartheta_x z)^2+(\beta_0\vartheta_x)^2+(y-\vartheta_y z)^2+(\beta_0\vartheta_y)^2\right)\right.$$

$$\left.-\frac{(k-k_0)^2}{2\sigma_k^2}-\frac{(z+ct)^2}{2\sigma_z^2}\right] \qquad (5.2.33)$$

$$\vec{\mathbf{k}} = k(\vartheta_x\hat{x}+\vartheta_y\hat{y}+\hat{z}),$$

where $\varepsilon_{x,y}$ are the transverse emittances of the electron beam, $\beta_{x,y}$ are the transverse beta functions at z = 0, and σ_p and σ_l are the momentum spread and the bunch length of the electron beam. β_0 is the Rayleigh range and σ_k and σ_z are the dispersion and

the bunch length of the photon beam. Assuming the collisions occur at the waist (z = 0) of both beams ($\alpha_x = 0$, $\alpha_y = 0$), Equation 5.2.32 can be reduced as:

$$f_e(\vec{\mathbf{r}},\vec{\mathbf{p}},t) = \frac{1}{(2\pi)^3 \varepsilon_x \varepsilon_y \sigma_p \sigma_l} \exp\left[-\frac{(x^2 + \beta_x^2 x'^2)}{2\varepsilon_x \beta_x} - \frac{(y^2 + \beta_y^2 y'^2)}{2\varepsilon_y \beta_y} \right.$$

$$\left. - \frac{(p_z - p_0)^2}{2\sigma_p^2} - \frac{(z - ct)^2}{2\sigma_l^2} \right], \qquad (5.2.34)$$

$$\sigma_{x,y} = \sqrt{\varepsilon_{x,y} \beta_{x,y}}, \quad \sigma_{x',y'} = \sqrt{\varepsilon_{x,y} / \beta_{x,y}}.$$

Substituting Equations 5.2.34 and 5.2.33 into and integrating Equation 5.2.31, for σ_l^2, $\sigma_z^2 << \beta_0$ and for $\theta_i \cong \pi$, $\beta \cong 1$, one arrives at

$$A \cong \frac{\lambda\beta_0}{2} \sqrt{1 + \frac{4\pi\varepsilon_x \beta_x}{\lambda\beta_0}} \sqrt{1 + \frac{4\pi\varepsilon_y \beta_y}{\lambda\beta_0}}. \qquad (5.2.35)$$

Neglecting the energy (momentum) spread of the electron beam and the wave vector spread of the photon beam (typically $\sigma_p/p \approx 10^{-3}$ and $\Delta\lambda/\lambda \approx 10^{-4}$ - 10^{-5} in the Duke/OK-4 FEL), one arrives at a simple form for the total flux of γ rays. For a two-bunch operation, there is only one collision point and the total flux is given by

$$\dot{N}_\gamma = 2.238 \times 10^{12} \frac{\sigma_{tot}}{A} \dot{N}_{ph} I_{e,ave}[A]. \qquad (5.2.36)$$

The quality of γ rays is determined dominantly by the quality of the electron beam when the recoil parameter is small. In an ideal case (no energy spread and no angular spread), the γ-ray energy is determined by the observation angle. In reality, the energy resolution and energy distribution of the γ rays are affected by the electron beam quality. However, the effects of the energy or angular spread of the electron beams

on the total flux of γ rays is negligible in the Duke system. The dependence of γ-ray energy resolution on various experimental parameters is summarized in Table 5.2.1.

Parameters	Dependences	Factors	Typical contributions
$\Delta E_e/E_e$	$2\left(1-2\gamma\hbar\omega/(mc^2+4\gamma\hbar\omega)\right)$	~ 2	~ 0.1 %
$\Delta E_{ph}/E_{ph}$	$\left(1-4\gamma\hbar\omega/(mc^2+4\gamma\hbar\omega)\right)$	~ 1	~ 10^{-4}
$\Delta(\gamma^2\theta_f^2)$	$mc^2/(mc^2+4\gamma\hbar\omega)$	~ 1	e-beam + collimator
$\Delta(\gamma^2\theta_i^2)$	1/4	~ 0.25	~ 10^{-2}
$\Delta(\gamma^2\theta_{ph}^2)$	$mc^2/(mc^2+4\gamma\hbar\omega)\cdot(\hbar\omega/\gamma mc^2)$	~ 10^{-8}- 10^{-9}	

Table 5.2.1 Dependence of γ-ray energy resolution on various experimental parameters.

5.2.4. Energy spectrum of γ rays

The parameters of the γ rays can be calculated from Equation 5.2.28 by specifying various experimental parameters. The total flux of γ rays in the Duke/OK-4 system is determined mostly by the average electron beam current and the average FEL power. However, the flux, energy resolution, and peak energy of the γ rays after the collimator critically depend on the incoming beam parameters. Before we calculate the energy distribution at a target or a detector, we examine the energy dependence of all the parameters in Equation 5.2.2. Table 5.2.1 shows that the energy

spread of the photon beam, the incoming angles, and the angles between incoming and outgoing photons contribute little to the energy resolution of the γ rays. These parameters have a small effect because the recoil parameters and the angular spreads of the electrons and the FEL in the Duke/OK-4 FEL are small. The scattering angle is influenced by the beam size and the angles of the electrons at the collision point and by the collimator at the target or detector. Fortunately, one can choose a proper collimator to satisfy the experimental requirements. Otherwise the energy spread of the γ rays would depend linearly on the size and the angular spread of the electron beams.

The derivation of the energy spectrum of γ rays given above mostly followed the method in the reference [Litvinenko 1995a]. In here, we extend the calculation from a pinhole collimator case to an arbitrary collimator case. We also change the Dirac delta function $\delta(f)=\delta(E_\gamma-\hbar\omega')$ to $\delta(\gamma-\gamma_r)$ (instead of $\delta(\theta_x-\theta_{x,r})$) because the first derivative of the function f with respect to γ gives a smooth function.

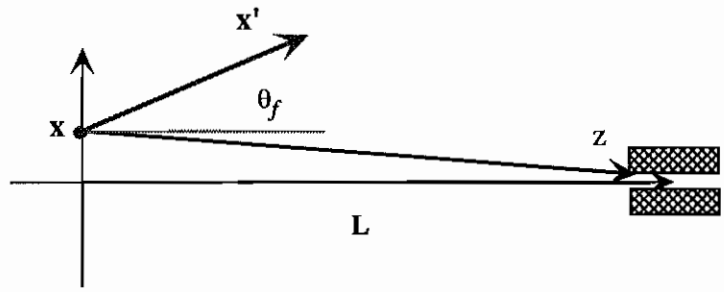

Figure 5.2.8. Schematic layout of the geometry of the scattered angle θ_f.
x and x': position and angle of incoming electron at the collision point; L: distance between the collision point and the collimator; θ_f: scattered angle, $\hat{p}\cdot\hat{k}'=\cos\theta_f$.

The γ-ray energy distributions are determined by the scattered photons that pass through the collimator. As shown in Fig. 5.2.8, the scattered photons from an electron beam with both a finite size and a finite angular spread can pass through the collimator constrained by the geometry of the collimator. These conditions are:

$$\theta_f^2 \approx \theta_x^2 + \theta_y^2 \quad (\because \theta_f \le \gamma^{-1} \sim 10^{-3}),$$

$$\theta_x \cong x' + {(x - c_x)}/{L}, \quad \theta_y \cong y' + {(y - c_y)}/{L}, \tag{5.2.37}$$

where (c_x, c_y) is an arbitrary point inside the opening of the collimator and L is distance between the collision point and the collimator. Since the dependence on θ_i and θ_{ph} is negligible compared to the dependence on the electron beam parameters, we reduce the problem to a simple "*head-on collision*". From energy conservation considerations, the scattered photons must satisfy

$$\delta(E_\gamma - \hbar\omega') \approx \delta\left(E_\gamma - \frac{4\gamma^2 \hbar\omega}{1 + \gamma^2\theta_f^2 + 4\gamma\hbar\omega/mc^2} \right). \tag{5.2.38}$$

By substituting Equations 5.2.32, 5.2.33, and 5.2.37 into Equation 5.2.28, one can calculate the energy spectrum by integrating [Litvinenko 1995a]:

$$\frac{dN_\gamma(E_\gamma)}{dE_\gamma d\Omega} = N_e N_{ph} c \int\int\int\int dp^3 dk^3 dV dt$$

$$\cdot \frac{d\sigma(\vec{\mathbf{p}}, \vec{\mathbf{k}}; k', \theta_f)}{d\Omega} (1+\beta) f_e(\vec{\mathbf{r}}, \vec{\mathbf{p}}, t) f_{ph}(\vec{\mathbf{r}}, \vec{\mathbf{k}}, t) \delta(E_\gamma - \hbar\omega'), \tag{5.2.39}$$

where the differential scattering cross section is given in Equation 5.2.19. Since the scattering cross section is independent of the spatial coordinates and the time t, and

the incoming photon angles ϑ_x and ϑ_y, one can integrate the incoming electron and photon distribution functions over $dVdtd\vartheta_x d\vartheta_y$ [Appendix E]. Then,

$$\frac{dN_\gamma(E_\gamma)}{dE_\gamma d\Omega} = \frac{N_e N_{ph}\cdot k/\beta_0}{(2\pi)^3\sigma_k\sigma_p}\sqrt{\frac{\beta_x\beta_y}{\varepsilon_x\varepsilon_y\xi_x\xi_y}}\iiint dpd\theta_x d\theta_y dk\frac{d\sigma(p,\theta_x,\theta_y,k;k')}{d\Omega}(1+\beta)$$

$$\times\exp\left[-\frac{(\theta_x+c_x/L)^2}{2\sigma_{\theta_x}^2}-\frac{(\theta_y+c_y/L)^2}{2\sigma_{\theta_y}^2}-\frac{(p_z-p_0)^2}{2\sigma_p^2}-\frac{(k-k_0)^2}{2\sigma_k^2}\right]\delta(E_\gamma-\hbar\omega'), \quad (5.2.40)$$

where

$$\sigma_{\theta_{x,y}}^2=\frac{\varepsilon_{x,y}\xi_{x,y}}{\beta_{x,y}\zeta_{x,y}},\ \xi_{x,y}=1+\left(\alpha_{x,y}-\frac{\beta_{x,y}}{L}\right)^2+\frac{4\pi\varepsilon_{x,y}\beta_{x,y}}{\lambda\beta_0},\ \zeta_{x,y}=1+\frac{4\pi\varepsilon_{x,y}\beta_{x,y}}{\lambda\beta_0}.$$

For a pinhole collimator located at the center of the beam (c_x= 0 and c_y = 0), Equation 5.2.40 is simplified to

$$\frac{dN_\gamma(E_\gamma)}{dE_\gamma d\Omega} = \frac{N_e N_{ph}\cdot k/\beta_0}{(2\pi)^3\sigma_k\sigma_p}\sqrt{\frac{\beta_x\beta_y}{\varepsilon_x\varepsilon_y\xi_x\xi_y}}\iiint dpd\theta_x d\theta_y dk\frac{d\sigma(p,\theta_x,\theta_y,k;k')}{d\Omega}(1+\beta)$$

$$\times\exp\left[-\frac{\theta_x^2}{2\sigma_{\theta_x}^2}-\frac{\theta_y^2}{2\sigma_{\theta_y}^2}-\frac{(p_z-p_0)^2}{2\sigma_p^2}-\frac{(k-k_0)^2}{2\sigma_k^2}\right]\delta(E_\gamma-\hbar\omega'). \quad (5.2.41)$$

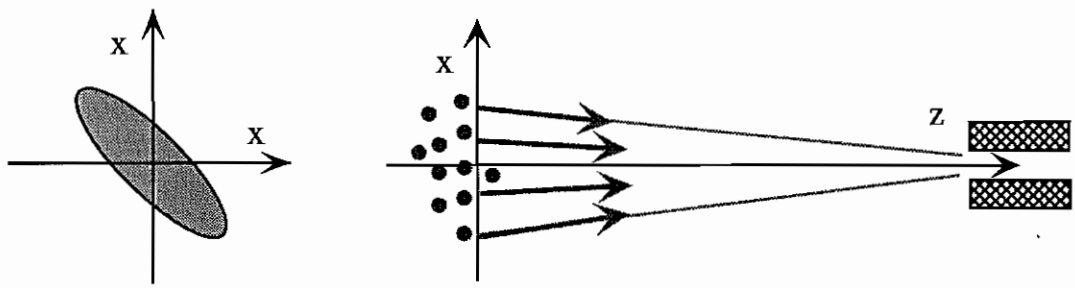

Fig. 5.2.9 Schematic diagram of γ-ray focusing due to electron beam distribution in phase space.

The energy spread of the γ rays due to the finite size and angular spread of the electron beam can be reduced through appropriate choices of the beta functions or the Rayleigh range. Also one can minimize the energy spread by adjusting the electron beams at the collision point to satisfy the condition $\alpha_{x,y} = \frac{\beta_{x,y}}{L}$. When the electron distribution in the phase space is matched (as shown in Fig. 5.2.9) so that electrons with positive position in x or y have negative angles (and vice versa) and each angle at the collision point satisfies the above geometric conditions, then the scattered γ rays are automatically focused on the target or detector. Ideally, one needs an apparatus to precisely measure the electron beam near the collision point. However, this condition would result in an increase in the effective area of overlap (see Equation 5.2.35) and result in a reduction of flux.

Since the vertical emittance in the Duke storage ring is ~ 1/10 of the horizontal emittance, the horizontal angular spread of the electron beams contributes dominantly to the energy spread of the γ rays. Furthermore, according to Table 5.2.1, the growth of the energy spread of the γ rays due to the incoming photon energy spread is much smaller than due to the energy spread and horizontal angular spread of the incoming electrons. We can simplify Equations 5.2.40 or 5.2.41 by assuming that the contribution of θ_y and k are negligible compared to that of the energy spread and horizontal angular spread of the electron beam. Integrating over θ_y and k and changing the variable momentum p ($p = \gamma\beta mc \approx \gamma mc$) to the energy parameter γ, we obtain

$$\frac{dN_\gamma(E_\gamma)}{dE_\gamma d\Omega} = N_e N_{ph} \frac{k/\beta_0}{4\pi^2\sigma_\gamma}\sqrt{\frac{\beta_x}{\varepsilon_x\xi_x\zeta_y}}\int\int d\gamma d\theta_x \frac{d\sigma(\gamma,\theta_x;k',k_0,\theta_y=0)}{d\Omega}(1+\beta)$$

$$\times\exp\left[-\frac{(\theta_x+c_x/L)^2}{2\sigma_{\theta_x}^2}-\frac{(\gamma-\gamma_0)^2}{2\sigma_\gamma^2}\right]\delta(E_\gamma-\hbar\omega'). \qquad (5.2.42)$$

The double integrations can be reduced to a single integration by using the Dirac delta function relation,

$$\delta(f(x))=\sum_i \delta(x-x_i)\left|\frac{df(x)}{dx}\right|^{-1}_{x=x_i}.$$

Therefore, by integrating with respect to γ,

$$\frac{dN_\gamma(E_\gamma)}{dE_\gamma d\Omega} \approx N_e N_{ph} \frac{k/\beta_0}{2\pi^2\sigma_\gamma}\sqrt{\frac{\beta_x}{\varepsilon_x\xi_x\zeta_y}}\int_0^{\theta_{max}} d\theta_x \frac{d\sigma(E_\gamma,\theta_x;k_0,\theta_y=0,\gamma=\gamma_r)}{d\Omega}$$

$$\times\frac{(1+\gamma_r^2\theta_x^2+4\gamma_r a)}{8\gamma_r\hbar\omega(1+2\gamma_r a)}\exp\left[-\frac{(\theta_x+c_x/L)^2}{2\sigma_{\theta_x}^2}-\frac{(\gamma_r-\gamma_0)^2}{2\sigma_\gamma^2}\right], \qquad (5.2.43)$$

where

$$\gamma_r=\frac{2E_\gamma a}{(4\hbar\omega-E_\gamma\theta_x^2)}\left\{1+\sqrt{1+\frac{(4\hbar\omega-E_\gamma\theta_x^2)}{4E_\gamma a^2}}\right\},\ \theta_{max}=\sqrt{4\hbar\omega/E_\gamma},\ a=\frac{\hbar\omega}{mc^2}.$$

For a finite size collimator at an arbitrary position, the flux is obtained by integrating Equation 5.2.43 over the collimator opening center c_x of collimator, i.e., ($c_x - \Delta x/2$, $c_x + \Delta x/2$):

$$\frac{\Delta N_\gamma(E_\gamma)}{dE_\gamma d\Omega} \approx N_e N_{ph} \frac{k/\beta_0}{2\pi^2\sigma_\gamma}\sqrt{\frac{\beta_x}{\varepsilon_x\xi_x\zeta_y}}\int_{c_x-\Delta x/2}^{c_x+\Delta x/2} dc_x \int_0^{\theta_{max}} d\theta_x \frac{d\sigma(E_\gamma,\theta_x;k_0,\theta_y=0,\gamma=\gamma_r)}{d\Omega}$$

$$\times\frac{(1+\gamma_r^2\theta_x^2+4\gamma_r a)}{8\gamma_r\hbar\omega(1+2\gamma_r a)}\exp\left[-\frac{(\theta_x+c_x/L)^2}{2\sigma_{\theta_x}^2}-\frac{(\gamma_r-\gamma_0)^2}{2\sigma_\gamma^2}\right]. \quad (5.2.44)$$

Figures 5.2.10, 5.2.11, and 5.2.12 illustrate the dependence of the γ-ray spectra on both the energy spread and the angular spread (emittance and beta function) of the electron beam for a pinhole collimator (i.e., $c_x = 0$ and $\Delta x = 0$). The energy spread of the electron beam has a larger effect on the γ-ray energy resolution than the angular spread of the electron beam. Increasing the angular spread does not change the peak energy, whereas the peak energy shifts toward lower energy as the energy spread of the electron beam becomes larger. However, the peak energy shifts toward higher energy as the emittance of the electron beam becomes smaller, as shown in Figure 5.2.13. Therefore, we can see the shift of the peak energy of γrays is due to both parameters (energy spread and emittance), not just one of them. The flux of γrays for a higher energy electron beam is more sensitive to the angular spread of the electron beam than for a lower energy electron beam. This sensitivity arises from the narrower scattering angle of the higher energy electron beam. The energy resolution of γrays is better at low operating energy as expected from the g-function in Equation 5.2.22. The energy resolution is better even for the same level of the energy spread of electron beam, as the ring has a smaller emittance at low operating energies.

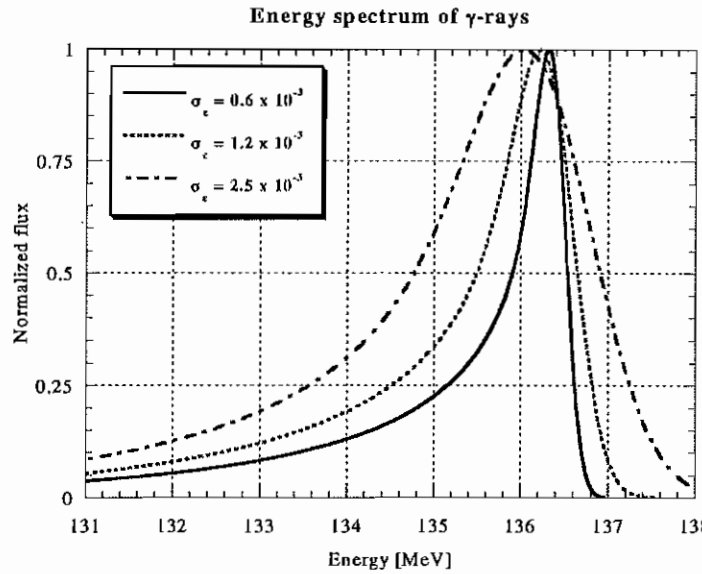

Fig. 5.2.10. Dependence of energy spectrum of γ rays on the energy spread of the electron beam.
Incoming electron beam: $E_e = 1$ GeV, $\varepsilon_x = 18\times10^{-9}$ m·radian, and $\beta_x = 4$ m.
Incoming photon beam: $\lambda = 120$ nm and $\beta_0 = 3.36$ m.
(solid curve: $\sigma_\varepsilon = 0.6$ x 10^{-3}; dotted curve: $\sigma_\varepsilon = 1.2$ x 10^{-3}; dashed curve: $\sigma_\varepsilon = 2.5$ x 10^{-3})

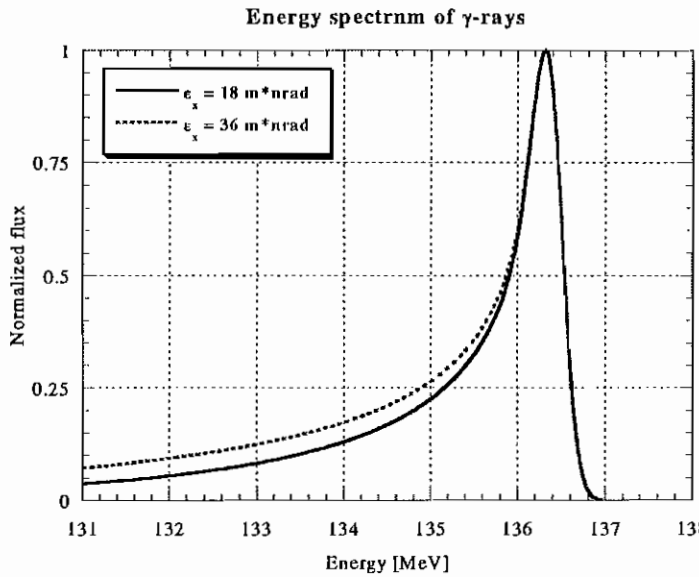

Fig. 5.2.11. Dependence of energy spectrum of γ rays on the emittance of the electron beam.
Incoming electron beam: $E_e = 1$ GeV, $\sigma_\varepsilon = 0.6$ x 10^{-3}, and $\beta_x = 4$ m.
Incoming photon beam: $\lambda = 120$ nm and $\beta_0 = 3.36$ m.
(solid curve: $\varepsilon_x = 18\times10^{-9}$ m·radian; dotted curve: $\varepsilon_x = 36\times10^{-9}$ m·radian)

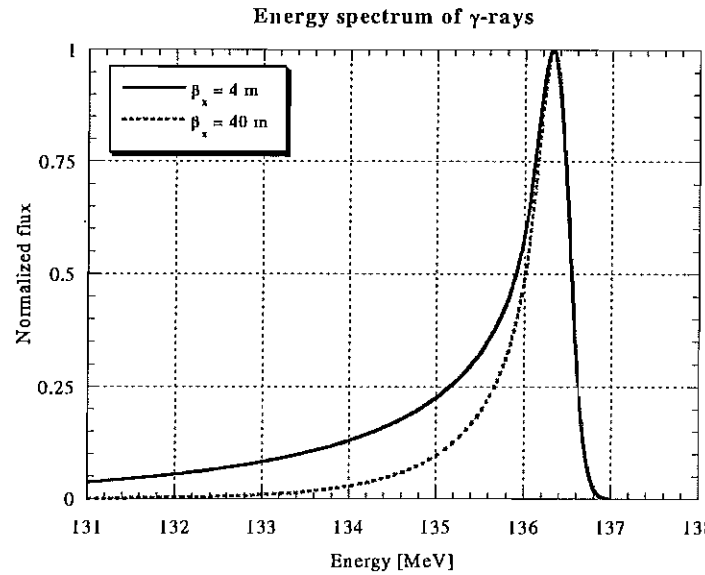

Fig. 5.2.12. Dependence of energy spectrum of γ rays on the beta function of the electron beam. Incoming electron beam: $E_e = 1$ GeV, $\sigma_\varepsilon = 0.6 \times 10^{-3}$, and $\varepsilon_x = 18 \times 10^{-9}$ m·radian. Incoming photon beam: $\lambda = 120$ nm and $\beta_0 = 3.36$ m. (solid curve: $\beta_x = 4$ m; dotted curve: $\beta_x = 40$ m)

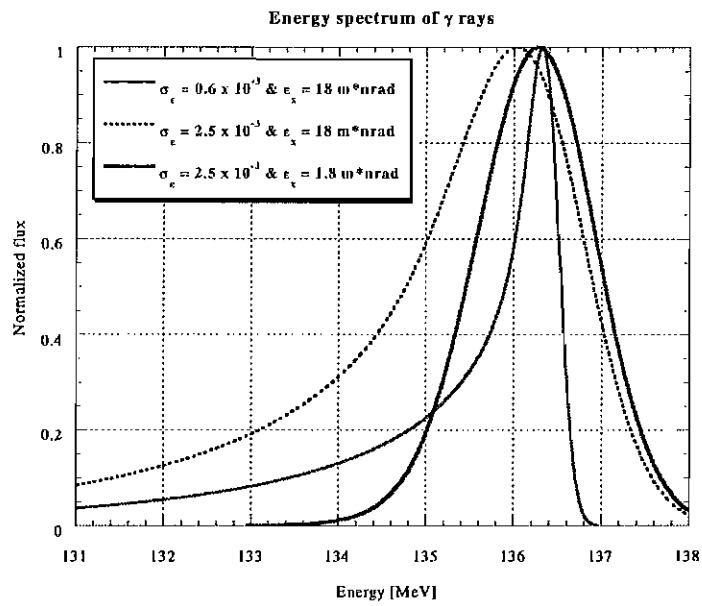

Fig. 5.2.13. Dependence of the peak energy of γ rays on the energy spread and the emittance of the. electron beam. (Incoming electron beam: $E_e = 1$ GeV and $\beta_x = 4$ m; Incoming photon beam: $\lambda = 120$ nm and $\beta_0 = 3.36$ m) The solid and dotted curves are the same as the solid and dashed curve in Figure 5.2.10. The third curve (thick solid curve) is the case that the energy spread is equal to that of dotted curve but the emittance is ten times smaller than other two curves.

5.3. γ rays via Compton backscattering: Experiments

5.3.1. Generation of γ rays

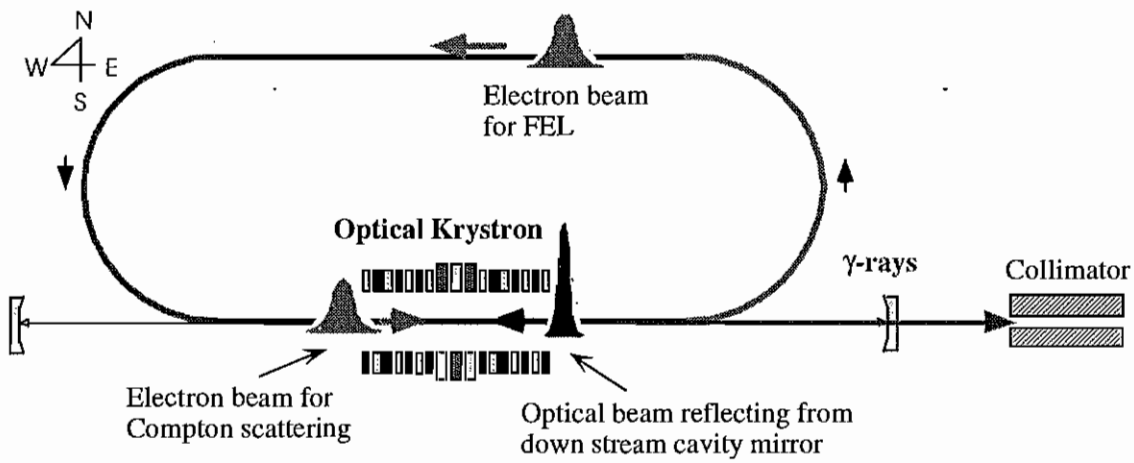

Fig.5.3.1 Schematics of γ-ray generation in the Duke/OK-4 SR FEL.

Figure 5.3.1 illustrates the schematic layout of the Duke/OK-4 SR FEL for γ-ray generation. Two electron bunches (or any number of pairs) are stored in the storage ring, separated by a distance equal to half the circumference of the ring. γ rays are generated by a collision of the electron bunch with the optical bunch (generated by the other electron bunch). As the number of electron bunches is increased, the γ-ray flux increases. However, γ-ray production is sensitive to high

order modes of the RF cavity. These high order modes cause the energy resolution of the γ rays to become slightly worse than the two-bunch operation because of more than one collision point in the straight section. With four electron bunches, collisions occur at three points in the south straight section of the Duke storage ring. For low energy γ-ray generation the corresponding electron beam energy is reduced. Since γ-ray flux drops approximately as the electron beam energy to the fourth power (due to the reduction of the optimized FEL power for lower energies of the electron beam with the same average currents), the flux at low γ-ray energies may be small for some applications. Hence, to increase the flux, one must increase either the electron beam current per bunch or the number of electron bunches. As shown in Figure 3.2.6, the lifetime of the electron beam decreases at low operating energies due to instabilities and is further reduced by γ-ray generation. Below a 300 MeV operating energy, electrons can be continuously injected into the beam to maintain lasing. In this mode, flux is increased at the expense of the γ-ray energy resolution. We can also produce γ rays in a giant pulse mode. This strongly increases the peak flux of the γ rays at the expense of the average flux. Table 3.4.1 shows parameters of γ rays generated at the Duke/OK-4 system.

The collision point is located at the center of the OK-4 FEL cavity in a 20 cm field-free region between the first wiggler and the buncher. A lead collimator was placed approximately 30 m from the collision point and a detector approximately 1 m behind the collimator. Because of their good resolution, HPGe detectors were used to

study of the energy spread of γ rays at low energies. However, for γ-ray energies above 15 MeV, NaI detectors were used due to their superior efficiency. The tunability of the γ rays depends on the bandwidth of the cavity mirrors, but is wider than the FEL tuning range because the energy of the electron beam can also be easily changed. With different sets of cavity mirrors, γ rays were generated at energies between 1.9 MeV and 55 MeV. The total flux measured was on the order of 10^5 to 10^7 γ's/sec, depending on the lasing parameters and the electron beam energy. A 3 mm diameter lead collimator results in typical energy resolutions of 0.7% (FWHM); the best resolution measured was 0.5%.

Figure 5.3.2 shows a typical spectrum of the high energy γ rays measured in a 10" x 10" NaI detector. Figure 5.3.3 shows a typical spectrum of low energy γ rays using a HPGe detector. As expected from theory, the energy resolution is approximately 1% for high energy γ rays and approximately 0.5% for low energy γ rays.

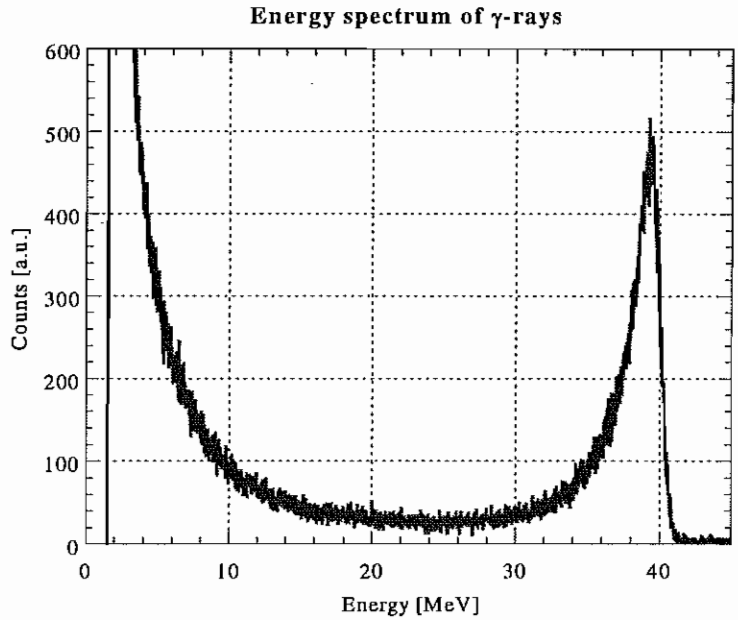

Fig.5.3.2 A typical high energy γ-ray spectrum measured by a 10" x 10" NaI detector. (The energy resolution of a 10" x 10" NaI(Tl) detector is ~ 5 % FWHM for γ rays of this energy.)

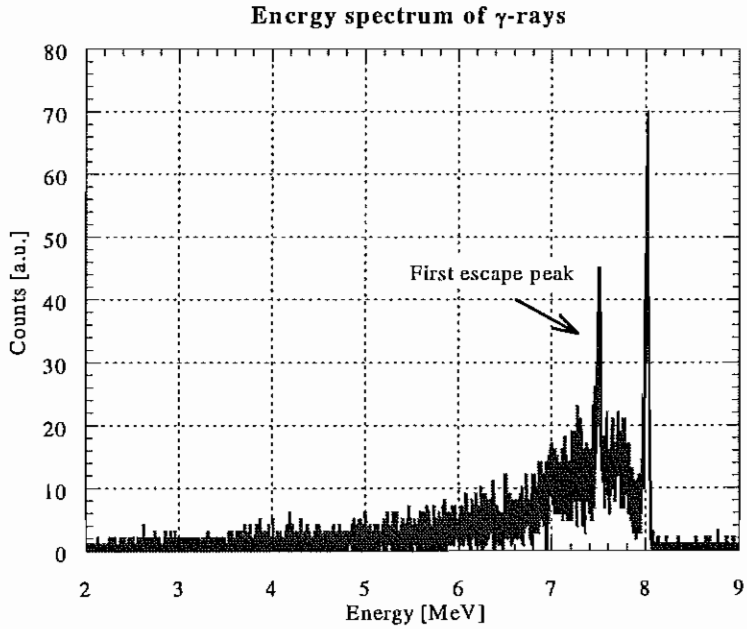

Fig.5.3.3 A typical low energy γ-ray spectrum measured by a HPGe detector. (The energy resolution of the detector is less than ~ 0.1 % FWHM for γ-rays with energy below 12 MeV.)

5.3.2 Energy spectrum of γ rays

Figures 5.3.4 – 5.3.6 show typical γ-ray spectra generated at the Duke/OK-4 system. As the peak energy and the energy resolution strongly depend on the direction of the electron beam at the collision point, the collimator should be re-aligned (even though it is pre-aligned using the FEL) at the center of the γ rays or the direction of the electron beam should be corrected by changing the current in the trims on both sides of the optical klystron. Figure 5.3.7 shows the angular dependence of the energy resolution and peak energy on position. These results indicate the importance of alignments to the electron beam and collimator.

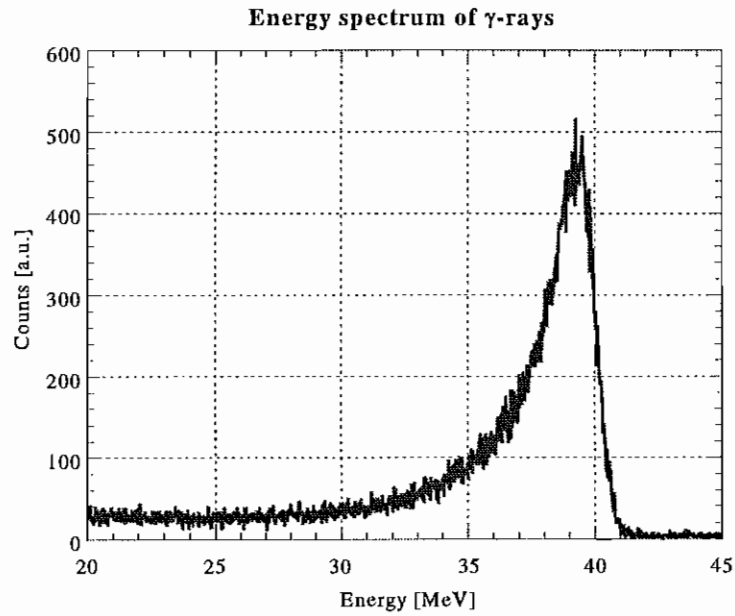

Fig. 5.3.4 Spectrum of γ rays through a 3 mm collimator measured using a NaI detector. Electron beam: 700 MeV and 4.78 mA/2 bunches; Photon beam: 5.21 eV; γ rays: 39.2 MeV with FWHM energy resolution of 5 %.

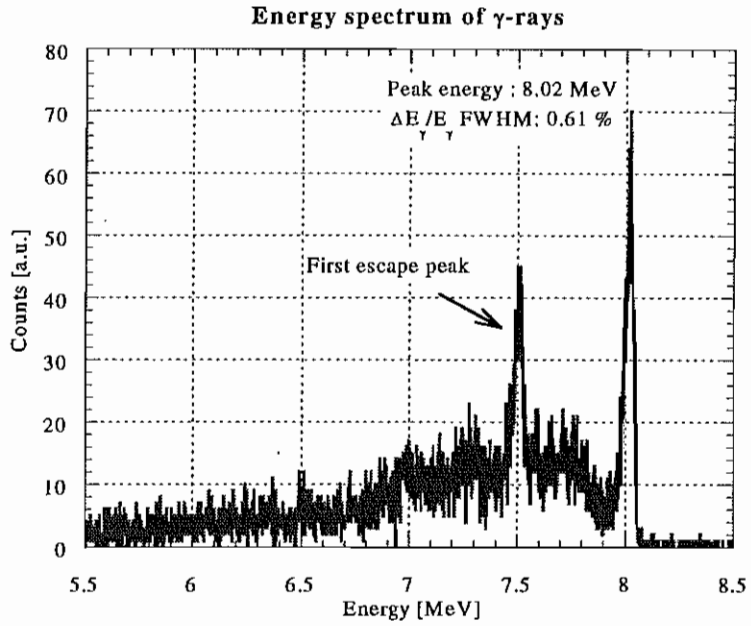

Fig. 5.3.5 Spectrum of γ rays through a 3 mm collimator measured using a HPGe detector. Electron beam: 500 MeV and 2.8 mA/2 bunches, V_{RF} = 150 kV; Photon beam: 2.1 eV; γ rays: 8.02 MeV with FWHM energy resolution of 0.61%

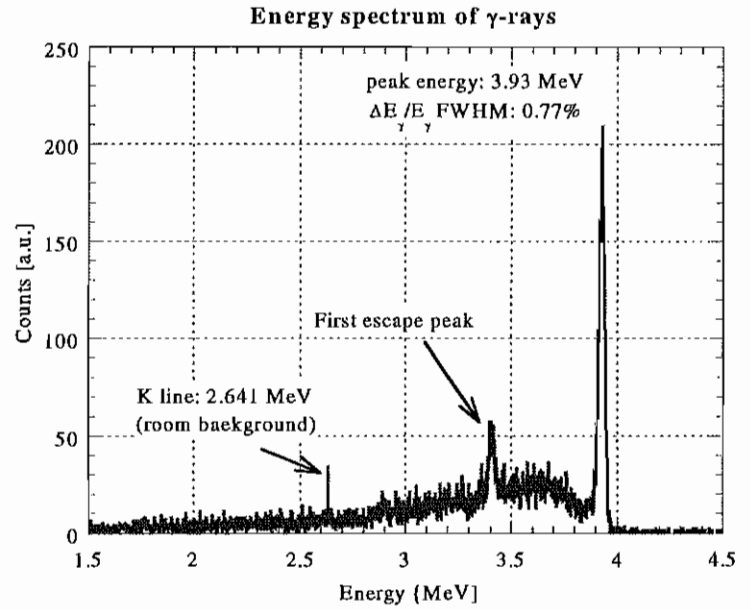

Fig. 5.3.6 Spectrum of γ rays through a 3 mm collimator measured using a HPGe detector. Electron beam: 350 MeV and 5.12 mA/2 bunches, V_{RF} = 400 kV; Photon beam: 1.79 eV; γ rays: 3.93 MeV with FWHM energy resolution of 0.77%

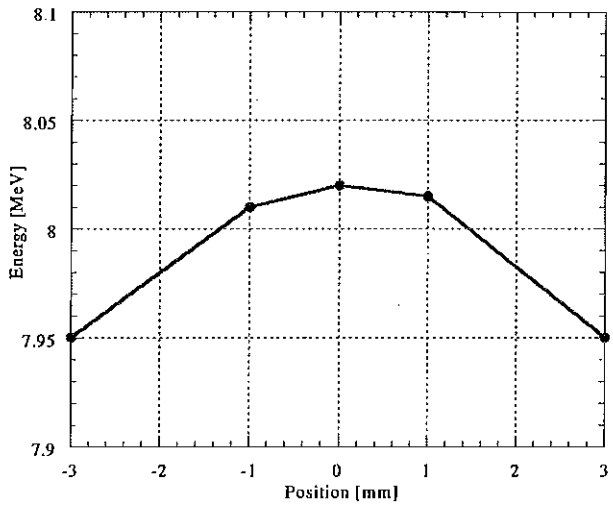

(A) Peak energy

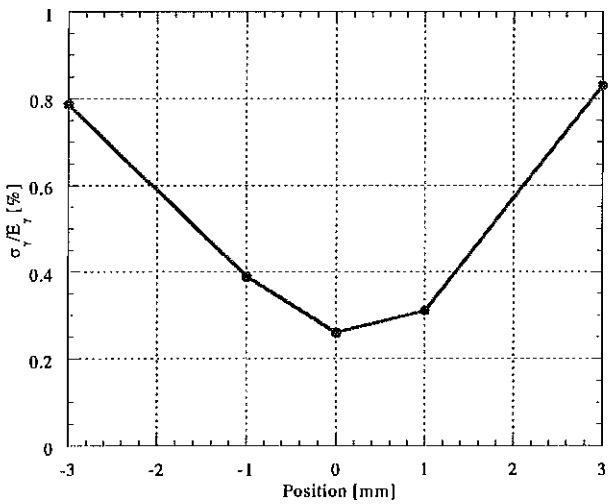

(B) Energy spread

(a)

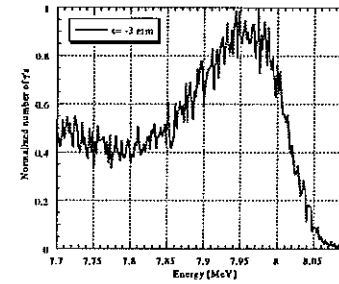

(b)

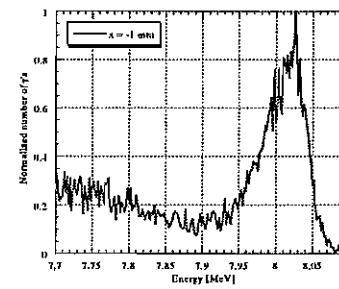

(c)

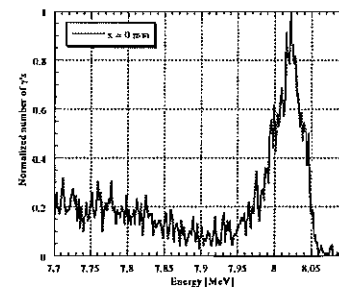

(d)

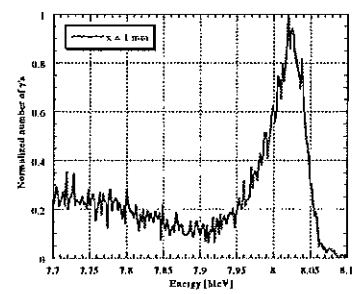

(e)

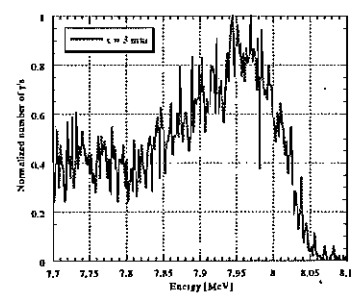

Fig. 5.3.7. Dependence of peak energy (A) and energy spread (B) on the position of the collimator from the optical axis. (a)-(e): energy spectra of γ rays as the collimator position is scanned. ((a): -3 mm; (b): -1 mm; (c): 0 mm; (d): 1 mm; (e): 3 mm)

The dependence of the γ-ray flux on FEL power agrees well with theoretical predictions. When the FEL and the γ-ray flux are optimized, the FEL power increases as the electron energy to the fourth power, γ^4, and as the beam current to the α^{th} power, I_e^{α}. The total γ-ray flux also increases as the electron energy to the fourth power, γ^4, but as the beam current to the $(\alpha+1)^{th}$ power, $I_e^{\alpha+1}$ (see Section 2.5). The factor α includes the contribution of the beam current to the induced energy spread. The factor α was between 1.5 and 2.2 according to our measurements. Figures 5.3.8 and 5.3.9 show the relationship between the FEL power and γ-ray flux at different operating energies.

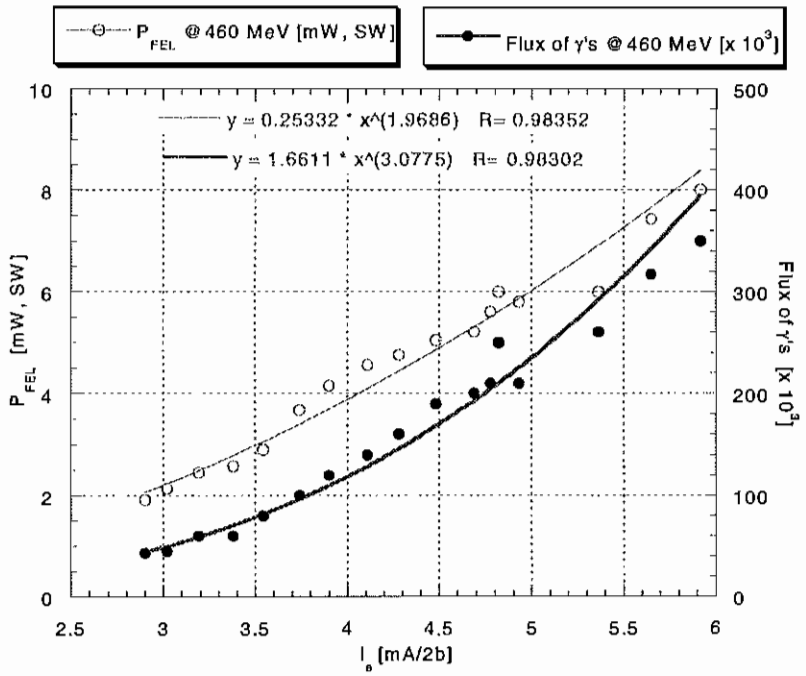

Fig. 5.3.8 Relationship between γ-ray flux and FEL power.
(460MeV e-beam and 385 nm FEL)

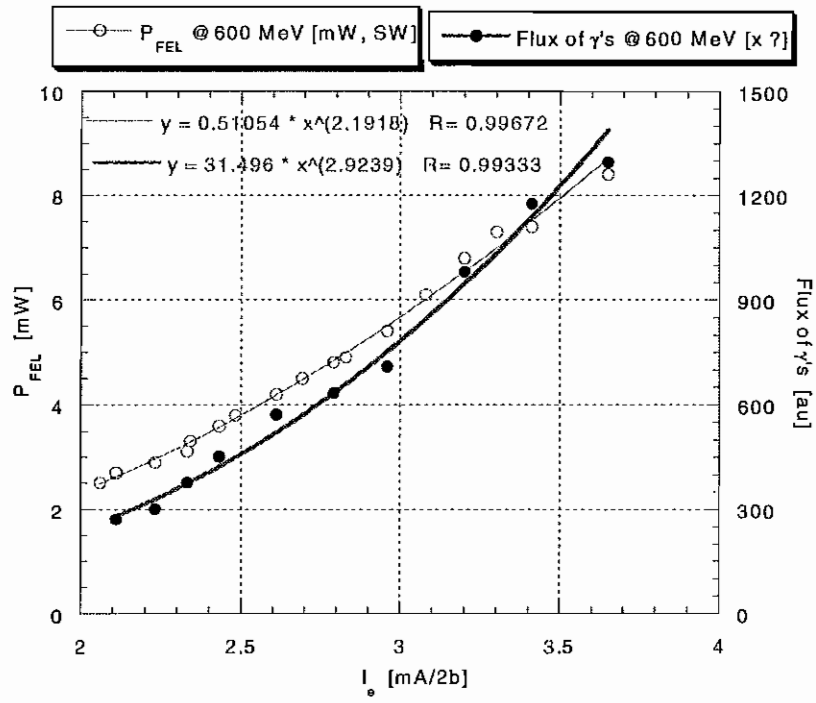

Fig. 5.3.9 Relationship between γ-ray flux and FEL power.
(600MeV e-beam and 370 nm FEL)

5.3.3 Dependences on the electron beam parameters

Figures 5.3.10 - 5.3.16 show theoretical predictions of γ-ray energy spectra using different measured electron beam parameters for 460 MeV electron beams and a 385 nm FEL. The theoretical predictions agreed amazingly well with the measured spectra. Figures 5.3.10 – 5.3.14 are the measured spectra at different buncher currents (i.e., different total slippage), whereas Figures 5.3.15 and 5.3.16 are spectra at different RF voltages with fixed buncher current. Appendix C lists the measured parameters of the electron beam and γ rays. As we mentioned in Section 3.2.2, the

horizontal emittance does not change significantly due to the FEL interaction, γ-ray generation, and the electron beam current. In the Duke/OK-4, the energy resolution of the γ rays is determined mainly by the induced energy spread of the electron beam. For generating high flux γ rays, the buncher current was adjusted for optimal FEL power, while, for better energy resolutions of the γ rays, we increased the buncher current to decrease the induced energy spread of the electron beam (see Section 3.5). Decreasing the RF cavity voltage also reduces the energy spread of the electron beam, but this also causes a reduction in the energy acceptance. In high energy γ-ray generation, high RF cavity voltages allow γ-ray generation in a no-loss mode.

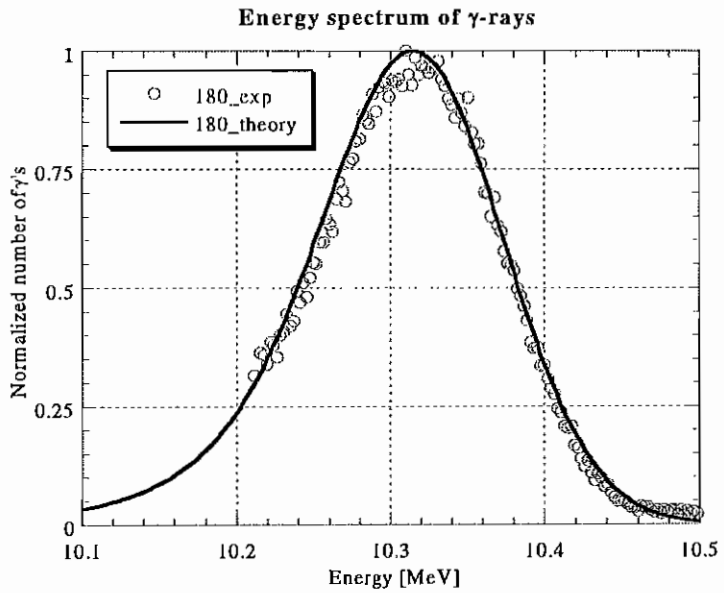

Fig. 5.3.10 The measured and calculated spectrum of γ rays (#180).
(2.64×10^{-3} relative energy spread and 16.2×10^{-9} m·rad horizontal emittance of e-beam)

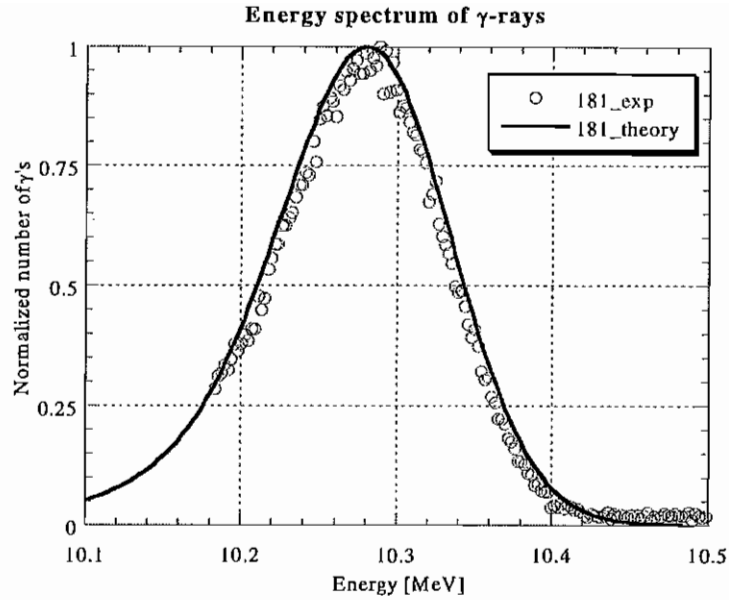

Fig. 5.3.11 The measured and calculated spectrum of γ rays (#181).
(2.44 x 10^{-3} relative energy spread and 15.6 x 10^{-9} m·rad horizontal emittance of e-beam)

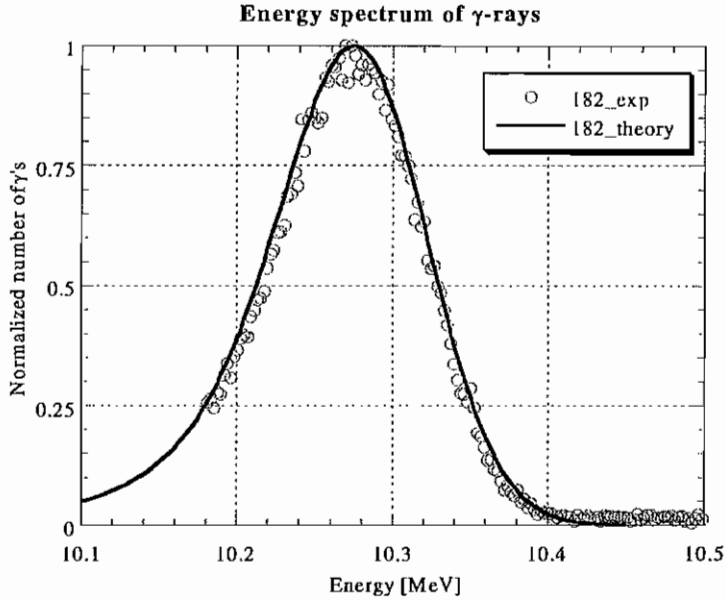

Fig. 5.3.12 The measured and calculated spectrum of γ rays (#182).
(2.10 x 10^{-3} relative energy spread and 16.2 x 10^{-9} m·rad horizontal emittance of e-beam)

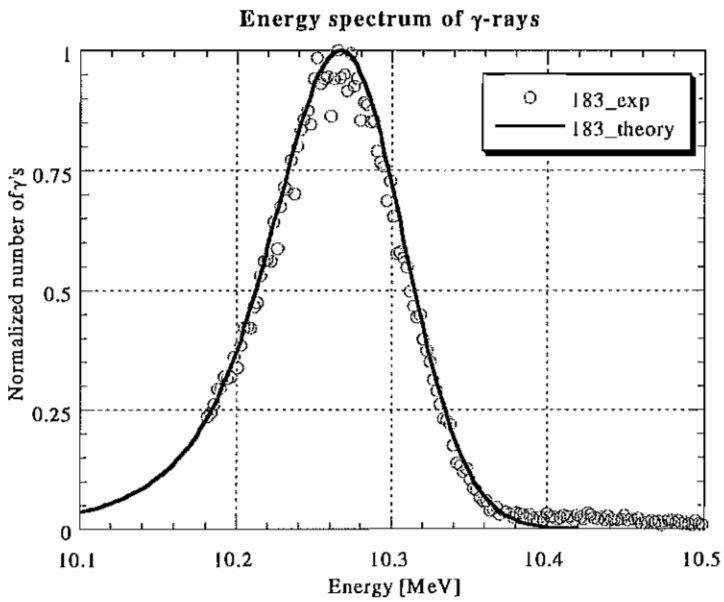

Fig. 5.3.13 The measured and calculated spectrum of γ rays (#183).
(1.84×10^{-3} relative energy spread and 13.7×10^{-9} m·rad horizontal emittance of e-beam)

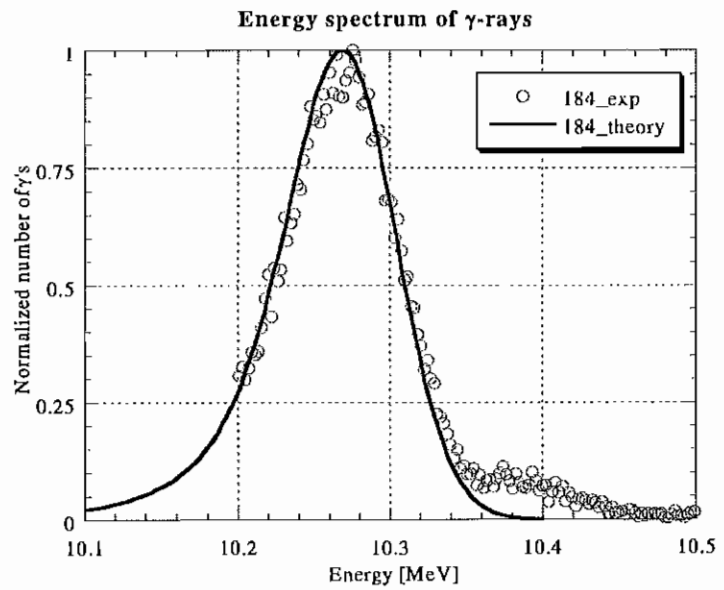

Fig. 5.3.14 The measured and calculated spectrum of γ rays (#184).
(1.58×10^{-3} relative energy spread and 12.2×10^{-9} m·rad horizontal emittance of e-beam)

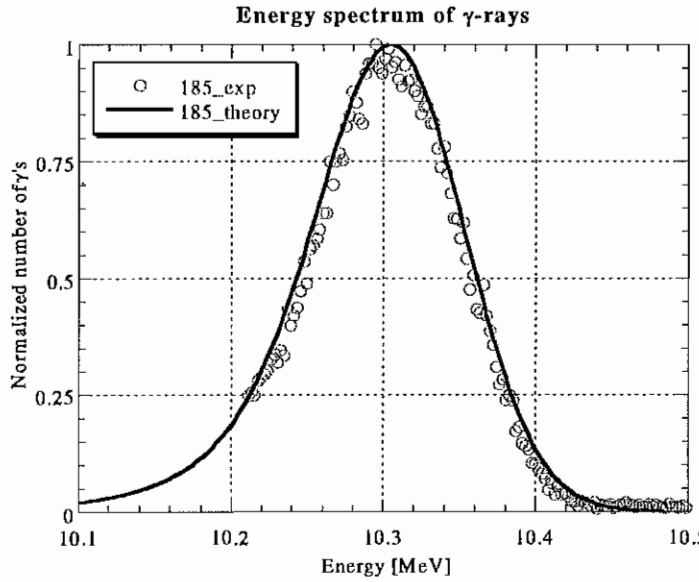

Fig. 5.3.15 The measured and calculated spectrum of γ rays (#185).
(2.17 x 10^{-3} relative energy spread and 13.6 x 10^{-9} m·rad horizontal emittance of e-beam)

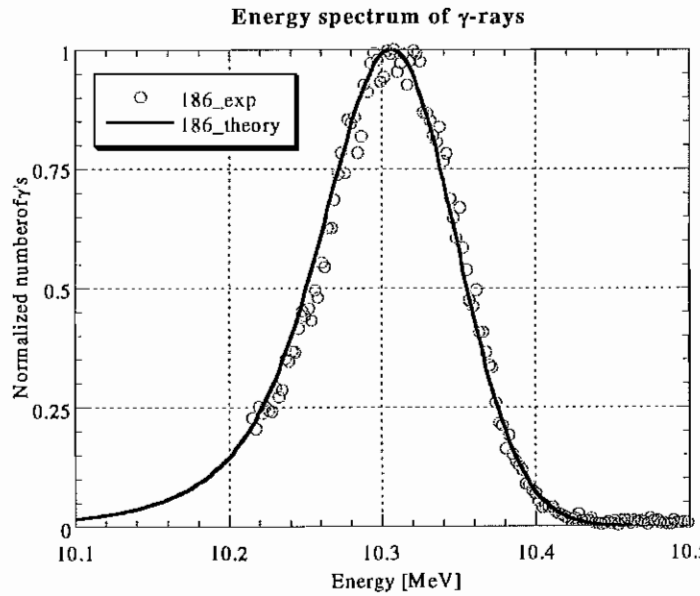

Fig. 5.3.16 The measured and calculated spectrum of γ rays (#186).
(1.88 x 10^{-3} relative energy spread and 13.9 x 10^{-9} m·rad horizontal emittance of e-beam)

5.3.4 Density distributions of γ rays

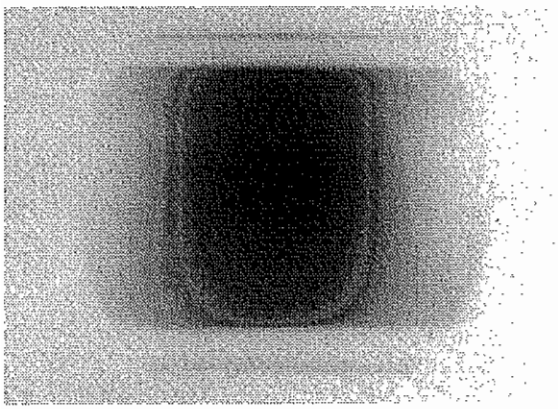

(a)-1 Photo picture

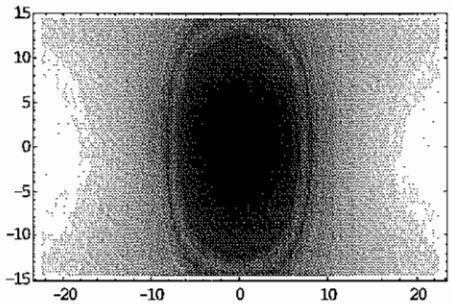

(a)-2 Theoretical plot

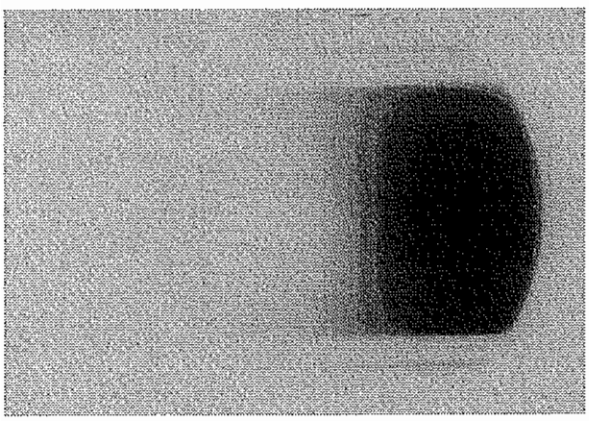

(b)-1 Photo picture

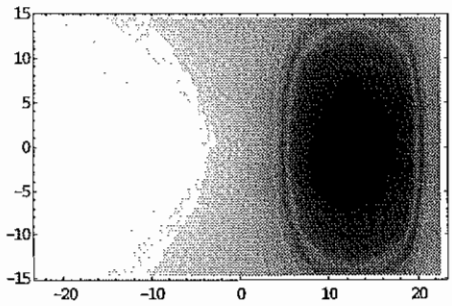

(b)-2 Theoretical plot

Fig. 5.3.17. Spatial distribution of γ rays. (a): The direction of the electron beams and optical beams are aligned at the center of the optical cavity (b) The direction of the electron beams and optical beams are tilted by 0.46 mrad.

The density distribution of γ rays can be measured by taking pictures using the X-ray films. In the photos, the effects of linearly polarized incoming photons can be observed as discussed in Section 5.2.2. Figure 5.3.17 shows the measured and calculated spatial distribution of γ rays at a distance 27.8 m from the collision point. At a 600 MeV electron beam energy, the node due to linearly polarized photons is 23.68 mm from the peak in the density distribution. The electron beam and photon beam were intentionally skewed to more clearly examine the horizontal node of the density distribution of the γ rays in image (b), which is located at –10.77 mm ("–" means left-hand side from the center of the beam line; The peak is located at + 12.91 mm.). Because of saturation and the low resolution of the X-ray films, three dimensional density plots are not as clear as the theoretically computed plot. However, the node in the horizontal direction in the photo is clearly observed. If we operate at a 1 GeV ring energy, the density distributions are smaller than those at a 600 MeV ring energy as shown in Figure 5.2.6.

Images were taken of dense materials inside slightly less dense materials (for example, a stainless steel ring inside of an aluminum cylinder). These images demonstrate the possibility of tomography of dense materials much like X-ray scanning.

Chapter 6

Conclusion

The Duke storage ring provides a unique opportunity to study the physics of a complex system consisting of intense ultra-relativistic beams of electrons, a free electron laser, and a Compton γ-ray source. We measured the parameters of the electron beams as well as the FEL light to study relationships between different variables in this complex system. The experimental measurements agree well with the theoretical predictions. Our work has pointed to improvements which should be made in the Duke/OK-4 FEL system to increase its stability.

6.1 Storage ring FELs

Recent developments and upgrades of the electron and optical beam diagnostic systems have improved the performance of the Duke/OK-4 system and allowed us to study the complex interplay between the electron beam, FEL light, and Compton backscattered γ rays. Although the FEL interaction does not result in a significant change in the emittance of the electron beam, whereas the energy spread

is increased by a factor of 2 to 3. As we expected, the performance of the FEL and the Compton backscattered γ rays are mainly determined by the energy spread of the electron beam.

Lasing was achieved at wavelengths between 193.7 nm and 720 nm using five different sets of dielectric cavity mirrors. Using a MDR-23 Monochromator (0.0128 nm resolution with 20 μm slit and 2400 grooves/mm grating) and a Hamamatsu streak camera (1.5 psec resolution in Range 1 with 30 μm pinhole slit), we measured the first Fourier limited optical pulse in a SR FEL. We found that the FEL power depends on the electron beam current as I^{α}, where the values of α were between 1.5 and 2.2 (depending on the saturation condition). The measured FEL power agreed well with the theoretical calculations using measured electron beam and optical beam parameters.

We also measured the macro-temporal structure of the Duke/OK-4 SR FEL light. There are five zones-CW, pulsed, CW, pulsed, and CW- as the cavity length is tuned. A well-synchronized zone has a CW mode with the highest power and the shortest optical pulse. The bandwidth of the CW zone at the center of the detuning curve is very narrow, approximately 0.05 Hz at a current of 3.6 mA and a beam energy of 600 MeV. The gain modulation in the pulsed zone is caused mostly by the fluctuation of magnet power supplies. We operated at a TEM_{00} transverse mode for the maximum FEL power and observed higher order modes up to the TEM_{33} mode depending on the wavelength of the FEL light.

6.2 Compton γ-ray source

We studied how the polarization and the γ-ray energy spectrum depend on the electron and optical beam parameters both theoretically and experimentally. We developed a theoretical model for the energy distribution of the γ-ray beam for arbitrary geometries of the collimator. In addition, we derived an analytical formula for the energy spectrum of γ rays that passed through a pinhole collimator (we assumed a flat electron beam). For collimators of arbitrary size and position, the flux can be calculated by integrating Equation 5.2.40 or Equation 5.2.44 (for a flat electron beam) over the collimator opening area. We compared the measured energy spectra through a 3 mm collimator at a distance of approximately 30 m from the collision point to the theoretical energy spectra through a pinhole collimator using the measured experimental beam parameters. The spectra agreed well.

The dependence of the flux on the beam current goes as $I_e^{\alpha+1}$, where α is determined by the saturation condition in the FEL. We observed that $(\alpha + 1)$ is approximately 3 for γ-ray modes. However the expected range of $(\alpha + 1)$ is between 2.5 and 3.

The main factor contributing to the energy resolution of the γ rays is the induced energy spread of the electron beam caused by due to the FEL interaction. In order to improve the energy resolution of the γ rays, a separation between the target electron bunch and the lasing electron bunch is required. The target electron bunch

must have its peak current below the lasing threshold so that the FEL gain per turn is less than the cavity loss per turn in order to avoid the growth of energy spread due to the FEL interaction. We propose that the separation of the function of the two electron bunches be achieved by using a second high order RF cavity [Park 1998].

6.3 Optical cavity

We studied the stability of the optical resonator in the Duke/OK-4 and mirror degradation due to thermal and mechanical distortion. We discovered that mechanical distortion was most critical in detuning the performance of the FEL. However, as we store more current per bunch, the thermal load on the downstream mirror increases and then thermal distortion becomes a serious problem. For shorter wavelengths, the main problem is downstream mirror degradation caused by the radiation of high order harmonics from the planar wiggler on the axis. In addition to the lack of good optical materials for short wavelengths remains a problem.

6.4 Future plans

To better understand the physics of a complex system consisting of intense ultra-relativistic beams of electrons, a free electron laser, and a Compton γ-ray source, we plan to improve the beam diagnostic system to provide more precise

measurements of the beam parameters. Further, we plan to develop a model for the γ-ray energy spectrum for arbitrary electron beam geometry (beyond the flat electron beam case). To overcome the problem of mirror degradation at short wavelengths, we plan to continue the design of a ring resonator using cylindrical mirrors as a focusing mirror (instead of ellipsoidal focusing mirror). To improve the FEL performance, we must minimize the instability of the electron beam. A separate cooling system for the RF cavity, longitudinal feedback system, high quality magnetic coils, and less noisy power supplies will lead to improvements in the stability of the FEL light and γ-ray source.

Appendix A:

The dual sweep streak camera

When a light pulse strikes a S20 photocathode with an MgF_2 window (spectral response range: 115 – 850 nm), an electronic pulse which is proportional to the intensity of the incident light is generated via the photoelectric effect. The pulse is rapidly swept by parallel electrodes in a M5675 synchroscan unit triggered at 89.273 MHz, which is one half the frequency of the RF cavity (or 34^{th} harmonic of the revolution frequency) of the Duke storage ring (see Figure A.1). The synchroscan unit provides four fast-sweep time scales referred to as Range 1 (151 psec), Range 2 (700 psec), Range 3 (1.303 nsec), and Range 4 (1.903 nsec) with a time resolution of less than 1.6 psec. The horizontal slow-sweep allows the fast vertical sweep to be repeated along the horizontal axis (see Figure A.2). This dual sweep function allows us to measure pulse widths (vertical axis) as well as the evolution of the optical pulse or the phase fluctuations between100 nsec and 100 msec (19 sweep ranges). The input optics consist of four mirrors (instead of lenses) to transmit incident light of wavelengths as low as 150 nm (transmittance: 50% at 200 nm and 10% at 150 nm). These optics are useful for the broad band spectral range because there is. no

chromatic aberration or material dispersion. The optics are 1:1 with an effective F-number of 4.

Electrons produced by the incident light striking the photocathode arrive at slightly different times and pass through a pair of accelerating electrodes to arrive at a pair of sweep electrodes. During the high-speed sweep from the top to bottom (in the vertical axis of the screen), the electrons that arrive at slightly different times are deflected at slightly different angles in the vertical direction of the scope. These electrons then enter a MCP (micro-channel plate). The electrons are multiplied several thousands times in the MCP and impact on a phosphor screen (where electrons are converted into light). Phosphor images of the light are captured with a high sensitivity video camera and transferred using a frame grabber for computer analysis.

The temporal resolution of the streak camera is determined by the pulse width of the incident light. The temporal resolution of the system is affected by the spatial spread of electrons, the deflection speed, and the deflection electric field. When the temporal resolution of the measurement system (the streak camera and any additional input optics) is τ_s in FWHM and the FWHM of the streak image (observed pulse width) is τ_m, the FWHM of the incident pulse light is determined by $\tau = \sqrt{\tau_m^2 - \tau_s^2}$.

The schematic for the experimental setup of the simultaneous measurement of the electron and optical beams is shown in Figure A.3. The temporal structure of the electron beam corresponds to that of the light pulse of spontaneous radiation

from the wigglers and the bending magnet. The spontaneous radiation from the OK-4 (collected using a periscope mirror located about 1 m in front of the downstream cavity mirror and delayed by about 100 psec) is used for bunch length measurements of the electron beam.

Since the typical induced energy spread of the electron beam is greater than 200 psec in FWHM, Range 2 of the vertical sweep time (full time scale of 700 psec) is used for simultaneous measurements. Range 1 (full time scale of 150 psec) is used for the micro-temporal structure of the FEL light on the vertical axis. By varying the horizontal time scales, the evolution of the FEL in a turn-by-turn (in a full time scale less than 5 μsec) or in a long time (in a full time scale more than 500 μsec) is observed on the horizontal axis.

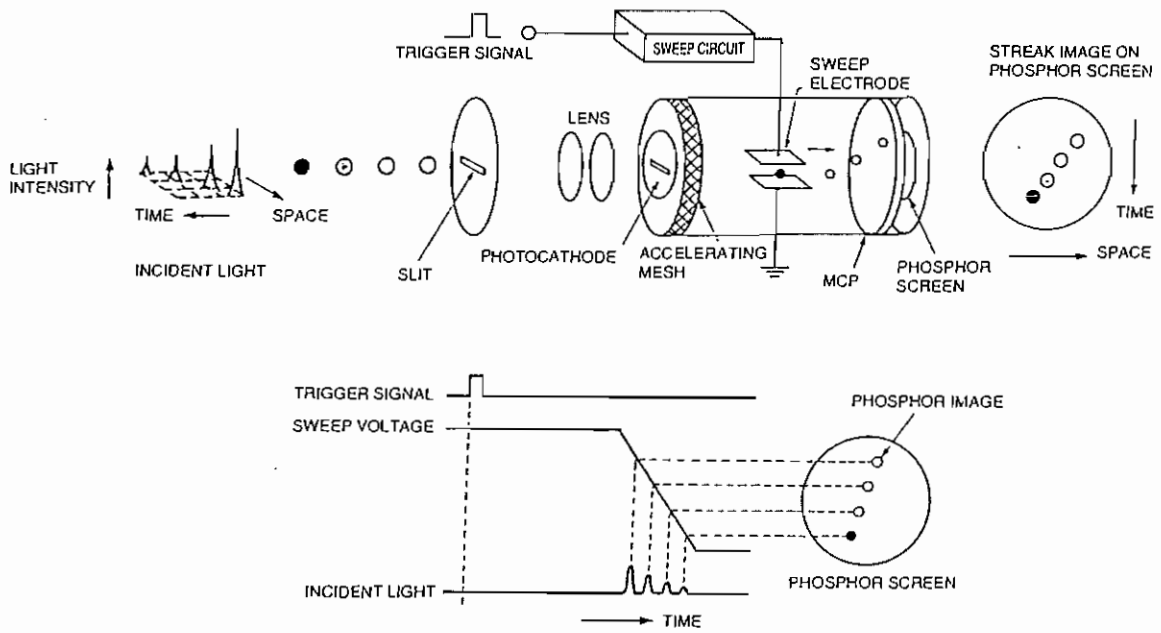

Fig. A.1. Schematic of the operating principle of the streak camera.

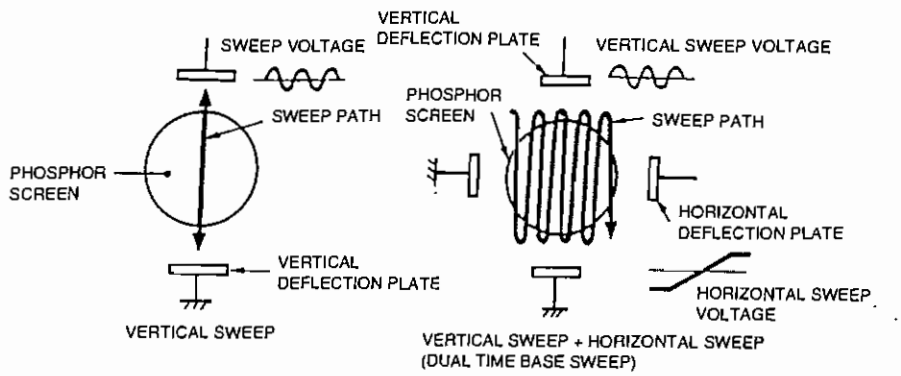

Fig. A.2. Sweep path using the dual time base.

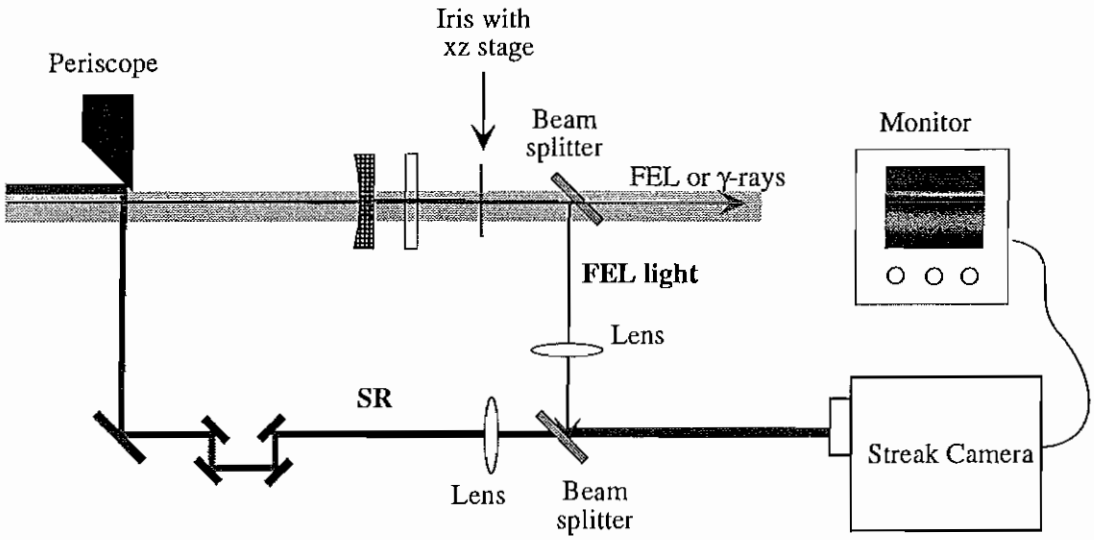

Fig. A.3. Schematic for the experimental setup of the simultaneous measurements of the electron and optical beam.

Appendix B:

The response function of the HPGe detector

The total High-Purity Germanium (HPGe) full energy peak response function of Compton backscattered γ rays is determined by an intrinsic response function due to the interaction of a monoenergetic γ rays with the HPGe crystal. A kinematic response function is caused by the incoming electron and optical beam parameters and the geometry of the scattering process. In this appendix, we discuss the intrinsic response function of the HPGe detector used in our measurements.

There are three components of the intrinsic response function: a primary Gaussian, a skewed Gaussian, and a smoothed step function in the low energy tail. The primary Gaussian arises from the statistical nature of the charge collection process, while the skewed Gaussian is due to incomplete charge collection of the detector. The smoothed step in the low energy tail is caused by the escape of photo-electrons from the detector and a Compton scattering background in the detector.

The three components can be expressed as (refer to [Schmid 1995] and the references therein):

$$R_G(E) = \frac{A}{\sqrt{2\pi}\sigma_{\gamma,D}} \exp\left[-\frac{(E-E_c)^2}{2\sigma_{\gamma,D}^2}\right],$$

$$R_{skew}(E) = B\exp\left[-\frac{E-E_c}{\beta}\right] erfc\left[\frac{E-E_c}{\sqrt{2}\sigma_{\gamma,D}} + \frac{\sigma_{\gamma,D}}{\sqrt{2}\beta}\right],$$

$$R_{step}(E) = C \cdot erfc\left[\frac{E-E_c}{\sqrt{2}\sigma_{\gamma,D}}\right],$$

where A, B, and C are normalization factors, E_c is the centroid of the peak, and $\sigma_{\gamma,D}$ is the RMS energy resolution of the HPGe detector. The total intrinsic response function of the HPGe detector is a linear combination of these three components:

$$R(E) = a \cdot R_G(E) + b \cdot R_{skew}(E) + c \cdot R_{step}(E),$$

where a, b, and c are coefficients satisfying $a+b+c=1$. The results for the parameters from fitting to D($\vec{p}$,γ)^{3}He γ-ray spectra [Schmid 1995] are a = 0.03, b = 0.75, c = 0.22, β = 1.72 keV, and $\sigma_{\gamma,D}$ = 1.78 keV (0.076 % FWHM energy resolution) for 5.5 MeV γ rays.

The energy resolution of Compton backscattered γ rays in the Duke/OK-4 is determined mainly by the induced energy spread of the electron beam. As summarized in Appendix C, our measured σ_γ/E_γ (RMS) is between 3.77×10^{-3} (i.e., 0.377%) and 6.03×10^{-3} (i.e., 0.603%) and the intrinsic resolution of the HPGe detector is expected to be approximately 4.4 keV at 10.3 MeV (about 0.1% FWHM energy resolution (i.e., 0.042% RMS energy resolution)) [Cecil 1985]. For a detector with 0.1% FWHM energy resolution, the energy spread is reduced only 0.25% for σ_γ/E_γ = 0.377% and 0.65% for σ_γ/E_γ = 0.603%. Hence, the contribution of the intrinsic resolution is negligible for measured energy spread.

When the target electron bunch is prevented from lasing by reducing the peak current below the lasing threshold, the energy spread of the electron beam is reduced by a factor of 2.5 up to 10 depending on the magnitude of the average current. Since the contribution of the electron energy spread to the γ-ray energy resolution is a factor of 2 (see Section 5.2.4), the total reduction in the γ-ray energy spread will be a factor between 5 and 20. In this case, we cannot neglect the intrinsic resolution of the HPGe detector and will need to include the intrinsic response function in Equation 5.2.28 or 5.2.41.

Appendix C:

Data for the measured and calculated parameters in Section 5.3.3

Data for fitting curves in Section 5.3.3																
E_e	[MeV]	460														
E_{FEL}	[eV]	3.22														
I_{OK}	[kA]	1.7704														
f_{rev}	[MHz]	2.789852														
h		64														
α_c		8.60E-03														
$\sigma_{\delta\,nat}$		2.72E-04														
Usr,e	[keV]	1.888527														
Dia. of collimator		[mm]	3													
Transmittance of input optics for power measurements						0.729										
Efficiency (HPGe)						0.0652										
Transmittance of SW cavity mirror					[%]	0.29										
Transmittance of SE cavity mirror					[%]	0.51										
Optical cavity loss					[%]	0.4										
														Theoretical calculation		
																Detector
Run #	Buncher	Slippage	RF	Current	Flux	E,max	σ_γ/E_γ	P_{FEL}/SW	ε x (rms)	ε y (rms)	σ_l	$\sigma_{\delta,ind}$	σ_γ/E_γ	P_{FEL}	P_{FEL}/SW	P_{FEL}/SW
	[A]	[μm]	[kV]	[mA]/2b	[Hz]	[MeV]	[%]	[mW]	[m nrad]	[m nrad]	[psec]		[%]	[mW]	[mW]	[mW]
180	312.7	15.737	500	5.375	656.3	10.3	0.603	6.22	16.1681	2.98864	132.5	2.635E-03	0.600	33.228	12.045	6.366
181	489.9	19.239	500	5.11	530.4	10.28	0.543	5.35	15.5596	2.82152	122.6	2.438E-03	0.560	29.177	10.577	5.590
182	613.9	22.611	500	4.765	429.8	10.27	0.475	4.38	16.1714	2.95108	105.5	2.098E-03	0.488	23.309	8.450	4.466
183	798.5	29.030	500	4.42	312.5	10.26	0.43	3.25	13.7443	3.31742	92.5	1.840E-03	0.430	18.860	6.837	3.613
184	988.3	37.383	500	3.938	179.5	10.27	0.378	2.02	12.1815	3.91789	79.5	1.581E-03	0.377	14.328	5.194	2.745
185	482.5	19.063	500	3.52	253.8	10.3	0.485	3.085	13.6253	2.52069	108.9	2.166E-03	0.495	17.792	6.450	3.409
186	482.5	19.063	389	3.02	173.7	10.3	0.455	2.33	13.8638	2.42758	107	1.877E-03	0.448	13.156	4.769	2.521

Appendix D

Diffusion coefficient $\tilde{D}_{FEL}(I)$ of Equation 2.5.26.

From the definition in Equation 2.5.22,

$$\tilde{D}_{FEL}(I)=\frac{1}{\pi}\int_0^{2\pi} D_{FEL}(I,\varphi_s)\cos^2\varphi_s\, d\varphi_s\,, \tag{D.1}$$

$$D_{FEL}(I,\varphi_s)=D_{FEL}(\varepsilon,s)=\frac{1}{2}f_0\left\langle \Delta\varepsilon_{FEL}{}^2\right\rangle_{\varphi_0}. \tag{D.2}$$

One can calculate $\left\langle \Delta\varepsilon_{FEL}{}^2\right\rangle_{\varphi_0}$ for a plane wave in a small signal regime (for details, refer to [Brau 1990], [Litvinenko 1989], and the references therein). From the Lorentz force equation, the energy transfer in a planar wiggler is given by

$$\frac{dE}{dt}=-e\vec{\mathcal{E}}\cdot\vec{v}=-e\mathcal{E}_x v_x. \tag{D.3}$$

For a plane wave, one can write the optical field as

$$\mathcal{E}_x=\mathcal{E}_0\cos(kz-wt+\varphi)\,, \tag{D.4}$$

where φ is an arbitrary initial phase at entry into the wiggler. Using Equation 2.3.8, equation D.3 can be re-written as

$$\frac{dE}{dz}=-e\mathcal{E}_x\frac{v_x}{v_z}\approx e\mathcal{E}_0\frac{K_w}{\gamma}\sin(k_w z)\cos(kz-wt+\varphi)\,. \tag{D.5}$$

Near the resonance condition and by averaging the fast oscillation term over the wiggler period, one arrives at

$$\frac{dE}{dz} = -\frac{1}{2} e\mathcal{E}_0 L_w [JJ] \frac{K_w}{\gamma} \sin\left(\frac{\Delta k}{2\gamma_{\parallel}^2} z - \varphi \right), \tag{D.6}$$

where

$$\Delta k = k - 2\gamma_{\parallel}^2 (2n+1) k_w, \qquad (n = 0, 1, 2 \cdot \cdot \cdot \cdot \cdot \cdot)$$

$$[JJ] = J_n(\xi_n) - J_{n+1}(\xi_n),$$

$$\xi_n = \frac{(2n+1)}{2} \frac{K_w^2/2}{1+K_w^2/2}.$$

Here, (2n+1) is the number of the harmonic. Integrating along the one wiggler at n = 0 (the fundamental harmonic) case, we obtain

$$\Delta E = \Delta E_0 \cos\varphi_0, \tag{D.7}$$

$$\Delta E_0 = \frac{1}{2} e\mathcal{E}_0 L_w [JJ] \frac{K_w}{\gamma} \frac{\sin\psi}{\psi}, \qquad \psi = \frac{\Delta k}{2\gamma_{\parallel}^2} \frac{L_w}{2}. \tag{D.8}$$

For an optical klystron,

$$\Delta E = \Delta E_1 \cos\varphi_1 + \Delta E_2 \cos\varphi_2, \tag{D.9}$$

$$\varphi_2 = \varphi_1 + k(\Delta s_0 + \frac{ds}{dE}(\varepsilon + \Delta E_1)), \ \varepsilon = E - E_0, \tag{D.10}$$

where Δs_0 is the slippage of the synchronous electrons between the centers of two different wigglers. In the OK-4, the two wigglers are identical so $\Delta E_1 = \Delta E_2 = \Delta E_0$. In the small signal regime, the second term can be expanded with respect to ΔE_1 (or ΔE_0). By averaging ΔE and ΔE^2 over random initial φ_1's (or φ_0's), one obtains

$$\left\langle \Delta\varepsilon_{FEL} \right\rangle_{\varphi_0} = -\frac{1}{2} (\Delta E_0)^2 k \frac{ds}{dE} \sin\left[k(\Delta s_0 + \frac{ds}{dE}\varepsilon) \right], \tag{D.11}$$

$$\left\langle \Delta\varepsilon_{FEL}{}^2 \right\rangle_{\varphi_0} = (\Delta E_0)^2 \left[1+\cos(k(\Delta s_0 + \frac{ds}{dE}\varepsilon)) \right]. \qquad \text{(D.12)}$$

For a pulsed optical field in the longitudinal direction, we replace the envelope $\mathcal{E}_0$ by

$$\mathcal{E}_0 \rightarrow \mathcal{E}_0(s) = \mathscr{E}_0 \exp\left[-\frac{(s-s_0)^2}{2\sigma_l^2} \right],$$

because the optical bunch length σ_l is much larger than total slippage of the electrons. $\mathscr{E}_0$ is the peak value of the optical field, s is the distance from the electron beam center, and s_0 is the center of the optical pulse which is measured from the center of the electron beam. When the electron and optical bunches are synchronized ($s_0 = 0$), one obtains

$$\begin{aligned} D_{FEL}(I,\varphi_s) &= D_{FEL}(\varepsilon, s) \\ &= a\left(1+\cos k\Delta s_0 \left(1-\frac{2\varepsilon}{E_0} \right) \right) \exp\left[-\frac{s^2}{\sigma_l^2} \right] \\ &= a\left(1+\cos k\Delta s_0 \left(1-\frac{2\sqrt{2I}}{E_0}\cos\varphi_s \right) \right) \exp\left[-\frac{2Ib^2\sin^2\varphi_s}{\sigma_l^2} \right], \end{aligned} \qquad \text{(D.13)}$$

where

$$a = \frac{1}{2} f_0 \left(\frac{1}{2} e\,\mathscr{E}_0 L_w [JJ] \frac{K_w}{\gamma} \frac{\sin\psi}{\psi} \right)^2 \cong \frac{1}{2} f_0 \left(\frac{1}{2} e\,\mathscr{E}_0 L_w [JJ] \frac{K_w}{\gamma} \right)^2.$$

At the maximum gain condition ($\sin k\Delta s_0 = -1$), Equation D.13 can be reduced to

$$D_{FEL}(I,\varphi_s) = a(1-\sin(\mu\cos\varphi_s))\exp\left[-\nu\sin^2\varphi_s \right], \qquad \text{(D.14)}$$

where

$$\mu = k\Delta s_0 \frac{2\sqrt{2I}}{E_0} \text{ and } \nu = \frac{2Ib^2}{\sigma_l^2}.$$

Substituting Equation D.14 into Equation D.1, one calculates the diffusion coefficient averaged over one period of the synchrotron oscillation.

$$\tilde{D}_{FEL}(I) = \frac{a}{\pi}\int_{-\pi}^{\pi} \exp\left[-\nu \sin^2\varphi_s\right]\cos^2\varphi_s \, d\varphi_s$$

$$-\frac{a}{\pi}\int_{-\pi}^{\pi} \exp\left[-\nu \sin^2\varphi_s\right]\sin(\mu\cos\varphi_s)\cos^2\varphi_s \, d\varphi_s \,. \qquad \text{(D.15)}$$

Then,

$$\frac{a}{\pi}\int_{-\pi}^{\pi} \exp\left[-\nu \sin^2\varphi_s\right]\sin(\mu\cos\varphi_s)\cos^2\varphi_s \, d\varphi_s$$

$$= \frac{2a}{\pi}\int_{0}^{\pi} \exp\left[-\nu \sin^2\varphi_s\right]\sin(\mu\cos\varphi_s)\cos^2\varphi_s \, d\varphi_s \,, \left(\theta = \varphi_s - \frac{\pi}{2}\right)$$

$$= \frac{2a}{\pi}\int_{-\frac{\pi}{2}}^{\frac{\pi}{2}} \exp\left[-\nu \cos^2\theta\right]\sin(\mu\sin\theta)\sin^2\theta \, d\theta = 0$$

and

$$\frac{a}{\pi}\int_{-\pi}^{\pi} \exp\left[-\nu \sin^2\varphi_s\right]\cos^2\varphi_s \, d\varphi_s = \frac{2a}{\pi}\int_{-\frac{\pi}{2}}^{\frac{\pi}{2}} \exp\left[-\nu \cos^2\theta\right]\sin^2\theta \, d\theta \,, \left(\theta = \varphi_s - \frac{\pi}{2}\right)$$

$$= \frac{a}{\pi}e^{-\nu/2}\int_{0}^{\pi} \exp\left[-\frac{\nu}{2}\cos x\right](1-\cos x)dx \,, \quad (x = 2\theta)$$

$$= \frac{a}{\pi}e^{-\nu/2}\left(\int_{0}^{\pi} \exp\left[-\frac{\nu}{2}\cos x\right]dx + 2\frac{d}{d\nu}\int_{0}^{\pi} \exp\left[-\frac{\nu}{2}\cos x\right]dx\right)$$

by using the definition of modified Bessel function $I_\nu(z)$,

$$I_\nu(z) = \frac{(z/2)^\nu}{\Gamma(\nu+\frac{1}{2})\Gamma(\frac{1}{2})}\int_0^\pi e^{\pm z\cos\theta}\sin^{2\nu}\theta d\theta \,,$$

$$I_1(z) = \frac{d}{dz} I_0(z).$$

Therefore, we finally obtain Equation 2.5.23:

$$\tilde{D}_{FEL}(I) = ae^{-qI}\left(I_0(qI) + I_1(qI)\right), \qquad q = v/2I = b^2/\sigma_I^2.$$

Appendix E:

Energy spectrum $\frac{dN_\gamma(E_\gamma)}{dE_\gamma d\Omega}$ of Equations 5.2.40 and 5.2.44.

From Equation 5.2.39, the energy spectrum for the "*head-on collision*" case is

$$\frac{dN_\gamma(E_\gamma)}{dE_\gamma d\Omega} = N_e N_{ph} c \int\int\int\int dp^3 dk^3 dV dt$$

$$\cdot \frac{d\sigma(\vec{\mathbf{p}},\vec{\mathbf{k}};k',\theta_f)}{d\Omega}(1+\beta) f_e(\vec{\mathbf{r}},\vec{\mathbf{p}},t) f_{ph}(\vec{\mathbf{r}},\vec{\mathbf{k}},t)\delta(E_\gamma - \hbar\omega'), \quad \text{(E.1)}$$

where (from Equations 5.2.32 and 5.2.33)

$$f_e(\vec{\mathbf{r}},\vec{\mathbf{p}},t) = \frac{1}{(2\pi)^3 \varepsilon_x \varepsilon_y \sigma_p \sigma_l} \exp\left[-\frac{(\gamma_x x^2 + 2\alpha_x xx' + \beta_x x'^2)}{2\varepsilon_x} - \frac{(\gamma_y y^2 + 2\alpha_y yy' + \beta_y y'^2)}{2\varepsilon_y} \right.$$

$$\left. - \frac{(p_z - p_0)^2}{2\sigma_p^2} - \frac{(z-ct)^2}{2\sigma_l^2} \right] \quad \text{(E.2)}$$

$$\gamma_{x,y} = \frac{1+\alpha_{x,y}^{\ 2}}{\beta_{x,y}}, \quad \alpha_{x,y} = -\frac{1}{2}\beta'_{x,y} \qquad (\alpha_{x,y}, \beta_{x,y}, \text{ and } \gamma_{x,y} : \text{Twiss parameters})$$

$$\sigma_{x,y} = \sqrt{\varepsilon_{x,y}\beta_{x,y}}, \quad \sigma_{x',y'} = \sqrt{\varepsilon_{x,y}\gamma_{x,y}}$$

$$f_{ph}(\vec{\mathbf{r}},\vec{\mathbf{k}},t) = \frac{k^2}{(2\pi)^3 \sigma_k \sigma_z} \exp\left[-\frac{k}{\beta_0}\left(x^2 + (\beta_0 \vartheta_x)^2 + y^2 + (\beta_0 \vartheta_y)^2\right) \right.$$

$$\left. - \frac{(k-k_0)^2}{2\sigma_k^2} - \frac{(z+ct)^2}{2\sigma_z^2} \right] \quad \text{(E.2)}$$

$$\vec{\mathbf{k}} = k(\vartheta_x \hat{x} + \vartheta_y \hat{y} + \hat{z}),$$

and (from Equation 5.2.19)

$$\frac{d\sigma(\vec{\mathbf{p}},\vec{\mathbf{k}};k',\theta_f)}{d\Omega} = \frac{8r_e^2}{x^2}\left\{(1-\xi_3)\left[\left(\frac{1}{x}-\frac{1}{y}\right)^2+\left(\frac{1}{x}-\frac{1}{y}\right)\right]+\frac{1}{4}\left(\frac{x}{y}+\frac{y}{x}\right)\right\}\left(\frac{\hbar\omega'(\theta_f)}{mc^2}\right)^2$$

$$x = \frac{2\gamma\hbar\omega(1+\beta)}{mc^2}, \quad y = \frac{2\gamma\hbar\omega'(1-\beta\cos\theta_f)}{mc^2}. \qquad \text{(E.3)}$$

Since the scattering cross section is independent of the spatial coordinates and the time t, the incoming photon angles ϑ_x and ϑ_y, one can integrate the incoming electron and photon distribution functions over $dVdtd\vartheta_x d\vartheta_y$. Substituting Equations E.2 and E.3 into E.1 and using Equation 5.2.37,

$$\frac{dN_\gamma(E_\gamma)}{dE_\gamma d\Omega} = N_e N_{ph} c \frac{k^2}{(2\pi)^6 \varepsilon_x \varepsilon_y \sigma_p \sigma_l \sigma_k \sigma_z} \iiiint dp d\theta_x d\theta_y dk \frac{d\sigma(p,\theta_x,\theta_y,k;k')}{d\Omega}$$

$$\times (1+\beta)\delta(E_\gamma - \hbar\omega')\exp\left[-\frac{(p_z-p_0)^2}{2\sigma_p^2}-\frac{(k-k_0)^2}{2\sigma_k^2}\right]\iiiint dxdydzdtd\vartheta_x d\vartheta_y$$

$$\times \exp\left[-\frac{(\gamma_x x^2 + 2\alpha_x x(\theta_x-(x-c_x)/L)+\beta_x(\theta_x-(x-c_x)/L)^2)}{2\varepsilon_x}-\frac{k}{\beta_0}x^2\right]$$

$$\times \exp\left[-\frac{(\gamma_y y^2 + 2\alpha_y y(\theta_y-(y-c_y)/L)+\beta_y(\theta_y-(y-c_y)/L)^2)}{2\varepsilon_y}-\frac{k}{\beta_0}y^2\right]$$

$$\times \exp\left[-\frac{(z+ct)^2}{2\sigma_z^2}-\frac{(z-ct)^2}{2\sigma_l^2}\right]\exp\left[-\frac{k}{\beta_0}(\beta_0\vartheta_x)^2-\frac{k}{\beta_0}(\beta_0\vartheta_y)^2\right]. \qquad \text{(E.4)}$$

One can calculate the above equation using the relation for the integration of a Gaussian function,

$$\int_{-\infty}^{\infty} dx \exp\left[-a(x-b)^2\right] = \sqrt{\frac{\pi}{a}}.$$

Integrating Equation E.4 over ϑ_x and ϑ_y gives $\pi/k\beta_0$ and integrating over z and t gives $\pi\sigma_l\sigma_z/c$. Integrating Equation E.4 over x and substituting γ_x in Equation E.2, one can obtain

$$\int_{-\infty}^{\infty} dx \exp\left[-\frac{(\gamma_x x^2 + 2\alpha_x x(\theta_x - (x-c_x)/L) + \beta_x(\theta_x - (x-c_x)/L)^2)}{2\varepsilon_x} - \frac{k}{\beta_0}x^2\right]$$

$$= \int_{-\infty}^{\infty} dx \exp\left[-\frac{1}{2\varepsilon_x}\left((\gamma_x - \frac{2\alpha_x}{L} + \frac{\beta_x}{L^2} + \frac{2k\varepsilon_x}{\beta_0})x^2 + 2\left(\alpha_x - \frac{\beta_x}{L}\right)\left(\theta_x - \frac{c}{L}\right)x + \beta_x\left(\theta_x - \frac{c}{L}\right)^2\right)\right]$$

$$= \sqrt{2\pi\varepsilon_x\beta_x}\left[1 + \left(\alpha_x - \frac{\beta_x}{L}\right)^2 + \frac{2k\varepsilon_x\beta_x}{\beta_0}\right]^{-1/2}$$

$$\times \exp\left[-\frac{\beta_x}{2\varepsilon_x}\left\{\left[1 + \frac{2k\varepsilon_x\beta_x}{\beta_0}\right]\left[1 + \left(\alpha_x - \frac{\beta_x}{L}\right)^2 + \frac{2k\varepsilon_x\beta_x}{\beta_0}\right]^{-1}\right\}\left(\theta_x - \frac{c}{L}\right)^2\right]. \quad \text{(E.5)}$$

Similarly, integrating Equation E.4 over y, one can obtain the same form of Equation E.5 by changing the subscript x to y. Let's define the variables ξ_x, ξ_y, ζ_x, ζ_y, σ_{θ_x}, and σ_{θ_y} as:

$$\xi_{x,y} = 1 + \left(\alpha_{x,y} - \frac{\beta_{x,y}}{L}\right)^2 + \frac{4\pi\varepsilon_{x,y}\beta_{x,y}}{\lambda\beta_0},$$

$$\zeta_{x,y} = 1 + \frac{4\pi\varepsilon_{x,y}\beta_{x,y}}{\lambda\beta_0}, \quad \text{(E.6)}$$

$$\sigma_{\theta_{x,y}}^2 = \frac{\varepsilon_{x,y}\xi_{x,y}}{\beta_{x,y}\zeta_{x,y}}.$$

Therefore, one arrives at (i.e., Equation 5.2.40)

$$\frac{dN_\gamma(E_\gamma)}{dE_\gamma d\Omega}=\frac{N_e N_{ph}\cdot k/\beta_0}{(2\pi)^3\sigma_k\sigma_p}\sqrt{\frac{\beta_x\beta_y}{\varepsilon_x\varepsilon_y\xi_x\xi_y}}\iiiint dpd\theta_x d\theta_y dk\frac{d\sigma(p,\theta_x,\theta_y,k;k')}{d\Omega}(1+\beta)$$

$$\times\exp\left[-\frac{(\theta_x+c_x/L)^2}{2\sigma_{\theta_x}^2}-\frac{(\theta_y+c_y/L)^2}{2\sigma_{\theta_y}^2}-\frac{(p_z-p_0)^2}{2\sigma_p^2}-\frac{(k-k_0)^2}{2\sigma_k^2}\right]\delta(E_\gamma-\hbar\omega'),\quad\text{(E.7)}$$

For a flat electron beam, θ_y and k are negligible. Integrating over θ_y and k and changing the variable momentum p ($p=\gamma\beta mc\approx\gamma mc$) to the energy parameter γ, we obtain

$$\frac{dN_\gamma(E_\gamma)}{dE_\gamma d\Omega}=N_e N_{ph}\frac{k/\beta_0}{4\pi^2\sigma_\gamma}\sqrt{\frac{\beta_x}{\varepsilon_x\xi_x\zeta_y}}\iint d\gamma d\theta_x\frac{d\sigma(\gamma,\theta_x;k',k_0,\theta_y=0)}{d\Omega}(1+\beta)$$

$$\times\exp\left[-\frac{(\theta_x+c_x/L)^2}{2\sigma_{\theta_x}^2}-\frac{(\gamma-\gamma_0)^2}{2\sigma_\gamma^2}\right]\delta(E_\gamma-\hbar\omega').\quad\text{(E.8)}$$

By using the Dirac delta function relation, one can rewrite $\delta(E_\gamma-\hbar\omega')$ as:

$$\delta(E_\gamma-\hbar\omega')\approx\delta\left(E_\gamma-\frac{4\gamma^2\hbar\omega}{1+\gamma^2\theta_x^2+4\gamma\hbar\omega/mc^2}\right)$$

$$=\delta(\gamma-\gamma_r)\left|\frac{d}{d\gamma}\left(E_\gamma-\frac{4\gamma^2\hbar\omega}{1+\gamma^2\theta_x^2+4\gamma\hbar\omega/mc^2}\right)\right|^{-1}_{\gamma=\gamma_r}$$

$$=\delta(\gamma-\gamma_r)\frac{(1+\gamma_r^2\theta_x^2+4\gamma_r a)^2}{8\gamma_r\hbar\omega(1+2\gamma_r a)},$$

where

$$\gamma_r=\frac{2E_\gamma a}{(4\hbar\omega-E_\gamma\theta_x^2)}\left\{1+\sqrt{1+\frac{(4\hbar\omega-E_\gamma\theta_x^2)}{4E_\gamma a^2}}\right\}\text{ with }a=\frac{\hbar\omega}{mc^2},$$

satisfying

$$E_\gamma - \frac{4\gamma_r^2\hbar\omega}{1+\gamma_r^2\theta_x^2+4\gamma_r^2\hbar\omega/mc^2} = 0 .$$

In order to have a real positive value of γ_r, it is necessary that

$$0 < \theta_x < \theta_{\max} \text{ for } \theta_{\max} = \sqrt{4\hbar\omega/E_\gamma} .$$

Also, the differential scattering cross section is expressed as:

$$\frac{d\sigma(E_\gamma,\theta_x;k_0,\theta_y=0,\gamma=\gamma_r)}{d\Omega}$$

$$= 8r_e^2\left\{\frac{1}{4}\left(\frac{4\gamma_r^2\hbar\omega}{E_\gamma(1+\gamma_r^2\theta_x^2)}+\frac{E_\gamma(1+\gamma_r^2\theta_x^2)}{4\gamma_r^2\hbar\omega}\right)-(1-\xi_3)\frac{\gamma_r^2\theta_x^2}{(1+\gamma_r^2\theta_x^2)}\right\}\left(\frac{E_\gamma}{4\gamma_r\hbar\omega}\right)^2 . \quad \text{(E.9)}$$

For a finite size collimator at an arbitrary position, the flux is obtained by integrating over the collimator opening center c_x of collimator, i.e., ($c_x - \Delta x/2$, $c_x + \Delta x/2$):

$$\frac{\Delta N_\gamma(E_\gamma)}{dE_\gamma d\Omega} \approx N_e N_{ph}\frac{k/\beta_0}{2\pi^2\sigma_\gamma}\sqrt{\frac{\beta_x}{\varepsilon_x\xi_x\zeta_y}}\int_{c_x-\Delta x/2}^{c_x+\Delta x/2}dc_x\int_0^{\theta_{\max}}d\theta_x\frac{d\sigma(E_\gamma,\theta_x;k_0,\theta_y=0,\gamma=\gamma_r)}{d\Omega}$$

$$\times\frac{(1+\gamma_r^2\theta_x^2+4\gamma_r a)}{8\gamma_r\hbar\omega(1+2\gamma_r a)}\exp\left[-\frac{(\theta_x+c_x/L)^2}{2\sigma_{\theta_x}^2}-\frac{(\gamma_r-\gamma_0)^2}{2\sigma_\gamma^2}\right] . \quad \text{(E.10)}$$

Bibliography

F.R. Arutyunian and V.A. Tumanian, 1963, "The Compton effect on relativistic electrons and the possibility of obtaining high energy beams", Physics Letters 4, p. 176.

M. Billardon *et. al.*, 1985, "Free Electron Laser Experiment at Orsay: A Review", IEEE J. Quantum Electronics QE-21, p. 805.

B.H. Burnham, 1995, "Storage Ring Free Electron Lasers: Dynamics and Characteristics", Ph.D. Thesis, Duke University.

F.E. Cecil *et. al.*, 1985, "Experimental Determination of Absolute Efficiency and Energy Resolution for NaI(Tl) and Germanium Gamma Ray Detectors at Energies from 2.6 to 16.1 MeV", Nucl. Instr. Meth. Phys. Res. A 234, p. 479.

T.S. Carman *et. al.*, 1996, "The TUNL-FEL inverse Compton γ-ray source a nuclear physics facility", Nucl. Instr. Meth. Phys. Res. A 378, p. 1.

W.B. Colson and A. Renier, 1983, "Pulse Propagation in Free Electron Lasers", Journal De Physique Colloque C1, C1-11.

W.B. Colson and P. Elleaume, 1982, "Electron Dynamics in Free Electron Laser Resonator Modes", Applied Physics B 29, p. 101.

W.B. Colson, 1981, "The Nonlinear Wave Equation for Higher Harmonics in Free Electron Lasers", IEEE J. Quantum Electronics QE-17, p. 1417.

M.E. Couprie *et. al.*, 1995, "Optical cavities for UV free electron lasers", Nucl. Instr. Meth. Phys. Res. A 358, p. 382.

G. Dattoli *et. al.*, 1980, "A Multimode Small Signal Analysis of the Single Pass Free Electron Laser", Optics Communications vol. 35, no. 3, p. 407.

G. Dattoli *et. al.*, 1981a, "Progress in the Hamiltonian Picture of the Free Electron Laser", IEEE J. Quantum Electronics QE-17, p. 1371.

G. Dattoli and A. Renier, 1981b, "The Free Electron Laser Single–Particle: Multimode Classical Theory", IL Nuovo Cimento vol 61 B, N. 2, p. 153.

D.A.G. Deacon and J.M.J. Madey, 1980, "Isochronous Storage Ring Laser: A Possible Solution to the Electron Heating Problem in Recirculating Free-Electron Lasers", Physics Review Letters 44, no. 7, p. 449.

D.A.G. Deacon *et. al.*, 1984, "Optical Klystron Experiments for the ACO Storage Ring Free Electron Laser", Applied Physics B 34, p. 207.

P. Elleaume, 1983, "Optical Klystron", Journal De Physique Colloque C1, C1-333.

P. Elleaume, 1985, "Microtemporal and Spectral Structure of Storage Ring Free Electron Lasers", IEEE J. Quantum Electronics QE-21, p. 1012.

P. Elleaume, 1985, "Storage Ring FEL Theory", Nucl. Instr. Meth. Phys. Res. A 237, p. 28.

P. Elleaume *et. al.*, 1985, "Diagnostic Techniques and VUV Induced Degradation of the Mirrors Used in the ORSAY Storage Ring Free Electron Laser", Nucl. Instr. Meth. Phys. Res. A 237, p. 263.

D. Garzella *et. al.*, 1985, "Mirror degradation and heating in storage ring FELs", Nucl. Instr. Meth. Phys. Res. A 237, p. 387.

F.A. Hopf *et. al.*, 1976, "Classical theory of a free electron laser", Optics Communications v. 18, no. 4, p. 413.

F.A. Hopf *et. al.*, 1980, "The Free Electron Laser: From A Laser-Physics Perspective", in Physics of Quantum Electronics v. 7, Addison-Wesley, p. 31.

M. Hosaka *et. al.*, 1997, "Observation of intracavity Compton Backscattering of the UVSOR free electron laser", Nucl. Instr. Meth. Phys. Res. A 393, p. 525.

Z. Huang and R.D. Ruth, 1998, "Laser-Electron Storage Ring", Physics Review Letters 80, no. 5, p. 976.

V.N. Litvinenko, 1989, "Optical Klystron at VEPP-3 Storage Ring: Lasing in the Visible and the UV", Ph.D. Thesis, Budker Institute of Nuclear Physics (BINP), Novosibrisk, Russia.

V.N. Litvinenko and N.A Vinokurov, 1991, "Lasing spectrum and temporal structure in storage ring FELs: theory and experiment", Nucl. Instr. Meth. Phys. Res. A 304, p. 66.

V.N. Litvinenko *et. al.*, 1991, "The Results of Lasing Linewidth Narrowing on VEPP-3 Storage Ring Optical Klystron", IEEE J. Quantum Electronics QE-27, p. 2560.

V.N. Litvinenko *et. al.*, 1993, "On the Classical analog of the Einstein relations between spontaneous emission, induced emission and absorption", Nucl. Instr. Meth. Phys. Res. A 331, p. 440.

V.N. Litvinenko and J.M.J. Madey, 1995a, "High Power Inverse Compton γ-ray Source at Duke Storage ring", Proceedings 1995 SPIE v. 2521, p. 55.

V.N. Litvinenko *et. al.*, 1995b, "mm-wave isochronous FEL and hard X-ray inverse Compton source at the Duke storage ring", Nucl. Instr. Meth. Phys. Res. A 358, p. 345.

V.N. Litvinenko *et. al.*, 1995c, "Giant laser pulses in the Duke storage ring UV FEL", Nucl. Instr. Meth. Phys. Res. A 358, p. 334.

V.N. Litvinenko *et. al.*, 1995d, "Dynamics of the Duke Storage ring UV FEL", Nucl. Instr. Meth. Phys. Res. A 358, p. 369.

V.N. Litvinenko *et. al.*, 1995e, "3D free electron laser gain for an electron beam with finite emittance and energy spread", Nucl. Instr. Meth. Phys. Res. A 359, p. 50.

V.N. Litvinenko *et. al.*, 1995f, "High Peak Pulse Power Operation of the OK-4/Duke XUV FEL", SPIE vol. 2521, p. 78.

V.N. Litvinenko *et. al.*, 1996, "Commissioning of the Duke storage ring", Proceedings of the 1995 Particle Accelerator Conference, vol. 1, p. 213.

V.N. Litvinenko *et. al.*, 1997, "Gamma-Ray Production in a Storage Ring Free-Electron Laser", Physics Review Letters 78, No. 24, p. 4569.

V.N. Litvinenko *et. al.*, 1998, "First UV/visible lasing with the OK-4/Duke storage ring FEL", Nucl. Instr. Meth. Phys. Res. A 407, p. 8.

V.N. Litvinenko *et. al.*, 1999a, "OK-4/Duke storage ring FEL lasing in the deep-UV", Nucl. Instr. Meth. Phys. Res. A 429, p. 151.

V.N. Litvinenko *et. al.*, 1999b, "Performance of the OK-4/Duke Storage Ring FEL", to be published in Nucl. Instr. Meth. Phys. Res. A, presented in FEL'99 Conference, August 23 – 27, 1999.

R.H. Milburn, 1963, "Electron scattering by an intense polarized photon field", Physics Review Letters 10, p. 75.

D. Nutarelli *et. al.*, 1998, "Gamma rays production by intra-cavity Compton Back Scattering with Super-ACO Storage Ring Free Electron Laser", Nucl. Instr. Meth. Phys. Res. A 407, p. 459.

H. Ohgaki *et. al.*, 1997, "FEL-X Project: High Brightness X-rays from FEL-Compton Backscattering", Proceedings of 18th FEL Conference, Rome, Italy, II-14.

S.H. Park *et. al.*, 1999, "Performance of the OK-4/Duke Storage Ring FEL and γ-ray source", Asian FEL'99 Conference, June 8 – 10, 1999, to be published.

S.H. Park *et. al.*, 1998, "OK-4/Duke monochromatic γ-ray source : Performance and prediction", Nucl. Instr. Meth. Phys. Res. A 407, p. 224.

S.H. Park *et. al.*, 1996, "VUV optical ring resonator for the Duke storage ring free electron laser", Nucl. Instr. Meth. Phys. Res. A 375, p. 487.

I.V. Pinayev, M. Emamian, V.N. Litvinenko, S.H. Park, and Y. Wu, 1998, "System for control and stabilizing of OK-4/Duke FEL optical cavity", AIP-Conference Proceedings no. 451, p. 545.

A. Renier, 1979, "Storage ring Operation of the Free Electron Laser: Amplifier", IL Nuovo Cimento vol 53 B, N. 1, p. 160.

R. Roux *et. al.*, 1997, "The Super-ACO FEL Dynamics measured with a streak camera", Nucl. Instr. Meth. Phys. Res. A 393, p. 33.

A.M. Sandorfi *et. al.*, 1983, "High Energy Gamma Ray Beams From Compton Backscattered Laser Light", IEEE Trans. Nuclear Science, Vol. NS-30, no.4, p. 3083.

M. Sands, 1970, "The Physics of Electron Storage Ring - An Introduction", SLAC Report, p. 121.

G.J. Schmid, 1995, "Radiative Capture of Polarized Protons by Deuterium in the Energy Range E_p(lab) = 80 – 0 keV", Ph.D. Thesis, Duke University.

N.A. Vinokurov and A.N. Skrinsky, 1977, "Power Limit for an Optical Klystron Installed on a Storage Ring", Novosibirsk preprint INP77-59.

Y. Wu, 1995, "Theoretical and Experimental Studies of the Beam Physics in the Duke FEL Storage Ring", Ph.D. Thesis, Duke University.

Reference Books

M. Born and E. Wolf, *Principles of Optics*, 6th edition, Pergamon Press, 1980.

C.A. Brau, *Free Electron Lasers*, New York Academic Press, 1990.

W.B. Colson, C. Pellegrini, and A. Renieri, *Laser Handbook: free electron lasers, vol. 6*, North-Holland, 1990.

J.D. Jackson, *Classical Electrodynamics*, 2nd Edition, John Wiley & Son, 1975.

G.F. Knoll, *Radiation Detection and Measurement*, John Wiley & Sons, New York, 1989.

L.D. Landau and E.M. Lifshitz, *Quantum Electrodynamics: Course of Theoretical Physics vol. 4*, Pergamon Press, 1982.

L.D. Landau and E.M. Lifshitz, *The Classical Theory of Fields: Course of Theoretical Physics vol. 2*, Pergamon, 1975.

J.J. Sakurai, *Advanced Quantum Mechanics*, Benjamin/Cummings Publishing Company, 1967.

A.E. Siegman, *Lasers*, University Science Books, 1986.

G.B. Thomas, *Calculus and Analytic Geometry*, 4th Edition, Addison-Wesley Pub. Co., 1969.

H. Wiedemann, *Particle Accelerator Physics: Basic Principles and Linear Beam Dynamics*, Springer-Verlag, 1993.

H. Wiedemann, *Particle Accelerator Physics II: Nonlinear and Higher-Order Beam Dynamics*, Springer-Verlag, 1995.

S. Wolfram, *Mathematica: A System for Doing Mathematics by Computer*, Addison-Wesley, 1991.